

Syracuse University

SURFACE

Dissertations - ALL

SURFACE

December 2016

STRUCTURE, DYNAMICS AND RHEOLOGY OF SURFACTANT MICELLES AND MICELLE-NANOPARTICLE SOLUTIONS: A MOLECULAR DYNAMICS STUDY

Abhinanden Sambasivam
Syracuse University

Follow this and additional works at: <https://surface.syr.edu/etd>



Part of the [Engineering Commons](#)

Recommended Citation

Sambasivam, Abhinanden, "STRUCTURE, DYNAMICS AND RHEOLOGY OF SURFACTANT MICELLES AND MICELLE-NANOPARTICLE SOLUTIONS: A MOLECULAR DYNAMICS STUDY" (2016). *Dissertations - ALL*. 593.

<https://surface.syr.edu/etd/593>

This Dissertation is brought to you for free and open access by the SURFACE at SURFACE. It has been accepted for inclusion in Dissertations - ALL by an authorized administrator of SURFACE. For more information, please contact surface@syr.edu.

Abstract

Surfactant micelles are widely used in a number of industrial, commercial and household products and processes. Understanding flow-microstructure coupling in micellar systems can benefit applications ranging from targeted drug delivery and detergency to enhanced oil recovery and hydrofracking. Amongst micellar fluids, wormlike micelles (WLMs) are extremely interesting due to their structural similarity to polymers and their ability to constantly undergo scission and recombination at equilibrium. More recently, much has been generated in studying the effect of adding colloidal particles to WLMs. Colloidal particles can not only add functionality to the fluid but also act as viscosity modifiers. Such solutions can be used to design active nanomaterials for applications in energy harvesting and sensing. While several theories and continuum-level computational models have been developed to study the dynamics and rheology of WLMs, molecular-level explorations of the flow-structure coupling in such solutions is lacking. Further, in the case of mixtures of colloidal particles and WLMs, there are only a handful of attempts to develop theoretical/computational frameworks capable of describing their thermodynamics, self-assembly and phase behavior. The goals of this thesis are to uncover mechanisms by which WLMs interact with colloidal particles and to determine how these interactions affect the macroscopic properties of mixtures of model WLMs and colloidal nanoparticles (NPs) using molecular dynamics (MD) simulations.

Coarse-grained (CG) molecular models and corresponding force-fields are employed to describe the NP, cationic cetyltrimethylammonium chloride (CTAC) surfactant, hydrotropic sodium salicylate (NaSal) salt, solvent and the underlying physico-chemical interactions. Results are first presented for the dynamics of a single self-assembled rodlike micellar aggregate under shear flow. The effect of shear rate on the configurational dynamics, e.g. orientation distribution

of the end-to-end vector and tumbling frequency are presented and compared to experimental observations as well as predictions from stochastic simulations and mesoscopic theories. Further, a relationship between micelle length and stretching force is presented and compared with experimental estimates of similar forces in biological systems. Finally, a shear rate-independent energy barrier for micelle scission is identified for relatively large shear rates.

We also show that the addition of NPs to surfactant solutions can result in the formation of NP-surfactant complexes (NPSCs). The effect of NP charge and surface chemistry on the nature of the self-assembly is discussed. Further, such NPSCs can further interact with WLMs, in the presence of NaSal salt, to form electrostatically stabilized micelle-NP junctions via an end cap attachment mechanism. The dynamics, energetics and stability of such junction formation is also described in detail. These junctions can give rise to unique rheological modifications of WLMs such as significant buildup in viscosity and viscoelasticity. Large-scale equilibrium and non-equilibrium MD simulations consisting of several NPs and WLMs are performed to study the flow-microstructure coupling in such systems. The relationship between the zero-shear viscosity, NP volume fraction and salt concentration at a fixed surfactant concentration is presented. Shear thinning behavior is observed for all of the systems studied. Shear thinning is accompanied by flow-alignment and shear-induced isotropic-to-nematic transitions in micellar systems. Further, the evolution of the first normal stress difference, N_1 , is presented as a function of time and shear rate, and compared with experimental observations for similar systems. The results of this work provides insight into the mechanisms of self-assembly in WLMs and colloidal NPs and demonstrate that rheological properties of WLMs can be uniquely controlled by the addition of NPs.

STRUCTURE, DYNAMICS AND RHEOLOGY OF SURFACTANT
MICELLES AND MICELLE-NANOPARTICLE SOLUTIONS: A
MOLECULAR DYNAMICS STUDY

By

Abhinanden Sambasivam

B. Tech. Anna University, 2010

DISSERTATION

Submitted in partial fulfillment of the requirements for the degree of

Doctor of Philosophy in Chemical Engineering

Syracuse University

December 2016

Copyright © 2016 Abhinanden Sambasivam

All rights reserved

Acknowledgements

First and foremost, I would like to thank my dissertation advisor, Radhakrishna Sureshkumar, who has afforded me a great deal of freedom to explore in my research and has always served as an outstanding academic mentor and role model. I would like to thank my committee members: Arindam Chakraborty, Jesse Bond, Shikha Nangia, Dacheng Ren and James Henderson for their constructive comments and invaluable inputs to my dissertation.

This dissertation would not have been nearly as successful without the help of a number of friends and colleagues who assisted (whether knowingly or unknowingly) with the work contained herein. Thanks to Ashish Sangwai, who indoctrinated me into the Sureshkumar group and introduced me to the world of molecular modeling and simulations, and Subas Dhakal who has always motivated me to do more than I believed I could. I would also like to thank Tao, Pete, Shirley, Yating, Bendy, Kelechi, Stephen, Mardochee and Meenakshi for their support and company which has definitely made my graduate studies as enjoyable as I could have hoped for. I would also like to thank all my friends at Syracuse and elsewhere for such unforgettable memories and lasting friendships. My life and career are much the better for it.

Most importantly, I would like to thank my parents, Padmini and Sambasivam, and my sister, Krithika, whose constant encouragement to explore and enjoy the world in all its aspects has made my life such a fulfilling and worthwhile journey. This dissertation, and my life, would not be complete without my wife, Divya Parameswaran, whose unconditional love and tremendous sacrifice has kept me motivated and optimistic in the toughest of times. I would also like to thank my extended family and in-laws for their constant support and understanding which has helped me a great deal in this journey.

I dedicate this humble effort to

My grandfather, V. Ramnath, who is my greatest inspiration and the only man I
have ever wanted to impress

&

My grandmother, Savithri Ramnath, for her unconditional love and support.

TABLE OF CONTENTS

LIST OF FIGURES	xi
LIST OF TABLES	xvii
CHAPTER 1 INTRODUCTION	1
1.1. Motivation	1
1.2. Surfactant Self-Assembly	4
1.2.1. Micelle Formation: Packing parameter	4
1.2.2. Wormlike Micelles (WLMs)	5
1.3. Nanoparticles	8
1.3.1. Plasmonic Nanoparticles	8
1.3.2. Zeta Potential	9
1.4. Nanoparticle-Surfactant Interactions	11
1.4.1. Self-Assembly in Micelle-Nanoparticle Solutions	11
1.4.2. Plasmonic Nanofluids	13
1.5. Computational Modeling of Complex Fluids	14
1.5.1. Hierarchy of Simulation Techniques	14
1.5.2. Simulations of Surfactant and Nanoparticle Solutions	16
1.6. Scope and Objective	17
CHAPTER 2 DYNAMICS AND SCISSION OF RODLIKE CATIONIC SURFACTANT MICELLES IN SHEAR FLOW	20
2.1. Introduction	20

2.2.	Simulation Methods	24
2.2.1.	The CGMD Surfactant Model	24
2.2.2.	Assembling and Equilibrating a Rodlike Micelle	27
2.2.3.	Molecular Dynamics Simulations of Micelle Dynamics in Shear Flow	28
2.2.4.	Determination of Micelle Relaxation from Flow-Induced Stretched Configurations	29
2.2.5.	Calculation of Instantaneous Length and Orientation of the Micelle	29
2.3.	Results and Discussion	30
2.3.1.	Orientational Dynamics in Shear Flow	30
2.3.2.	Structure Relaxation and Stretching Forces	38
2.3.3.	Flow-Induced Micelle Scission	40
2.4.	Conclusions	43
 CHAPTER 3 SELF-ASSEMBLY OF NANOPARTICLES WITH SURFACTANT MICELLES		45
3.1.	Introduction	45
3.2.	Simulation Methods	48
3.3.	Results and Discussion	51
3.3.1.	Self-assembly of CTAC Surfactants with NPs	51
3.3.1.1.	Kinetics of NPSC Formation	56
3.3.2.	Self-Assembly of NPSCs with Rodlike Micelles	59

3.3.2.1.	Surfactant Exchange Dynamics	61
3.3.2.2.	Energetics of Junction Formation	62
3.4.	Conclusions	63

**CHAPTER 4 MICROSTRUCTURE AND RHEOLOGY OF MIXTURES
OF NANOPARTICLES AND WORMLIKE MICELLES 65**

4.1.	Introduction	65
4.2.	Simulation Methods	67
4.2.1.	The CG MD Model	67
4.2.2.	Viscosity Calculation from MD Simulations	69
4.2.2.1.	Equilibrium MD: Pressure Fluctuations	69
4.2.2.2.	Non-equilibrium MD (NEMD): SLLOD Algorithm	70
4.2.2.3.	Reverse NEMD (RNEMD)	71
4.2.3.	MD Simulations of WLM-NP Solutions	72
4.3.	Results and Discussion	74
4.3.1.	Equilibrium Rheology	74
4.3.2.	Shear Rheology	79
4.4.	Conclusions	89

**CHAPTER 5 INFLUENCE OF SALT TYPE AND CONCENTRATION
ON THE MORPHOLOGY OF SURFACTANT MICELLES 91**

5.1.	Introduction	91
5.2.	Simulation Methods	95
5.2.1.	Effect of Salt Concentration on Micelle Growth Kinetics	95

5.2.2.	Effect of Salt Type on Micelle Growth	96
5.3.	Results and Discussion	98
5.3.1.	Micelle Growth Kinetics: Effect of Salt Concentration	98
5.3.2.	Zero-Shear Viscosity	101
5.4.	Conclusions	104
CHAPTER 6 SUMMARY AND FUTURE OUTLOOK		106
6.1.	Introduction	106
6.2.	Configurational Dynamics and Scission of a Rodlike Micelle	109
6.3.	Self-Assembly at the Nanoparticle-Surfactant Interface	111
6.4.	Rheology of Micelle-Nanoparticle Solutions	112
6.5.	Effect of Salt Type and Concentration on Micelle Formation	115
6.6.	Recommendations for Future Work	116
6.6.1.	Effect of Nanoparticle Charge, Surface Chemistry and Size on the Self-Assembly and Rheology of Wormlike Micelle-Nanoparticle Solutions	116
6.6.2.	Linear Viscoelasticity	117
6.6.3.	CGMD Simulations using Implicit Solvent Models	120
6.6.4.	Extensional Rheology of Micelle-Nanoparticle Solutions	121
REFERENCES		123

LIST OF FIGURES

Figure 1.1: Packing parameter and predicted micelle morphologies for different molecular architectures of surfactants in micelle solutions 3

Figure 1.2: Diagram of ion distribution around a negatively charged particle and schematic of the electric potential at the surface, Stern layer and Slipping plane 10

Figure 1.3: A hierarchy of molecular modeling and simulation techniques 15

Figure 2.1: AA and CG representation of (a,b) cationic CTA⁺ surfactant and (c,d) hydrotropic Sal⁻ salt respectively 25

Figure 2.2: Schematic of NEMD simulations. CTA⁺ surfactants (purple heads and green tails) groups, Sal⁻ ions (yellow), sodium (red) and chloride (blue) ions and water (cyan), (b) Schematic of the micelle axis and definitions of angles used to characterize flow-alignment 28

Figure 2.3: Plots of θ vs. time t for various Wi 31

Figure 2.4: Plots of $p(\theta)$ at various Wi . The dotted line represents a uniform distribution and the vertical bars show the standard deviation of $p(\theta)$ at $Wi = 0$ within each interval 32

Figure 2.5: Plot of $\Delta\theta$ as a function of Wi . The solid line is a power law fit with an exponent of -0.31 which is in close agreement with experimental and theoretical predictions of -1/3 33

Figure 2.6: (Top left) Flow-aligned, (Top right) gradient-aligned, (Bottom left) misaligned (in the xy plane), and (Bottom right) misaligned (in the yz plane) states (not to scale) 34

Figure 2.7: $p(\varphi)$ at various Wi for $Wi > 1$. The black line indicates a slope of -235

Figure 2.8: Normalized tumbling frequency f versus Wi . Open circles indicate stochastic diffusion regime while filled circles lie in the flow-aligned regime. Power law fitting in the flow-aligned regime yields $f \sim Wi^{0.68}$ 36

Figure 2.9: Mean squared angular deviation vs. time for $Wi = 0$ 37

Figure 2.10: Pair potential energy $\Phi^*(l)$ (black dots) and probability distribution of length $p(l)$ (blue triangles) from the length relaxation simulations are plotted as a function of l . Snapshots at different locations show a) stretched micelle ($l \approx 7$ nm), b) micelle with most probable length $l \approx 5.4$ nm, and c) bent micelle ($l \approx 4.7$ nm) 39

Figure 2.11: $\Phi^*(l)$ and l versus t showing micelle scission for $Wi = 76$. Snapshots at different locations show a) stretched micelle ($t \approx 8$ ns), b) micelle with most probable l ($t \approx 16$ ns) and c) micelle after scission ($t \approx 62$ ns) 41

Figure 2.12: $\Phi^*(l)$ vs. t for 4 different Wi as indicated. Dotted lines indicate the range for micelle scission for $Wi > 70$ 42

Figure 3.1: Hydrophobic NP with an uncharged surface and core (C1 particle type) (yellow). (b) Metal NP with a charged CG surface (Q0 particle type) (yellow) and an uncharged core (C1 particle type) (green). (c, d) Snapshots of the self-assembled NPSCs. CG water, ions and excess surfactants are not shown for the sake of clarity. Color scheme: NPs (yellow), CTA+ head group (violet) and CTA+ tail groups (cyan).

(c) Corona-like monolayer with the tail groups of CTA⁺ physically adsorbed on to the NP surface. (d) Vesicle-like bilayer with the head groups of the inner layer electrostatically attracted to the NP surface and the tail groups of the outer layer interlinked with the tail groups of the inner layer 52

Figure 3.2: (Left) Snapshot showing a closer look at the vesicular structure. Surfactants that obstruct a direct visualization of the inner layer were removed for clarity. Concentric circles are used to depict the two different layers of the NPSC. (Right) Side view of same snapshot 53

Figure 3.3: Effect of zeta potential (ζ) on metal NP-surfactant bilayer formation. The radial distribution function g_{surf} of the surfactant head groups as a function of distance r from the center of mass of the NP for four different values of $|\zeta|$, namely 0 mV (red), 28.98 mV (green), 39.90 mV (blue) and 46.75 mV (pink). The first peak, at a distance almost equal to the radius of the NP, indicates the inner layer and the second peak indicates the outer layer of the vesicle. Representative snapshots of the system at $t = 1 \mu s$ are shown for each case 55

Figure 3.4: Plot of the number of surfactants adsorbed onto the NP surface vs. time during the formation of the bilayer. The growth of the inner layer (brown), outer layer (orange) and the entire bilayer (green) are all shown separately. The inset shows the growth kinetics of the inner layer during the first 10ns of simulation 57

Figure 3.5: Junction formation between a NPSC and rodlike micelle. Snapshots of the CGMD simulation system before and after junction formation for the (a, b) corona-like NPSC and (c, d) vesicle-like NPSC. In order to differentiate between the CTA⁺

surfactants of each species they have been colored differently. CTA⁺ in the micelle is represented by red head groups and pink tail groups whereas CTA⁺ in the NPSC is represented by violet head groups and cyan tail groups. NP (yellow), Sal⁻ (orange), Na⁺ (green) and Cl⁻ (tan) counter ions are also shown 58

Figure 3.6: Surfactant exchange rates during junction formation. A plot of the total number of surfactants present in the (a) vesicle-like (blue) and (b) corona-like (blue) (right hand side Y-axis) and the micelle (red) (left hand side Y-axis) as a function of time clearly indicating the net transfer of surfactants from the micelle to the NPSC. Dotted black line in both cases indicates a \sqrt{t} dependence which suggests a diffusion-limited exchange process 60

Figure 3.7: Energetics of junction formation. A plot of the summation of pair potential energies \square of the NP, CTA⁺ and Sal⁻ complex as a function of time indicating a decrease in \square of ~ 1050 kJ/mol associated with junction formation in the case of a vesicle-like NPSC bridging with a rodlike micelle 63

Figure 4.1: Schematic of nanoparticles used in simulations. (b) Schematic of the velocity profile in the shear gradient plane in a RNEMD simulation. (c) Schematic of the micelle-NP complex used to study the rheology 73

Figure 4.2: Zero-shear viscosity η_0 as a function of φ_p for different values of R and for a fixed $C_D = 0.25$ M. η_0 increases linearly with φ_p and non-monotonically with increase in R 74

Figure 4.3: Microstructures observed in simulations at various nanoparticle concentrations for $R = 0.1$. Number of micelle-NP junction increases with the NP concentration	75
Figure 4.4: Microstructures observed in simulations at various nanoparticle concentrations for $R = 1.0$. Number of micelle-NP junction increases and micelle branches vanish with φ_p	76
Figure 4.5: Nearest neighbor (NN) distance as a function of φ_p for $R = 1$ shows that NN distance $\sim \varphi_p^{-1/3}$. The red line indicates the fit	78
Figure 4.6: Shear stress and Normal stress as a function of Wi for $Wi < 1$. Shear stress scales linearly and N_1 scales quadratically. The dotted lines are the corresponding curve fit	81
Figure 4.7: Shear stress vs. Wi for $R = 0.1$ and $\varphi_p = 0.002$	82
Figure 4.8: Velocity profile at three different shear rates (Left to right) $Wi = 0.25$, $Wi = 4.76$, and $Wi = 22.1$	82
Figure 4.9: Shear viscosity as a function of shear rate for various salt and NP concentrations (a) $R = 0.1$, (b) $R = 0.33$, (c) $R = 0.67$, and (d) $R = 1.0$	84
Figure 4.10: Nematic order as a function of time at different shear rates at $C_D = 0.25$ M and $R = 0.33$. (b) Nematic order as a function of Wi . Insets show representative snapshots of the isotropic and nematic state	86
Figure 4.11: First normal stress difference N_1 vs (a) time at different shear rates and (b) Wi	88

Figure 5.1: Number of micelles N_m as a function of time for $R = 0.1$ and $R = 0.9$. Plots of N_m at other values of (R) are not shown for clarity	99
Figure 5.2: Dependence of the power law exponent $\alpha(R)$ on the salt/surfactant ratio, R . Error bars indicate data averaged over 10 different simulations for each data point	100
Figure 5.3: Zero-shear viscosity (η_0) for CTAC/SHNC system as a function of R showing a 35% increase in η_0 with the addition of salt. Line is just a guide to the eye	102
Figure 5.4: Snapshots of the largest self-assembled structure for $C_D = 0.34$ M and (a) $R = 0.1$, (b) $R = 0.25$, (c) $R = 1.2$, (d) $R = 1.6$ and (e) $R = 2.0$. Coloring scheme is as follows: CTA+ tail group (cyan), head group (yellow) and SHNC salt (red)	104
Figure 6.1: Plots of shear stress and shear strain as a function of time for a model surfactant micelle system in large-amplitude oscillatory shear flow using MD simulations. The stress response is sinusoidal and leads the applied strain by a phase angle, δ	120

LIST OF TABLES

Table 2.1: Bonded and non-bonded interaction parameters for all CG beads in the system	26
Table 3.1: Number of NPs, CTA+, Cl-, Na+ and Water (W) for different values of surface charge density (σ)	49
Table 3.2: Debye length ($1/\kappa$) and Zeta potential (ζ) for different values of NP surface charge density (σ)	54

Chapter 1

Introduction

1.1. Motivation

Surfactants are molecules that consist of two different chemical moieties that possess different solvophilic and solvophobic properties. Most commonly found surfactants are water soluble and consist of a hydrophilic head group and a hydrophobic tail group (typically a hydrocarbon chain). Surfactants can be nonionic (uncharged), cationic (positively charged), anionic (negatively charged) or even zwitterionic (consisting of both positive and negative charges). This amphiphilic character of surfactants results in their tendency to self-assemble into surfactant micelles with a rich variety of equilibrium structures. In aqueous solution, such molecules spontaneously aggregate in such a way that the head groups are solvated by water and the tail groups cluster and orient themselves in such a manner that they are shielded from the water molecules. Micellar self-assembly is a reversible process and is sensitive to a number of physicochemical conditions such as surfactant shape and concentration, solvent chemistry, salt concentration, salt type, temperature, pH and other non-equilibrium forces. Micelle solutions exhibit rich phase behavior and complex rheological properties including linear viscoelasticity and non-Newtonian flow properties.

Amongst micellar fluids, cylindrical and wormlike micelles (WLMs) have gained special interest and importance due to their structural similarity to polymers. They are referred to as “living” polymers or “equilibrium” polymers because their constitutive behavior is governed by

reptation dynamics but they also exist in a state of dynamic equilibrium between scission and recombination¹. Traditionally, WLMs have been used in several consumer and household products such as soaps, detergents, cleaning fluids and cosmetics². However, more recently they have found applications in the area of enhanced oil-recovery³, hydraulic fracturing⁴ and turbulent drag reduction⁵. For these applications, WLMs possess several advantages over more commonly used polymeric materials because of their resistance to shear degradation, ease of manufacturing, interactions with nanoscale or colloidal surfaces and most importantly, facile cleanup due to spontaneous dissolution upon dilution^{6, 7, 8}. Further, with rapid advancement in the area of nanotechnology, WLM fluids have been found to be a great template for the synthesis of active nanomaterials^{9, 10}. The ability to robustly tune the microstructure of the WLM fluid has given rise to a new method to create precisely controlled nanostructures.

It is important to note that in all of the above applications, there are one of two factors that are common and recurring. First, the close coupling between the molecular structure of the surfactant and the desired macroscopic properties of the fluid such as viscosity and flow behavior. Second, the coexistence of WLMs and colloidal particles. Recent research has suggested that nanoparticles can not only add functionality to the WLM fluid but also act as viscosity/rheology modifiers.

The goal of this thesis is to develop computational modeling techniques that possess sufficient spatiotemporal resolution to directly visualize the structure, dynamics and self-assembly of WLMs and micelle-nanoparticle solutions, at the molecular level, under both equilibrium and non-equilibrium conditions. The remainder of this chapter will present a review of the current literature, broadly summarize relevant modeling efforts, and define the objectives and primary focus of this work.








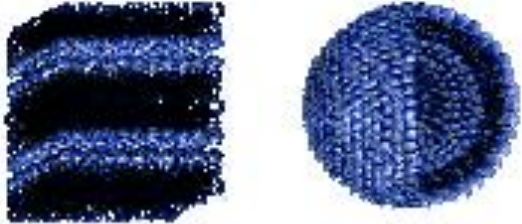
Packing parameter, p	Packing geometry	Micelle morphology
$p < 1/3$		 Sphere
$1/3 < p < 1/2$		 Rod
$1/2 < p < 1$		 Branch
$p \sim 1$		 Bilayer Vesicle

Figure 1.1: Packing parameter, molecular structure and predicted micelle morphology¹¹

1.2. Surfactant Self-Assembly

1.2.1. Micelle formation: Packing parameter

Surfactants are sparingly soluble as monomers in aqueous solutions and beyond a critical value, referred to as the critical micelle concentration (CMC), they spontaneously self-assemble into micelles. From a thermodynamics point of view, micelle formation is a direct consequence of the large entropic penalty arising from the exposure of the long hydrocarbon tail of the surfactant to water. Above CMC, depending upon the physicochemical conditions, various micelle morphologies including spheres, cylinders, WLMs and branched micellar networks can coexist in a single phase. Israelachvili¹² introduced the idea of characterizing the molecular structure of the surfactant using a packing parameter,

$$p = \frac{V}{al} \quad (1-1)$$

where V is the molecular volume occupied by the surfactant, a is the effective area occupied by the head group and l is the length of the hydrocarbon tail. Among these parameters, V and l can be roughly estimated based on the number of carbon atoms in the hydrocarbon tail as

$$l_c \approx (1.54 + 1.265n_c) \text{ \AA} \quad (1-2)$$

$$V_c \approx (27.4 + 26.9n_c) \text{ \AA}^3 \quad (1-3)$$

However, the effective head group area, a , is not a constant for a given molecule and is more difficult to estimate experimentally. To a first approximation, the preferred micelle shape can be predicted *a priori*, using the packing parameter (Fig. 1.1). Specifically, for $p < 1/3$, spherical micelles are favored, whereas cylindrical and rodlike micelles are favored for $1/3 < p < 1/2$. Branched micelles are preferred for $1/2 < p < 1$ and finally, when $p \sim 1$, bilayers and vesicular

structures are formed. For ionic surfactant systems, such as the ones we will be focusing on in this study, the effective area of the hydrophilic head group will be strongly dependent on the extent to which the electrostatic repulsion between the head groups is screened by the presence of counterions in solution. This can be quantitatively estimated by calculating the Debye length, $1/\kappa$, which is defined as,

$$\kappa^{-1} = \left(\frac{\epsilon_0 \epsilon_r k_B T}{2 N_A e^2 I} \right) \quad (1-4)$$

where ϵ_0 and ϵ_r are the permittivity of free space and relative permittivity of the solvent respectively, k_B is the Boltzmann constant (1.38×10^{-23} J/K), T is the absolute temperature, N_A is the Avogadro number (6.022×10^{23} mol⁻¹), e is the elementary charge (1.602×10^{-19} C), and I is the ionic strength of the solution¹³. Addition of salt to surfactant solutions would obviously increase the ionic strength of the solution thereby decreasing the Debye length. This would result in an increase in the packing parameter which would promote sphere-to-rod transition and consequently aid the formation of longer micelles.

1.2.2. Wormlike micelles (WLMs)

Initially, the rodlike micelles that are formed due to sphere-to-rod transitions are fairly short and rigid. They have two hemispherical end caps, each with an energy, E_{cap} , at either end. A further increase in the packing parameter would promote the axial growth of rodlike micelles resulting in the formation of semiflexible and flexible thread-like structures that are referred to as WLMs. As mentioned earlier, although WLMs are very similar to polymers they are held together by weak non-bonded interactions which are not immune to breakage by thermal fluctuations. The energy required to break a micelle into two can be estimated based on the energy required to create

two new end caps, which is given by $2E_{cap}$. This mechanism for micelle breakage has been proposed by several researchers and E_{cap} has been quantitatively estimated to be $\sim O(10)$ $k_B T$ from experimental, theoretical as well as computational calculations.

WLMs are also known to be extremely polydispersed in solution. Cates and Candau¹⁴ developed a mean field theory which accounted for the breakage and recombination kinetics of micelles to study the distribution of micelle lengths in solution. They showed that the interplay between entropy and end cap energy of the micelles results in a broad, exponential distribution of micelle lengths which is given by,

$$p(N) \propto \exp(-N/\langle N \rangle) \quad (1-5)$$

where $\langle N \rangle$ is the ensemble average of the micelle length. However, this model is applicable only for the case of non-ionic micelles and charge neutral micelles i.e., in the presence of an equimolar amount of salt. Mackintosh et al.^{15, 16} extended the Cates model for ionic micelles to account for electrostatic interactions between head groups and counterions and suggested that the probability distribution follows a log-normal distribution as compared to the exponential distribution in the previous case. Recently, coarse-grained molecular dynamics simulations have been able to capture predicted distributions from both theories¹⁷. However, the conclusions from the study also indicate that there is no universal distribution of micellar lengths for a given solution whether it is an ionic or a charge neutral micelle system.

From the above discussion, it is clear that the morphology of WLMs is a strong function of the salt concentration. Another important factor is the salt type. Experiments have shown that organic, hydrotropic salts tend to have a much more significant effect on the structure and rheology of micellar solutions as compared to inorganic salts. For example, it has been observed that the

equilibrium viscosity of a solution of cationic cetyltrimethylammonium bromide (CTAB) surfactant can be increased by ~3 orders of magnitude by adding very small amounts of sodium salicylate (NaSal) whereas this cannot be achieved by the addition of simple salts such as sodium nitrate (NaNO_3), sodium chloride (NaCl) and potassium bromide (KBr)¹⁸. Such anomalous viscosity variations are attributed to the ability of NaSal to more effectively screen the electrostatic repulsion between the cationic head groups. Molecular simulations have shown that the bulky hydrophobic ring of the NaSal salt tends to get buried in between the head groups thereby bringing the head groups closer^{19, 20}. This reduces the effective area of the surfactant head group and increases the packing parameter, thereby promoting growth of micelles and transition to longer structures. Experiments also indicate a rapid decrease in the equilibrium viscosity with further addition of salt which is attributed to the onset of branching in micelle solutions. Branching in micelles provides a new, faster mode of stress relaxation through a sliding mechanism by which the micellar branches can slide along the contour of the micelle. In the case of the CTAB/NaSal system, another anomaly is the occurrence of a double peak in the zero-shear viscosity as a function of the salt concentration. The second peak is an indication of an elastic network formation that occurs due to several branched micelles connecting with each other which in turn results in a slight increase in the viscosity. On further addition of salt, this network breaks down due to the presence of excessive salt in the system which results in a decrease in viscosity. Recently, this behavior has also been demonstrated through large-scale molecular dynamics simulations¹⁷.

WLM solutions exhibit a rich range of rheological behavior including Newtonian, rheopexy, i.e., an increase in shear viscosity with time at constant shear rate, shear thinning, i.e., a decrease in shear viscosity with increasing shear rate, shear-induced structure (SIS) formation that manifests as shear thickening, and shear banding. The hypothesis is that SIS formation in micelle

solutions is triggered by the end-to-end collision of flow-aligned rodlike micelles which results in the formation of longer WLMs²¹. While this hypothesis is generally accepted, molecular investigations of these phenomena are yet to be developed. One of the goals of this thesis is to be able to present a modeling framework that is capable of directly observing the configurational dynamics of rodlike micelles in shear flow. Further, most SIS transitions reported in literature are reversible and the gel tends to disintegrate as soon as the flow is stopped. Recently, a microfluidics-assisted, robust laminar flow process has been developed to create irreversible, permanent nanogels that persist even after cessation of flow²². A recent study conducted by Raghavan and co-workers²³ indicates that certain cationic surfactants, in the presence of certain organic counterions with aromatic character, have strong birefringence on shear. Importantly, the birefringent structures persist for hours after shear cessation, even though there was no permanent phase transition. Such materials can serve as excellent templates for the synthesis of soft nanomaterials. It has also been shown that the critical shear rate for the onset of shear thickening due to SIS formation is strongly dependent on the molar ratio of salt to surfactant, $R^{21,24}$. The shear thickening regime in such systems is followed by a shear thinning regime which is possibly due to the flow-alignment and breakage of WLMs in solution.

1.3. Nanoparticles

1.3.1. Plasmonic nanoparticles

Nanoparticles are colloidal particles that are in the size range of 1-100 nm. They are ubiquitous and present in various complex shapes and sizes. In this work, we will focus specifically on noble metal nanoparticles, such as gold and silver, and their properties. The ability of noble

metal nanoparticles to manipulate light at the nanoscale has been of interest to mankind since the late 1800's²⁵. However, over the last 2-3 decades, research and development of new nanoscale materials with advanced optical properties has burst forth due to advancements in the field of nanotechnology. Among the many attractive properties that metal nanoparticles possess, one important phenomenon is referred to as localized surface plasmon resonance (LSPR). When light is incident on a particle, the free conduction electrons in the particle surface may undergo a collective oscillation at the same frequency of the incident light and this phenomenon is known as LSPR. The effect of this phenomenon is the presence of a sharp absorption and scattering peak. The absorption peak and other related optical properties depend upon several factors including particle size, shape and material. For example, gold nanoparticles absorb light in the ~520 nm wavelength whereas silver nanoparticles absorb in the range of ~410 nm. However, aggregation of gold nanoparticles in solution will result in an increase in the size of the aggregate which would further result in a shift in the peak which can be characterized by a corresponding red-to-blue color change. This suggests that the particle size is also an important parameter in determining optical activity. Another important parameter is the surface charge on the nanoparticle. In this work, we will be focusing only on negatively charged metal nanoparticles.

1.3.2. Zeta potential

The effect of surface charge on the stability of the nanoparticle is characterized by the zeta potential, ζ ¹³. Consider a negatively charged nanoparticle in an aqueous solution that contains dissolved ions (Fig. 1.2). In order to achieve charge neutrality, the positively charged ions in the

solution will form a close shell around the negatively charged nanoparticle due to Coulombic attractive forces.

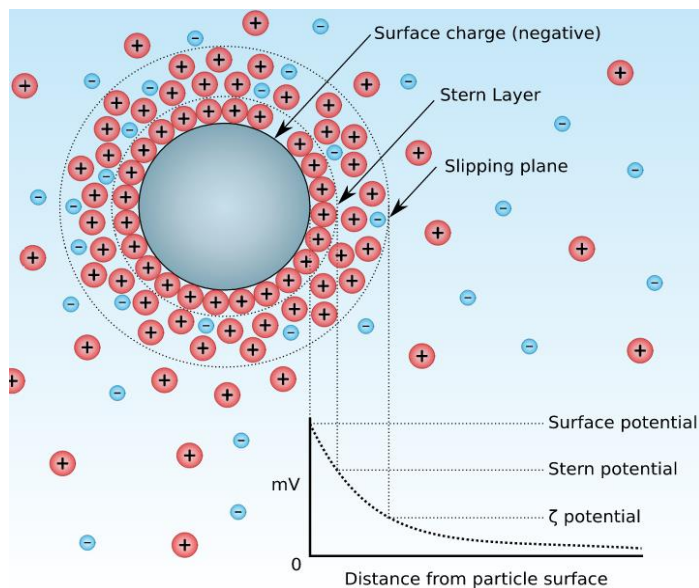


Figure 1.2: Diagram of ion distribution around a negatively charged particle and schematic of the electric potential at the surface, Stern layer and Slipping plane.

This shell like inner layer is referred to as the Stern layer and the electric potential at this plane is the Stern potential. The presence of bound surface charges and associated counterions will act as an effective capacitor with a compressible dielectric filling. Due to the increased concentration of ions at the colloidal surface relative to the bulk, there will be a gradient in the concentration of ions that decreases from the surface of the particle until it reaches the bulk ion concentration. Thermal motion of the solvent molecules and ions tends to create a second, more spread-out layer that can span distances on the order of nanometers. This layer of increased ion concentration is typically referred to as the diffuse layer. The characteristic thickness of the

electrical double layer is the Debye Length, $1/\kappa$, which has been defined earlier. The plane that separates the mobile fluid from the fluid that remains attached to the nanoparticle surface is referred to as the slipping plane and the electric potential at this plane is the zeta potential. Typically, ζ is experimentally determined using electrophoretic mobility measurements or estimated theoretically using the Derjaguin-Landau-Verwey-Overbeek (DLVO) theory¹². Alternatively, ζ and $1/\kappa$ can be directly calculated from molecular simulations. We will discuss this in more detail in Chapter 3.

1.4. Nanoparticle-Surfactant Interactions

1.4.1. Self-assembly in micelle-NP solutions

As mentioned earlier, surfactant micelles encounter colloidal and nanoparticles in several areas of application and it is important to understand their coexisting behavior in order to develop the ability to robustly tune and precisely control the desired properties of the resultant fluid. Due to their amphiphilic nature, surfactants prefer to partition at the solid-liquid interface that exists due to the presence of solid colloidal particles in a continuous liquid (fluid) medium. The nature of self-assembly greatly depends on the surface chemistry of the colloid and the corresponding interactions between the head and tail groups. For example, if the colloidal surface has a strong affinity to the head group, either due to van der Waals or electrostatic interactions or a combination of both, then the surfactant will adsorb on to the surface of the particle in a head-on fashion. On the contrary, if the particle has a strong affinity to the tail group and repels the head group, then a tail-on approach can be expected. At very low concentrations of surfactant and/or very weak attractive and repulsive forces between the colloidal surface and the head and tail groups we can

expect to see partial tail-on and head-on orientations during self-assembly. These self-assembly processes are typically enthalpy dominated²⁶.

In the presence of a macroscopic interface, it has been shown that micellar solutions can be forced towards reaching an ordered nematic phase due to the adsorption and structuring of individual surfactant molecules at the interface. This is achieved due to the presence of a planar surface which disrupts the symmetry (isotropic state) of the micellar fluid. However, as the surface gets smaller and less planar (increase in curvature), such as in the case of nanoparticles, it is not clear if this behavior would still be valid. Several attempts have been made to characterize the self-assembly of mixtures of WLMs and nanoparticles in aqueous solution. However, existing results and the corresponding hypothesis therein seem to be somewhat contradictory. Even rheological characterization of such systems show contrasting behavior and the trends observed are vastly different. The range of experimental techniques used to explore such systems include rheology, small angle X-ray scattering (SAXS)²⁷, small angle neutron scattering (SANS) and isothermal titration calorimetry measurements²⁸. The general hypothesis is that the nanoparticles integrate themselves within the micellar network, therefore giving rise to a micelle-nanoparticle double network with enhanced viscosity and viscoelasticity. However, the mechanism of self-assembly, the synergistic effects between nanoparticles and WLMs in solution, and the underlying interactions remain unclear. Theoretical and modeling efforts in this topic are limited to ad hoc models and pre-assembled structures that fail to include solvent effects and/or cannot capture relevant time/length scales. Jodar-Reyes and Leermakers^{29, 30} have performed self-consistent field theoretic calculations of rodlike micelles confined between two surfactant-covered surfaces. Their results suggested that micellar stalks can bridge between hydrophilic surfaces on to which a double layer of surfactants are adsorbed and that this would happen when the end cap energy of the

micelle, E_{cap} , is higher than the free energy required for junction formation. They also claim that it is impossible to have micelle-NP junctions in the case of a monolayer of surfactants adsorbed on to a hydrophobic colloidal surface.

1.4.2. Plasmonic Nanofluids

The addition of colloidal particles to viscoelastic polymer solutions has provided a great method to create light-weight, next-generation materials²⁴. Such materials are referred to as polymer nanocomposites (PNCs) and have been shown to possess superior material properties such as mechanical strength, flexibility and thermal conductivity even at very low nanoparticle filler loadings. A thorough review of all the experimental and computational efforts in the area of PNCs and polymer-grafted nanoparticle systems has been presented elsewhere³¹. In this study, we focus on micellar systems or “living polymers” and their self-assembly with nanoparticles. Recently, a new method has been developed to create stable, robustly tunable plasmonic nanogels using noble metal nanoparticles and WLMs. However, the mechanisms that govern the underlying self-assembly and the coupling between the microstructure and macroscopic properties of such solutions is relatively poorly understood. It is possible that the presence of WLMs prevents nanoparticle aggregation and help preserve their optical properties while nanoparticles act as optically functional viscosity modifiers. Such solutions exhibit complex behavior such as a non-monotonic increase in zero-shear viscosity with particle concentration and a rich range of rheological behavior including Newtonian, rheopexy, shear thickening and shear banding. Understanding the rheological and flow properties of these complex fluids are important from a

processing perspective. This work will make an attempt to fill the knowledge gap in this area using computational modeling techniques that can span appropriate time/length scales.

1.5. Computational Modeling of Complex Fluids

1.5.1. Hierarchy of simulation techniques

A schematic representing a hierarchy of molecular modeling and simulation techniques is shown in Fig. 1.3. The typical spatial and temporal scales that can be accessed by each of these techniques is also provided. Ab-initio quantum mechanical methods are limited to studying systems containing a few hundred electrons over femtosecond timescales. Quantum mechanical methods such as density functional theory (DFT) have been used in the past to study the molecular structure of highly dilute surfactant systems³². However, these methods cannot be used to study supramolecular aggregates and clusters of micelles. All-atom (AA) simulations are extremely useful in investigating the structure of macromolecules such as proteins, polymers, micellar aggregates and biological membranes. AA simulations give detailed atomistic descriptions of every single atom in the system and can access timescales on the order of 10-100 nanoseconds^{33, 34, 35, 36, 37, 38}. While this is good enough to examine radial distribution functions and energetics of the system, this is not enough to probe the configurational dynamics, self-assembly and rheology of macromolecular fluids such as polymers, wormlike micelles, proteins, DNA etc. Further, such detailed representations are unnecessary and irrelevant as far as macromolecular behavior is concerned. A slightly better approach is to use a united-atom description which typically neglects all the (light) hydrogen atoms and the bond vibrations associated with those atoms. This results in a slight increase in efficiency but is not enough to overcome the above mentioned limitations.

Several attempts have been made to develop reliable coarse-grained (CG) models that combine three or four heavy atoms into a single CG bead, which would effectively remove the ultrahigh frequency motions and reduce the number of degrees of freedom in the system^{39, 40}. This would allow sampling on the order of microseconds while still being able to retain chemical specificity of the molecules and explicitly account for hydrodynamic effects due to solvent motion.

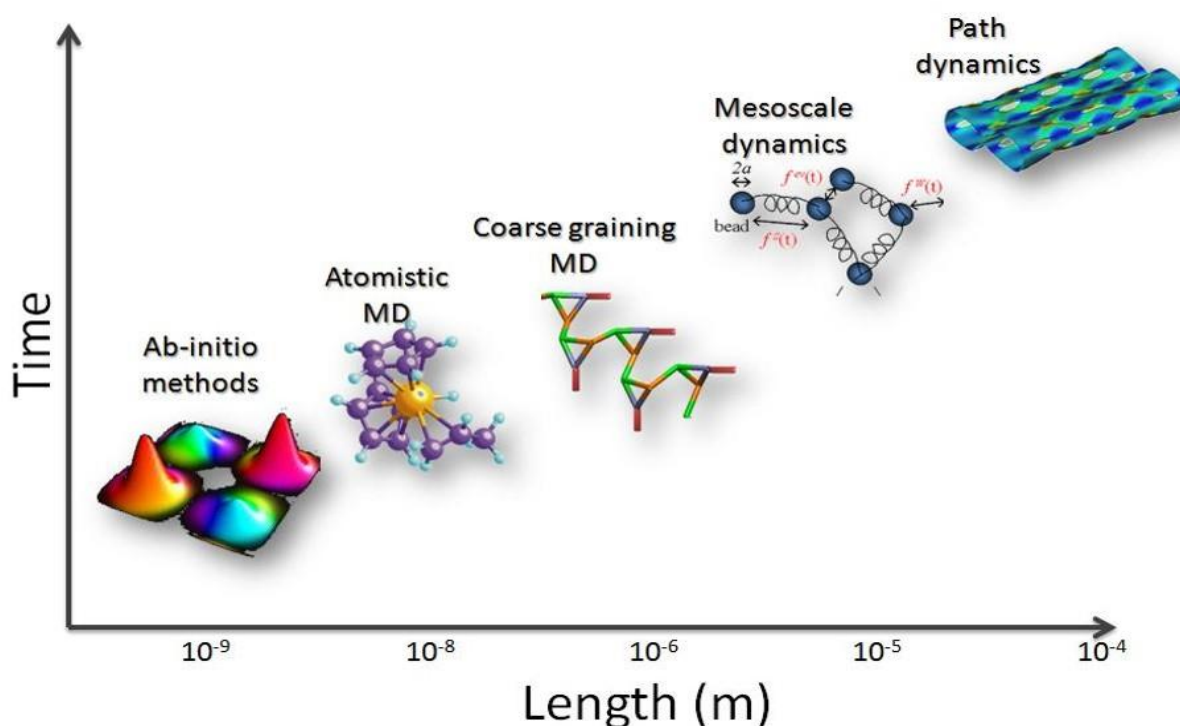


Figure 1.3: A hierarchy of molecular modeling and simulation techniques.

Beyond the CG approach lies the realm of mesoscopic simulations. This includes Brownian Dynamics (BD), Dissipative Particle Dynamics (DPD) simulations and so on. These are stochastic simulation models in which the solvent is represented by a thermal bath and the macromolecule is represented by an ad hoc micromechanical model, for e.g., bead-rod or bead-spring model. In the

bead-rod model, the beads are a collection of 10-20 monomers that can be assumed to be in concerted motion and the rod length is typically referred to as the Kuhn length (\approx twice the persistence length). The bead-spring model is slightly more coarse-grained and usually the spring is a non-linear entropic spring. These models have been extensively used to study the configurational dynamics of polymeric systems under confinement, various flow fields and solvent conditions. DPD simulations are stochastic simulations but are slightly closer to CG models in the fact that the solvent is modeled by CG particles and therefore such methods are more suitable for studying systems where the hydrodynamic interactions become important, such as in micelle solutions^{41, 42}. Finally, there are also continuum-level constitutive modeling methods that are often used to study the phase behavior of polymeric liquids. These techniques focus on modeling mean field quantities such as velocity, pressure and viscoelastic stress. They do not attempt to capture microstructural details such as molecular motion and self-assembly. Examples of such methods include direct numerical simulations (DNS) and self-consistent field (SCF) theories.

1.5.2. Simulations of surfactant and nanoparticle solutions

The design and development of computer simulations and related techniques to study amphiphilic surfactants, polymers and nanoparticles has become crucial to establish relationships between the nanoscale structure and macroscopic properties of these important class of soft materials. Molecular explorations of such systems have increased exponentially over the last two decades. Attempts to characterize surfactant structure and provide quantitative estimates of the critical micelle concentration, aggregation number and phase behavior of ionic and nonionic surfactant micelle solutions through various modeling techniques have been largely successful for

small, concentrated systems. Studies have also explored the behavior of surfactants at liquid-liquid (oil-water), vapor-liquid (air-water) and solid-liquid interfaces (nanoparticle/planar surfaces). Leermakers et al.^{29, 30} have made several contributions in this area through the development of SCF theoretic frameworks. Groot has studied the formation of a polymer-surfactant complex in aqueous solution using DPD simulations⁴¹. Lu et al. provided the first ever simulations of surfactant-assisted protein refolding using lattice models⁴³. Wang and Larson have shown the effect of salt type and concentration on the structure of cationic CTAB micelles²⁰. Sangwai et al. have shown sphere-to-rod transitions and coalescence of micelles due to salt-induced electrostatic screening effects^{19, 44}. For nanoparticle-surfactant systems, small-scale MD simulations on the order of a few hundred picoseconds have been performed on preassembled systems to show that surfactant adsorption on to the surface of a semiconductor or metal nanoparticle is energetically favorable^{45, 46}. Therefore, the collective literature suggests that molecular level explorations of micellar systems has been limited to nanosecond time scales and systems that consist of a few thousand particles at most. In this work, we will be developing suitable CG models that can span microsecond timescales for systems that consist of $\sim O(10^5)$ number of particles in the system.

1.6. Scope and Objective

As mentioned above, the multi-scaled nature of both the structure and properties of WLMs and WLM-nanoparticle mixtures requires an equally multi-scaled approach to study them. The goal of this thesis is to develop a rigorous coarse-grained molecular model to effectively describe model cationic surfactants, for e.g., cetyltrimethylammonium chloride (CTAC), hydrotropic salts, such as NaSal, and nanoparticles with both hydrophobic and charged, hydrophilic surfaces. The

nanoparticles utilized in this work are primarily spherical and in the size range of 3-5 nm. The CG framework that is developed herein will be used to investigate the structure, dynamics, self-assembly and rheology of mixtures of surfactant micelles and nanoparticles at the molecular level. The CG models and corresponding force field parameters for each of the molecules are listed in the respective chapters. The remainder of the thesis is organized as follows.

In Chapter 2, we discuss the configurational dynamics of a rodlike cationic surfactant micelle in shear flow. While the dynamics of a single polymer chain in various flow fields is clearly understood, the same cannot be said about self-assembled rodlike or WLMs. The study presented here provides the first and only way to directly visualize the dynamics of micelles under shear flow. Specifically, we characterize an effective parameter to distinguish between diffusive and flow-aligned regimes, estimate tumbling frequencies, orientational distributions and stretching forces for rodlike micelles. Further, we also predict micelle scission barriers and compare our predictions with stochastic simulations and mesoscopic theories.

In Chapter 3, we focus on identifying molecular mechanisms of self-assembly in mixtures of nanoparticles and surfactants in solution. The effect of nanoparticle surface functionalization and charge on the resulting self-assembly is also discussed. First we show that surfactants can self-assemble on the surface of a nanoparticle to form a corona-like monolayer or a vesicle-like bilayer. Next we show that these self-assembled nanoparticle-surfactant complexes can further self-assemble with rodlike micelles via an end cap attachment mechanism to form electrostatically stabilized junctions. The dynamics of surfactant exchange and the energetics associated with junction formation is discussed.

Chapter 4 focuses on the rheology of WLM-nanoparticle solutions. The effect of nanoparticle volume fraction and the molar ratio of salt to surfactant, R , on the equilibrium

viscosity is discussed. We show that nanoparticles materially participate in the micellar network and identify relationships between the microstructure and rheology of such systems. Specifically, two mechanisms result in an increase in viscosity with increase in nanoparticle volume fraction. First, the effective lengthening of micellar structures leads to longer structures. Second, the presence of nanoparticle-mediated junctions results in a decrease in the number of micellar branch points that can act as sliding junctions. Finally, we use non-equilibrium MD simulations to show shear thinning and shear-induced isotropic-to-nematic transitions in such solutions. The first normal stress difference, N_1 , and its dependence on time and shear rate is also discussed.

In Chapter 5 we discuss the effect of salt type and salt concentration on the morphology and rheology of micellar fluids. We compare the range of structures obtained from simulations of aqueous solutions of CTAB surfactant in the presence of three different salts, namely, NaCl, NaSal and 3-hydroxy naphthalene-2-carboxylate (SHNC). SHNC is a hydrotropic salt which is very similar to NaSal but has an additional ring in its tail group. It has been shown that the additional ring structure results in stronger π - π and cation- π interactions, which in turn results in complex rheological behavior. Effect of salt type and concentration on the dynamics of micelle formation is also discussed.

Chapter 6 provides a summary of all the results in this work and proposes directions for future work. Some preliminary investigations of relevant phenomenon in micellar systems, as well as attempts to develop algorithms and computational methods to explore linear viscoelasticity in complex fluids using molecular dynamics simulations that mimic small-amplitude oscillatory shear (SAOS) flow experiments are discussed. Finally, additional methods of optimizing and increasing the computational efficiency of computer simulations in order to access longer time and length scales is discussed.

Chapter 2

Dynamics and Scission of Rodlike Cationic Surfactant Micelles in Shear Flow

[Adapted (in part) from *Phys. Rev. Lett.* **114**, 158302 (2015)]

2.1. Introduction

Thermodynamic self-assembly in surfactant solutions is known to result in various micelle morphologies such as spheres, cylinders, vesicles, and lamellae. The rich diversity in equilibrium morphologies is of great fundamental and practical interest in applications ranging from detergency to targeted drug delivery. Amongst micellar structures, cylindrical and wormlike micelles are known to exhibit rich rheological behavior because micelle length and entanglement density depend greatly on the surfactant and salt concentration, salt hydrophobicity, temperature and flow shear. Specifically, depending on the surfactant concentration, chemical environment, and shear rate, cylindrical micelle solutions could exhibit Newtonian, shear thinning, or shear thickening behavior, which is accompanied by shear-induced structure (SIS) formation or shear banding^{21, 22, 47, 48, 49, 50, 51}.

Over the last couple of decades, significant progress has been made in trying to understand polymer dynamics under equilibrium and non-equilibrium conditions for applications in several areas including polymer processing, turbulent drag reduction and enhanced oil-recovery⁵². Further, single polymer manipulation has become increasingly important for several lab-on-a-chip

applications such as DNA separation^{53, 54} and stretching devices⁵⁵. To this effect, the configurational dynamics of single polymer molecules under various flow fields has been extensively investigated^{56, 57, 58, 59, 60, 61, 62}. The pioneering work in this area was done by Chu et al. who utilized video fluorescence microscopy techniques to directly visualize a dye-stained DNA molecule under conditions of simple shear⁵⁹ and uniaxial extensional flow⁶⁰ fields. Following this, several researchers have developed theoretical⁶², experimental and numerical⁶³ schemes to elucidate the dynamics of a single polymer chain. These include rheological experiments, mesoscopic theories and stochastic simulations such as Brownian Dynamics (BD) and Dissipative Particle Dynamics (DPD) simulations. More recently, the orientational distributions and tumbling dynamics of a single polyethylene oxide (PEO) molecule under shear flow has been characterized using CG MD simulations that explicitly account for hydrodynamic effects⁶⁴. The effect of chain length, solvent quality and confinement on the dynamics of these systems have also been studied in detail. While tremendous progress has been made in understanding the behavior of polymers, not much progress has been made in studying the dynamics of self-assembled systems.

Cylindrical and WLMs are structurally very similar to polymers but have an added layer of complexity in the form of a dynamic equilibrium that exists between scission and recombination of micellar structures¹⁴. Till date, we do not have any experimental techniques that have the ability to characterize the configurational dynamics of a single WLM in a flow field. This is because current experimental techniques lack the spatiotemporal resolution to directly observe micellar solutions in real time. Hence, the only way to study these systems is to use theoretical and numerical methods. While phenomenological, kinetic-theory inspired⁶⁵ and continuum-level constitutive models^{66, 67, 68, 69} have been developed to study the dynamics and rheology of cylindrical micelles, molecular-level explorations of flow-structure coupling in micelle solutions

is lacking. Understanding micelle structure and dynamics via faithful and systematic molecular simulations is an important and essential step in filling this knowledge gap. Briels et al.⁷⁰ have developed stochastic simulations (Brownian dynamics), in which parameters such as the persistence length were obtained from atomistic molecular simulations, to study dynamics and rheology of wormlike micelle solutions. In this study, we describe, for the first time, insights gained from a coarse-grained molecular dynamics (CGMD) study of cylindrical cationic micelles subjected to uniform and steady shear flow⁷¹. In CGMD, explicit solvent-salt-micelle interactions are incorporated by utilizing force fields which are validated against more detailed atomistic MD simulations. Several fundamental questions are addressed including the criterion that demarcates the Brownian (diffusive) and flow-aligned regimes, asymptotical scaling laws that characterize micelle configurational dynamics and their comparisons with stochastic theories of flexible and semi-flexible polymers, relationship between micelle energetics and length, and a mechanism of flow-induced micelle scission.

Cates and coworkers⁵⁰ suggested that the fundamental mechanism of SIS formation is end-to-end collisions between flow-aligned micelles, followed by the opening up of micelle end caps and micelle fusion to form longer micelles. These longer micelles tend to flow-align more easily because the rotational (angular) diffusion timescale τ_D of these rods increases significantly with micelle length ($\tau_D \sim L^3$), and this triggers a positive feedback mechanism that promotes formation of even longer micelles which eventually form networks. They also hypothesized that the onset of SIS formation occurs when τ_D of the micelles is comparable to the inverse shear rate, i.e., when the Peclet number $Pe \equiv S\tau_D$, is $O(1)$. Recent equilibrium MD simulations of cationic spherical micelles suggest that sufficient electrostatic screening is required to induce micelle fusion, which is more readily facilitated when ringed organic counter ions are present in salt to surfactant molar

ratio exceeding unity⁴⁴. For instance, benzoate ions physically adsorb onto the micelle-water interface and help neutralize the repulsive electrostatic interactions between the surfactant head groups, as characterized by the potential of mean force of binary interactions. This is consistent with experimental observations that hydrophobic salts such as benzoate or salicylate promote SIS formation and shear thickening in cationic micelle solutions^{18, 21}.

Hence, the literature suggests that satisfaction of two criteria is required for robustly inducing SIS in ionic micelle solutions, namely a mechanical one that requires that the inverse rate of flow deformation is comparable to that of the inherent rotational time scale of the micelle, and a chemical one that necessitates the counterion concentration to be large enough to provide sufficient electrostatic screening. In this work, we focus on studying the effects of shear flow on the configurational dynamics of a single cylindrical CTAC micelle in an aqueous solution containing NaSal salt while preserving the underlying physical chemistry and intrinsic self-assembled structure of the micelle. In the simulations, all chemical interactions, spontaneous rearrangements within the micelle structure and micelle shape/length fluctuations and angular diffusion are explicitly calculated. To date, atomistic non-equilibrium molecular dynamics (NEMD) simulations of micellar systems in presence of explicit solvent and electrostatic interactions are limited to nanosecond time scales. In the present study, we are able to conduct NEMD studies that span microseconds (\gg angular orientational relaxation time τ_R) by utilizing CG potentials of CTAC surfactant and NaSal salt in explicit solvent. Coarse-graining of surfactant, salt, and water helps reduce the number of particles by approximately 4 times and increase the time step in MD by an order of magnitude since time scales on the order of atomic bond vibrations are neglected in the CG description. MARTINI-based CG force fields⁷² used here have been extensively validated against atomistic simulations in terms of the radial distribution functions of

the system constituents. Polarizable CG water was used as a solvent because of its ability to capture electrostatic interactions in systems with charged interfaces more accurately compared to CG water models that lack a local dipole⁷³. The integrity of the cylindrical structure of the micelle is maintained by the surface adsorption of NaSal ions onto the micelle-water interface, especially when the molar ratio of NaSal to CTAC, $R \geq 1$. Hence in the simulations we used $R = 1.5$. The Weissenberg number $Wi \equiv S\tau_R$ is used to characterize the flow strength. Simulations are conducted for $0 \leq Wi \leq 125$. The vector \mathbf{l}_{axis} that connects the centers of mass of the two endcaps of the micelle represents the micelle axis. The angle θ that the projection of \mathbf{l}_{axis} onto the flow (x)-gradient (y) plane subtends with the x-direction is used to quantify orientation and flow-alignment. Micelle structure is not subject to any external constraints and is governed only by hydrodynamic forces as well as the interactions among the CTAC surfactants, NaSal salt and water molecules.

2.2. Simulation Methods

2.2.1. The CGMD Surfactant Model

Figure 2.1 illustrates atomistic and CG representations of the CTAB and NaSal molecules. Specifically, the tail group of the surfactant, which consists of 16 carbon atoms, is modeled using 4 CG beads and the positively charged head group with one CG bead. These models have been extensively validated and have shown to reproduce sphere-to-rod transitions and coalescence of micellar structures^{19, 44}.

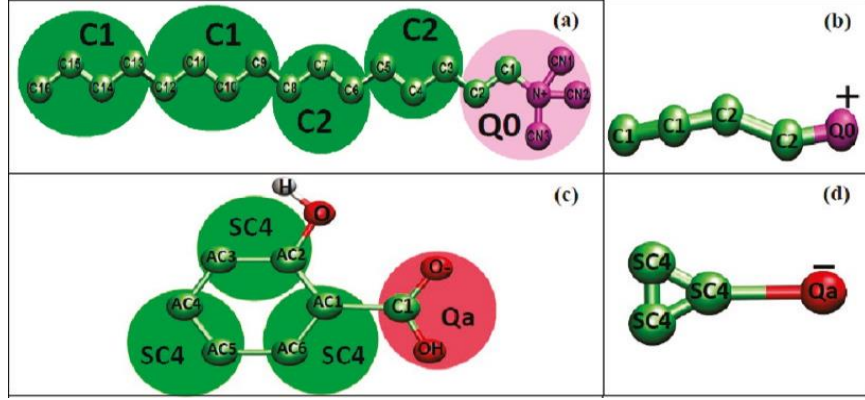


Figure 2.3: AA and CG representation of (a,b) cationic CTA⁺ surfactant and (c,d) hydrotropic Sal⁻ salt respectively.

Bonded interactions such as bond stretching and bending were represented by weak harmonic potentials V_b and V_θ respectively:

$$V_b(b) = \frac{1}{2}K_b(b - b_0)^2 \quad (2-1)$$

$$V_\theta(\theta) = \frac{1}{2}K_\theta(\cos(\theta) - \cos(\theta_0))^2 \quad (2-2)$$

where b_0 and θ_0 are the bond length and bond angle at the minimum energy configuration, respectively, and K_b and K_θ are constants associated with bond stretching and bending energies respectively. All non-bonded intramolecular interactions among the surfactant and salt beads as well as intermolecular interactions between surfactant, salt and solvent beads are represented by a Lennard-Jones (LJ) 12-6 potential. The LJ potential V_{LJ} between beads i and j separated by a distance r_{ij} is given by:

$$V_{LJ}(r_{ij}) = 4\varepsilon_{ij} \left[\left(\frac{\sigma_{ij}}{r_{ij}} \right)^{12} - \left(\frac{\sigma_{ij}}{r_{ij}} \right)^6 \right] \quad (2-3)$$

where ε_{ij} is the minimum in V_{LJ} and σ_{ij} is the distance at which the V_{LJ} vanishes. The values of these parameters are adopted from the work of Sangwai et al.¹⁹

Table 2.1: Bonded and non-bonded interaction parameters for all CG beads in the system

Interaction Potentials		
LJ	σ (nm)	ε (kJ/mol)
C1 – C1	0.47	3.5
C1 – C2	0.47	3.5
C1 – Q0	0.62	2.0
C1 – Qa	0.62	2.0
C1 – SC4	0.47	3.1
C2 – C2	0.47	3.5
C2 – Q0	0.62	2.0
C2 – Qa	0.62	2.0
C2 – SC4	0.47	3.1
Q0 – Q0	0.47	3.5
Q0 – Qa	0.47	4.5
Q0 – SC4	0.47	2.7

Qa – Qa	0.47	5.0
Qa – SC4	0.47	2.7
SC4 – SC4	0.43	2.625
Bond	d (nm)	K_b (kJ/mol/nm²)
C1 – C1	0.47	1250
C1 – C2	0.47	1250
C2 – Q0	0.47	1250
SC4 – SC4	0.27	1250
SC4 – Qa	0.47	1250
Angle	θ (degree)	K_θ (kJ/mol/rad²)
C1 – C1 – C2	180	25
C1 – C2 – C2	180	25
C2 – C2 – Q0	180	25

2.2.2. Assembling and Equilibrating a Rodlike Micelle

A short cylindrical micelle was obtained from a previous study where two spherical micelles were demonstrated to coalesce into a single stable cylindrical micelle driven by NaSal. The resultant cylindrical micelle structure containing 162 CTA⁺ monomers was solvated in 23364 polarizable CG water beads, equivalent to ~94000 all-atom water molecules, in a cubic box. Molar equivalent of Sal⁻ counterions were added. Na⁺ and Cl⁻ were placed at energetically favorable positions by replacing solvent molecules. This system was energy minimized and an equilibrium

MD run of 50 ns was performed at 300 K and 1 atm in an isothermal-isobaric (NPT) ensemble for the system to reach equilibrium density and energy. The resultant box size was 14.2 nm. Figure 2.2 shows a schematic of the NEMD simulation box and the angles used to characterize flow behavior.

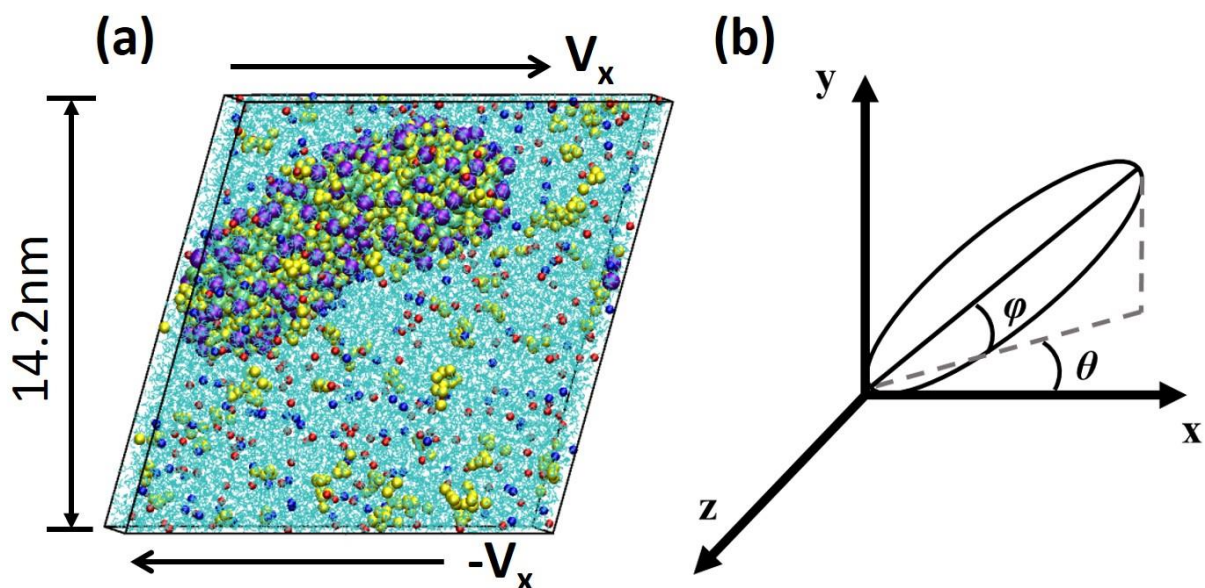


Figure 2.2: (a) Schematic of NEMD simulations. CTA⁺ surfactants (purple heads and green tails) groups, Salt ions (yellow), sodium (red) and chloride (blue) ions and water (cyan), (b) Schematic of the micelle axis and definitions of angles used to characterize flow-alignment.

2.2.3. Molecular Dynamics Simulations of Micelle Dynamics under Shear Flow

The equilibrated system was subjected to flow shear in NEMD simulations using Lees-Edwards boundary conditions⁷⁴ in which the top x-z plane is moving with a x-directional velocity $+V_x$, while the bottom the x-z plane is moving with a velocity $-V_x$ with a linear gradient in the

velocity along the y-direction (Fig. 2.2). The corresponding shear rate is $(2V_x/L)$ where L is the side of the cubic box. Pressure scaling was turned-off for NEMD. The time-step was 25 fs. Snapshots were saved after every 12.5 ps. Temperature scaling was implemented with improved Berendsen thermostat to maintain 300 K with a time constant of 0.5 ps. The relative permittivity was set to 2.5, as recommended for the polarizable CG water model in MARTINI potentials. Lennard-Jones non-bonded interactions were shifted to zero gradually in the range of $r_{\text{shift}} = 0.9$ nm to $r_{\text{cut}} = 1.2$ nm. Cut-off for Coulombic interactions $r_{\text{cut}} = 1.2$ nm. It was gradually shifted to zero from $r_{\text{shift}} = 0.0$ nm. Periodic boundary conditions were applied with the minimum image convention.

2.2.4. Determination of Micelle Relaxation from Flow-induced Stretched Configurations

In order to understand the dependence of pair potential energy on micelle length, we carried out equilibrium MD simulations on flow-stretched micelles to allow relaxation to their equilibrium lengths. A total of 10 different initial states with stretched micelles were obtained from NEMD simulations and were subjected to equilibrium MD simulations in an NVT ensemble without changing any other process conditions. These 10 simulations were carried out to estimate the dependence of two properties of the micelle: length relaxation and pair potential energy of the [Micelle-SaI] as functions of time. Each simulation was run for 50 ns which was sufficiently large considering observations of length and internal energy plateaued within first 10 ns.

2.2.5. Calculation of the Instantaneous Length and Orientation of the Micelle

To measure the alignment of micelle with flow in the x-direction, we first determine the center of mass of the end caps of the micelle in a given snapshot so that the axis of the micelle can be defined as the connecting vector between the end caps. Surfactant monomers participating in the end caps are distinguished by a distance parameter d_{cap} ($= 3.5$ nm). A monomer with its head group farther than $d_{\text{cap}} = 3.5$ nm from the center of mass of the micelle is part of an end cap. Further, we differentiate between the two end caps using relative distances of monomer head groups from each other. The vector \mathbf{l}_{axis} connecting the geometric centers of the two different end caps is defined as the axis of the cylindrical micelle. The flow is in the x-direction and gradient is in the y-direction, therefore the tumbling and flow-alignment are revealed clearly in the x-y plane. We project \mathbf{l}_{axis} onto the x-y plane to obtain $\text{proj}(\mathbf{l}_{\text{axis}})$. Thus the angle between $\text{proj}(\mathbf{l}_{\text{axis}})$ and the x-axis (θ) provides an accurate measure of flow-alignment effects independent of perturbations in the z-direction. In addition, the magnitude of \mathbf{l}_{axis} serves as a measure of micelle length.

2.3. Results and Discussion

2.3.1. Orientational Dynamics in Shear flow

Similar to polymer molecules, micelles tend to flow-align, stretch and tumble under shear flow. Flow-aligned micelles undergo an end-over-end tumbling due to the vorticity component in the rate of deformation tensor, which results in fluctuations in micelle length and orientational angle, θ . Fig. 2.3 shows θ plotted as a function of time t for 6 different values of Wi . Note that $\theta = 0^\circ$ represents a fully flow-aligned state while a transition through 90° corresponds to a tumbling event. Results are shown only for the first $1 \mu\text{s}$ for clarity although the trends remain the same throughout the duration of the simulations ($> 3 \mu\text{s}$). It is evident that in the absence of flow, i.e., for $Wi = 0$, the intrinsic rotational diffusion of the micelle dominates the orientational distribution.

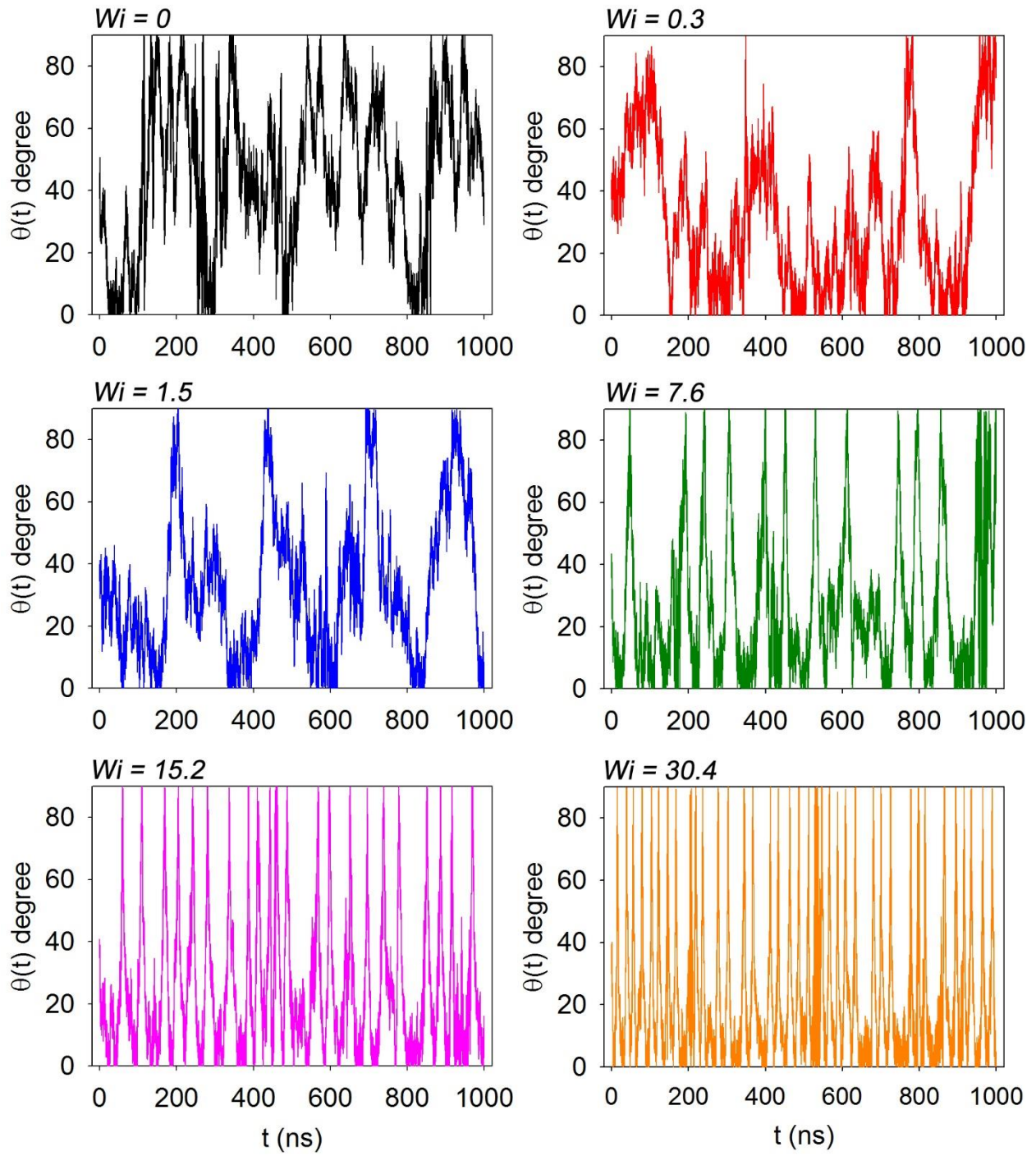


Figure 2.3: Plots of θ vs. time t for various Wi .

Beyond $Wi \sim 1$, flow becomes sufficiently strong enough to influence micelle dynamics. This can be seen by a more regular behavior in the variation of θ with time. Further, a consistent increase in the number of peaks as a function of time suggests that, with increase in Wi , the time taken by the micelle to go through one tumbling event reduces. In other words, this would imply that the micelle has an increased preference to a flow-aligned state. This is clearly seen in Fig. 2.4 where the probability distribution function (PDF) $p(\theta)$ is plotted. The pdf is uniform for $Wi = 0$ suggesting the absence of any preferred orientation.

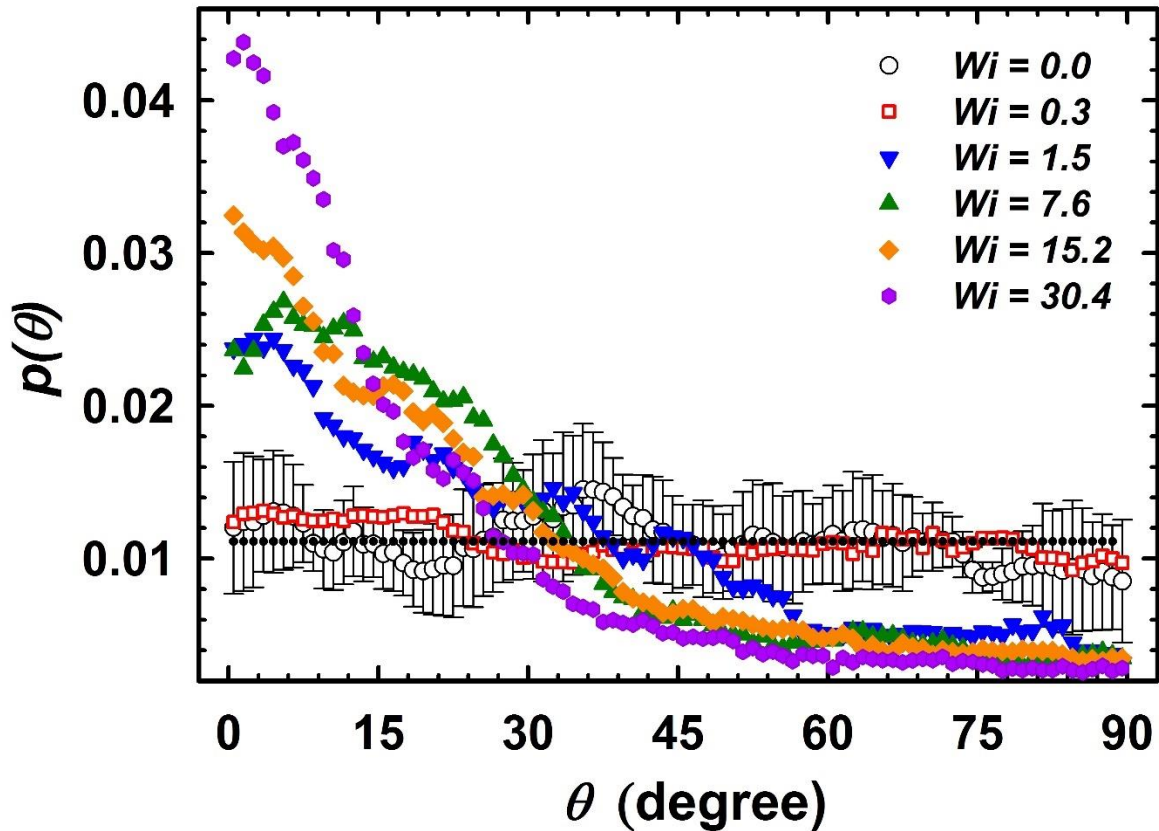


Figure 2.4: $p(\theta)$ at various Wi . The dotted line represents a uniform distribution and the vertical bars show the standard deviation of $p(\theta)$ at $Wi = 0$ in the simulations within each interval.

As Wi is increased, the effect of flow on micelle orientation becomes progressively more prominent. For example, for $Wi = 0.3$ the departure of $p(\theta)$ from the uniform equilibrium distribution is relatively small suggesting that the rotational diffusion dominates over flow alignment. However, at $Wi = 1.5$, higher probabilities are clearly seen associated with flow-aligned states. A crossover from a diffusive to a flow-aligned regime occurs at $Wi \sim 1$. For $Wi > 1$, quasi-periodic tumbling events dominate the micelle dynamics. Snapshots (i) and (ii) of the micelle displayed in Fig. 2.6 correspond to $\theta = 0^\circ$ (flow-aligned state) and $\theta = 90^\circ$ (gradient-aligned state) respectively at $Wi = 7.6$. The tumbling events occur at regular intervals while the tumbling frequency increases with Wi . For $Wi > 1$, $p(\theta)$ follows a Gaussian distribution and the full width at half maximum of the orientational distribution ($\Delta\theta$) $\propto Wi^{-0.31}$, which is consistent with previous predictions of mesoscopic theories for semiflexible polymers^{56, 62, 63} (Fig. 2.5).

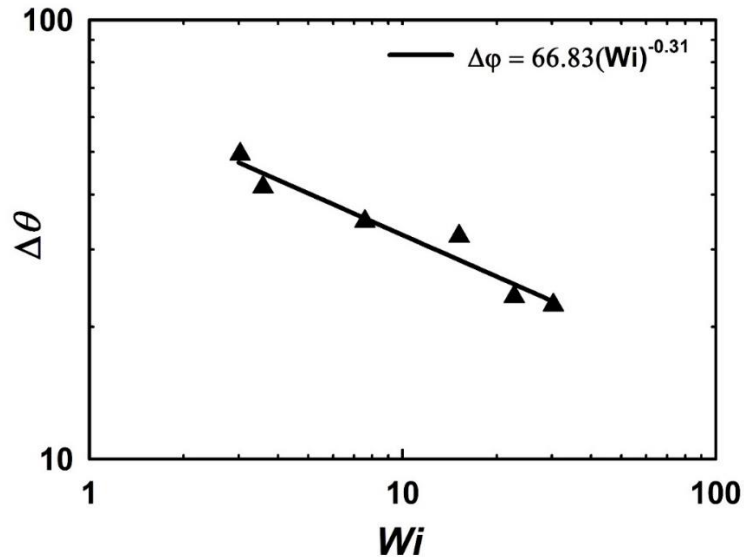


Figure 2.5: $\Delta\theta$ as a function of Wi . The solid line is a power law fit with an exponent of -0.31 which is in close agreement with experimental and theoretical predictions of -1/3.

Shape fluctuations in the z-dimension also influence the tumbling cycles, as seen in snapshot (iii) in Fig. 2.6, in which the micelle is slightly bent and misaligned with respect to the flow direction. In this case, the micelle axis is out of the flow-gradient plane, as seen in snapshot (iv). Such events occur more frequently for relatively low shear rates and tend to randomize the tumbling cycles. The micelle eventually recovers from such misaligned states to flow-aligned ones before undergoing a tumbling event or transitioning to another misaligned state.

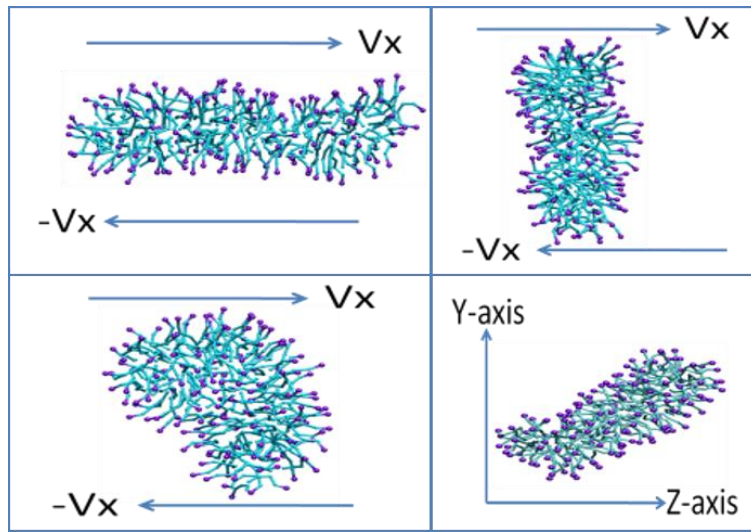


Figure 2.6: (Top left) Flow-aligned, (Top right) gradient-aligned, (Bottom left) misaligned (in the xy plane), and (Bottom right) misaligned (in the yz plane) states (not to scale).

The angular distributions of rod-like micelles can be defined in two ways. The first one is the angle between the micelle axis ($\text{proj}(\mathbf{l}_{\text{axis}})$) and the flow direction (x), θ , which is discussed above and the second one is the angle between the micelle axis ($\text{proj}(\mathbf{l}_{\text{axis}})$) and the out-of-plane direction, φ , which in this case is the z-axis. It has been shown that for rodlike and semiflexible polymers, the PDF of the angle φ , $p(\varphi)$, decays as φ^{-2} for $Wi \gg 1$ and always approaches a value

of $\pi/2$ independent of the Wi . Fig. 2.7 contains a plot of $p(\varphi)$ with the respect to φ . The black line indicates a slope of -2 and it is clear that for $Wi \gg 1$ the orientational dynamics of rodlike micelles are extremely similar to that of rigid and semiflexible polymers.

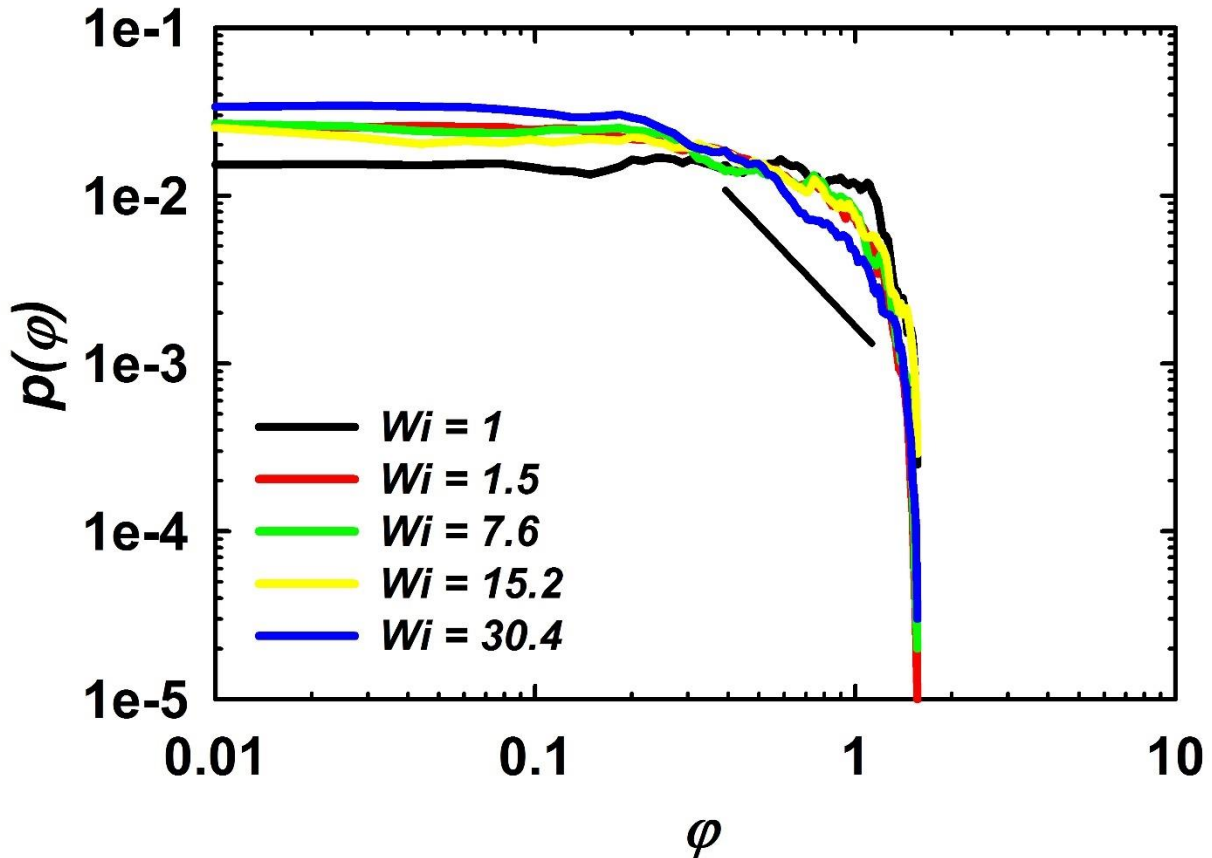


Figure 2.7: $p(\varphi)$ at various Wi for $Wi > 1$. The black line indicates a slope of -2.

The autocorrelation function (ACF) of θ defines the temporal correlation of the angular orientation. The ACF at $Wi = 0$ (at equilibrium) can be used to define an orientational relaxation time τ_R of θ by fitting it to a decaying exponential of the form,

$$ACF = \exp(-t/\tau_R) \quad (2-4)$$

where the ACF has been normalized using its value at $t = 0$. The relaxation time τ_R was calculated to be 28.7 ns and was used in our calculations of Wi .

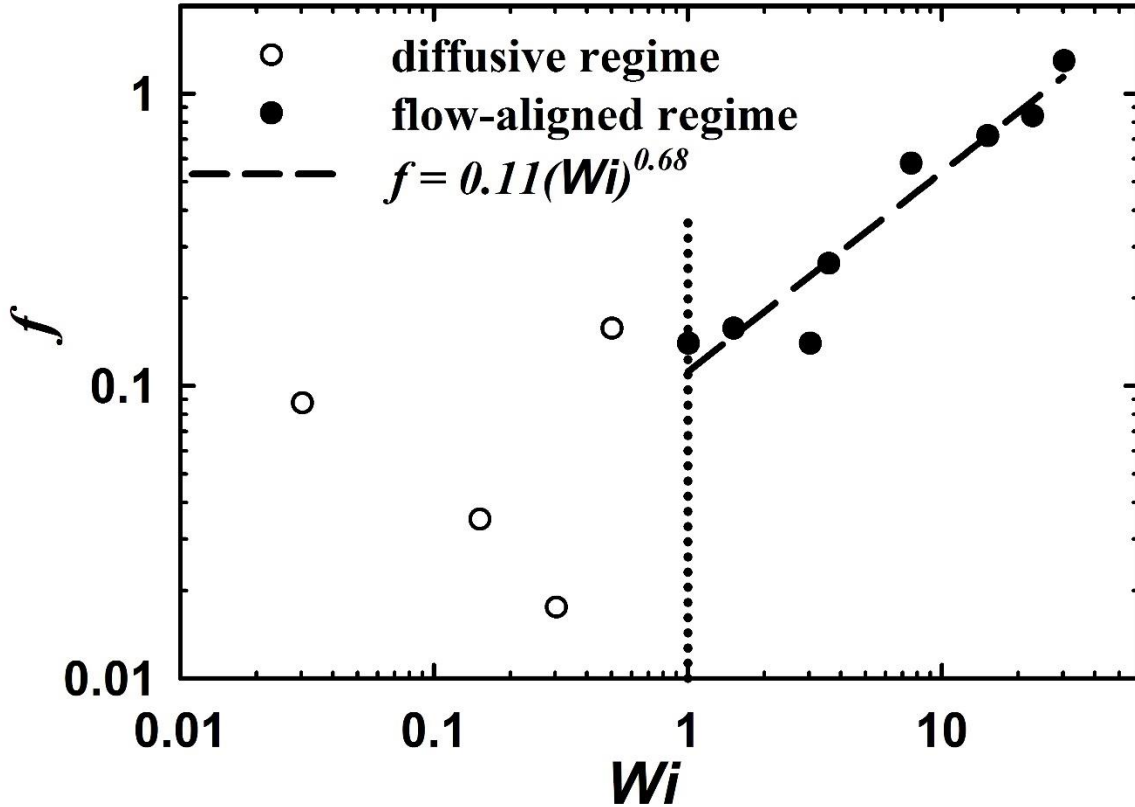


Figure 2.8: Normalized tumbling frequency f versus Wi . Open circles indicate stochastic diffusion regime while filled circles lie in the flow-aligned regime. Power law fitting in the flow-aligned regime yields $f \sim Wi^{0.68}$.

The power spectral density (PSD) can be obtained from the fast Fourier transform (FFT) of the ACF. We obtain the tumbling frequency $f^* \equiv (1 / \tau_c)$ from the peak in the PSD⁵⁸. The normalized tumbling frequency $f \equiv 1/(\tau_c/\tau_R)$ is plotted as a function of Wi is shown in Fig. 2.8. For

$Wi < 1$, no systematic change in f is observed. However, for $Wi > 1$, f increases indicating more frequent and periodic tumbling. Power law fitting of f vs. Wi provides an exponent of 0.68 which is also observed in Brownian dynamics simulations of polymers in dilute solutions^{75, 76, 77, 78}.

The rotational diffusivity D was obtained from equilibrium simulations as one sixth of the slope of the linear fit of the mean squared angular displacement, $\langle \theta - \theta_0 \rangle^2$, vs. time (Fig. 2.9). This yielded $D = 6 \times 10^6 \text{ rad}^2\text{s}^{-1}$, corresponding to $\tau_D = 6.58 \mu\text{s}^2$.

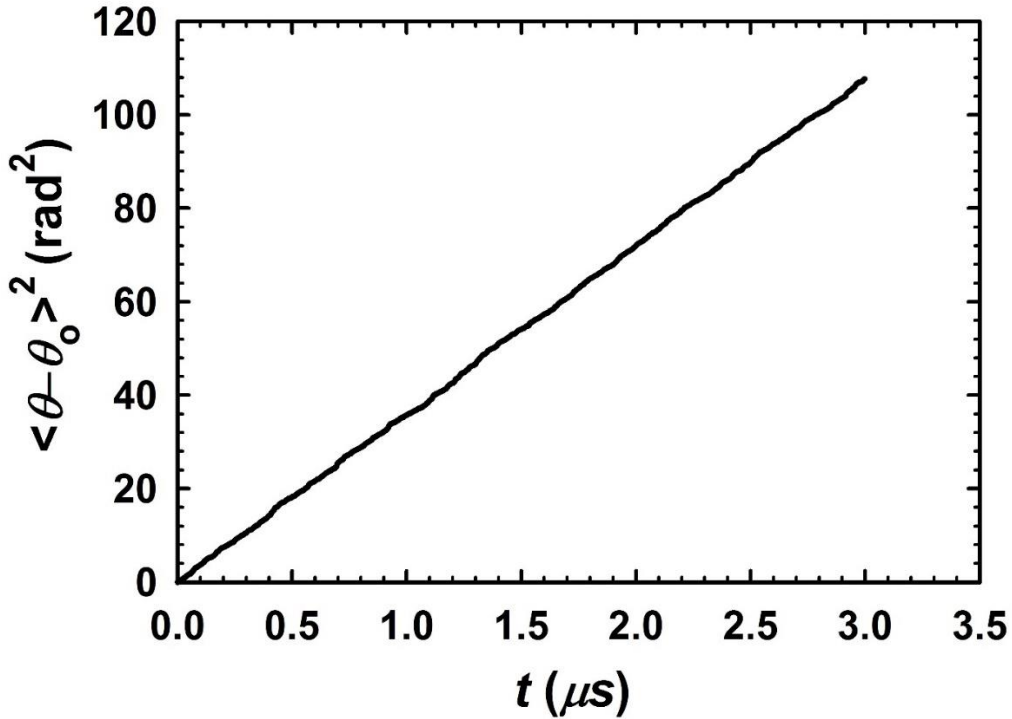


Figure 2.9: Mean squared angular deviation vs. time for $Wi = 0$.

For comparison purposes, if we consider the micelle to be a rigid rod with length $L = 10$ nm and aspect ratio $a = 2.5$ (based on a micelle diameter of ~ 4 nm), in a dilute aqueous solution at 300K with viscosity η of 0.001 Pa.s, the estimated $D = 3k_B T \ln(a) / (\pi \eta L^3)$, yields $\tau_D \sim 10^{-5}$ s. This

is in qualitative agreement with the value of D calculated from our simulations. The orientational relaxation time τ_R , however, is the time scale over which temporal correlations in the orientational angle θ is lost. This is on the order of 10 ns and comparable to the time scale of tumbling events. Transition from the diffusive to flow-aligned regime occurs when $\tau_R \sim 1/S$, or equivalently when $Wi \approx 1$ ($Pe \approx 230$).

2.3.2. Structure Relaxation and Stretching Forces

We computed the change in the total pair potential energy $\Phi(l)$ of the surfactants in the micelle and adsorbed Salt ions as a function of length l of the micelle, defined as the magnitude of the vector \mathbf{l}_{axis} . Note that l therefore is smaller than the end-to-end distance of the micelle. The use of \mathbf{l}_{axis} to calculate l instead of using the end-to-end micelle vector has an advantage of reducing the statistical uncertainty in l arising from shape fluctuations. We carried out 10 different equilibrium MD simulations of previously sheared systems where flow-aligned stretched micelles were allowed to relax to their equilibrium length structures. Over the length relaxation spectrum of the micelle from about $l = 7.2$ to 4.7 nm, $\Phi^*(l) \equiv \langle \Phi(l) - \Phi(l, Wi=0) \rangle$ was averaged into equally spaced bins of l with a width $dl = 0.0122$ nm (Fig. 2.10). The relaxation of length happens over a period of roughly 8 ns and therefore only the first 8 ns of data was considered. Energy $\Phi^*(l)$ needed to stretch a micelle from its equilibrium length is observed to vary linearly with l (Fig. 2.10). The slope of the linear fit provides a constant stretching force of $\approx 650 \text{ kJmol}^{-1} \text{ nm}^{-1}$ which corresponds to ~ 1 nN per molecule. In comparison, the force required to stretch a covalent bond is 2-3 orders of magnitude greater⁷⁹, while that for hydrogen bond stretching in water is 1-2 orders of magnitude greater⁸⁰. This is reasonable considering that the micelle is self-assembled by weak non-bonded

forces. Our estimate is in very good agreement with experimental measurements of similar forces in biological systems⁸¹.

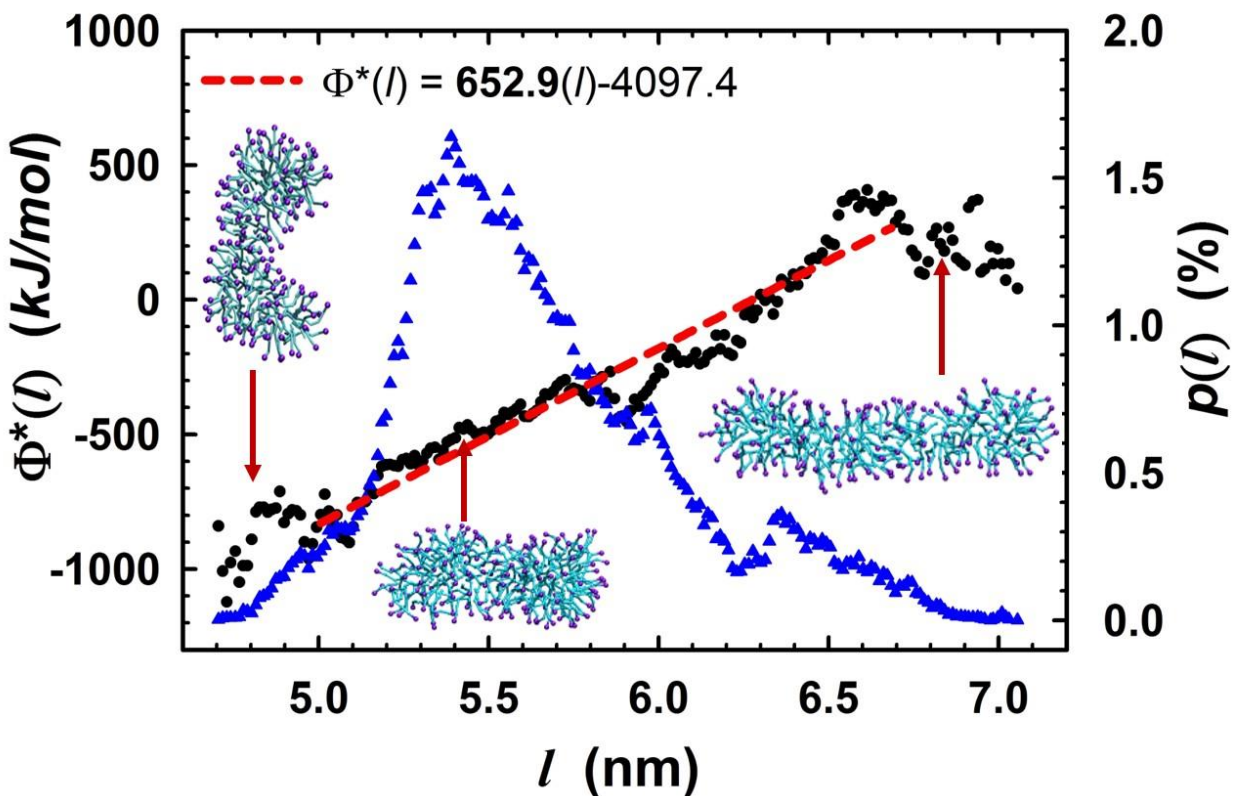


Figure 2.10: Pair potential energy $\Phi^*(l)$ (black dots) and probability distribution of length $p(l)$ (blue triangles) from the length relaxation simulations are plotted as a function of l . Snapshots at different locations show a) stretched micelle ($l \approx 7$ nm), b) micelle with most probable length $l \approx 5.4$ nm, and c) bent micelle ($l \approx 4.7$ nm).

The linear relationship between $\Phi^*(l)$ vs. l may be interpreted as an asymptotic behavior valid for a relatively short (\sim nm), stiff rodlike molecular assembly. From a further coarse grained, mesoscopic modeling point of view, this would suggest that a micelle with length on the order of

a few nanometers may be considered as a stiff spring whose length may only fluctuate within a small range around an average value, e.g. as in the stiff FENE-Fraenkel spring proposed by Hsieh et al. to model practically inextensible rods in the freely jointed bead-rod chain model of polymer chains⁸². In order to verify this, we calculated the probability distribution of l from a total of 160,000 configurations. A probability distribution of l during the relaxation process is also plotted in Fig. 2.10. The distribution shows a pronounced peak at 5.4 nm which is the most probable length. The micelle appears to explore lengths smaller than $l = 5.4$ nm which is possible because of a mechanism in which the recoil from a stretched state to equilibrium length would cause either micelle bending or compression. Further, the linear fit is not extended to the two ends of the length spectrum because the sampling of $l < 5.0$ nm and $l > 6.7$ nm in our simulations is very poor. However, we believe that the dependence of micelle pair-potential energy on micelle length will still hold true for all cases. In the three different micelle states shown in the plot, a stretched micelle ($l \approx 7.0$ nm) can be seen to relax to a shorter state with $l \approx 5.4$ nm and then further recoil into a state bent along its axis ($l < 5.0$ nm).

2.3.3. Flow-induced Micelle Scission

Unlike polymer chains, in which the monomers are covalently bonded to each other, micelles are self-assembled by weak non-bonded interactions. This presents a limitation in the range of Wi that can be explored without causing micelle scission. We performed multiple simulations between $50 \leq Wi \leq 125$ to study micelle scission. It was observed that micelle scission does not occur for $Wi < 70$. For larger Wi , flow shear is sufficiently strong to cause micelle breakage as shown in Fig. 2.11, in which the micelle is seen to undergo a few tumbling events before scission.

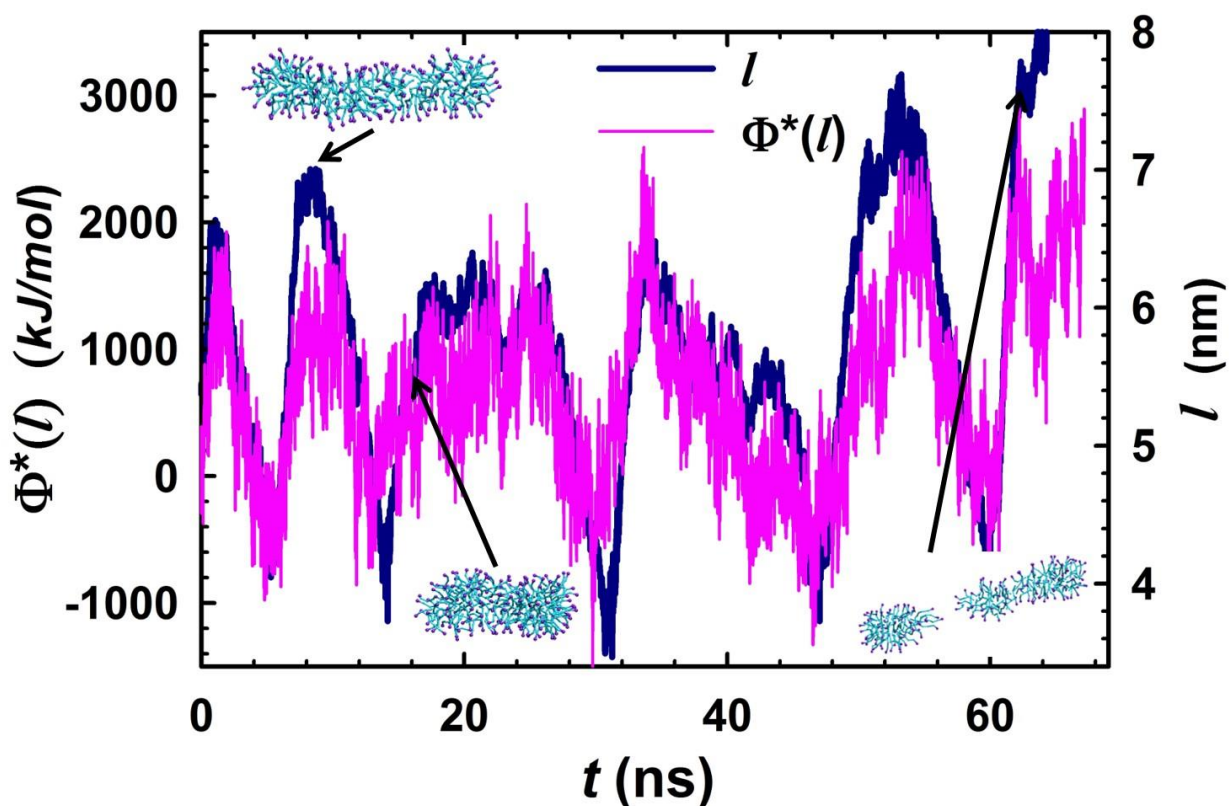


Figure 2.11: $\Phi^*(l)$ and l versus t showing micelle scission for $Wi = 76$. Snapshots at different locations show a) stretched micelle ($t \approx 8$ ns), b) micelle with most probable l ($t \approx 16$ ns) and c) micelle after scission ($t \approx 62$ ns).

A plot of $\Phi^*(l)$ as a function of time is shown in Fig. 2.12 for a case where no breakage was observed ($Wi = 50$) and for three cases for which the micelle broke apart into two shorter ones ($Wi = 76, 100, 125$). This plot, as well as data from other simulations, suggest the existence of an energy threshold for scission. From a series of simulations, the threshold value was estimated to be ~ 2500 - 2700 kJmol^{-1} . The observed extension before breakage, compared to the equilibrium

configuration, is 2-3 nm. This, based on the stretching force estimated above, corresponds to an increase in $\Phi^*(l)$ of 1300-1950 kJmol⁻¹, which is comparable to the estimated threshold. As the micelle stretches, the distance between the CTA⁺ head group and adsorbed Sal⁻ ions increases thereby reducing electrostatic screening and increasing the overall micelle energy. Above the threshold, it is energetically favorable to have two smaller micelles. This is further evidenced by the fact that the magnitudes of $\Phi^*(l)$ and $\Phi_{EL}^*(l)$, which is the electrostatic component of the pair potential energy between CTA⁺ and Sal⁻, are approximately equal. The other components of $\Phi^*(l)$ remain practically unchanged.

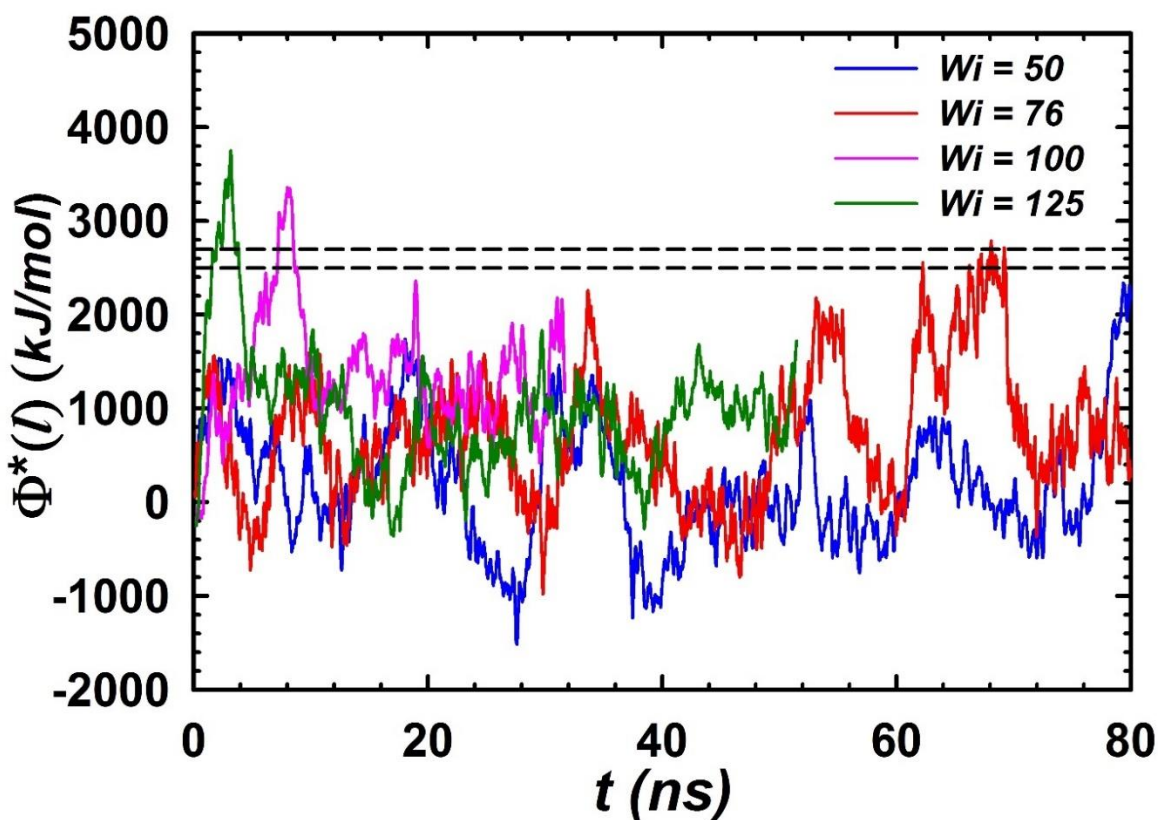


Figure 2.12: $\Phi^*(l)$ vs. t for 4 different Wi as indicated. Dotted lines indicate the range for micelle scission for $Wi > 70$.

2.4. Conclusions

In summary, we have provided a quantitative description of the shear-induced orientation dynamics, stretching and scission of rodlike surfactant micelles using coarse-grained molecular dynamics (CG MD) simulations. Our simulations accounted for hydrodynamic interactions and solvent polarity by using a 3-site polarizable CG water model and long-ranged electrostatic interactions using the particle mesh Ewald (PME) summation. Equilibrium simulations were performed to obtain quantities such as the orientational relaxation time, rotational diffusivity and average micelle length. Non-equilibrium molecular dynamics (NEMD) simulations were utilized to study the dynamics of a single rodlike micelle. The Weissenberg number (Wi), defined as the ratio of the micelle angular relaxation time to the inverse shear rate, was found to be an appropriate parameter that demarcates the diffusive and flow aligned regimes. Micelle tumbling frequency has been found to follow a power law relation with Wi , with an exponent of 0.68, which is in great agreement with experimental and theoretical estimates for rigid, semiflexible polymers. We have also analyzed the orientation distribution of the end-to-end vector, which is characterized by the orientation angle θ , defined as the angle between the projection of the end-to-end vector onto the flow-gradient plane and the flow direction. The mean orientation angle has been discovered to be slightly biased to positive θ values and the probability distribution function (*PDF*) of θ could be approximated by a shifted Gaussian for $Wi > 1$. Full width at half maximum (FWHM) of PDF of θ follows a power law relation with Wi , and the coefficient approaches to $-1/3$, which is again in good agreement with stochastic simulations and mesoscopic theories. Our results suggest that from a mesoscopic point of view, short rodlike micelles may be represented by a stiff bead-spring unit subject to hydrodynamic drag, Brownian fluctuations and a constant entropic spring force. Energy-

extension relationship in rodlike micelles was found to be linear with a constant stretching force of ~ 1 nN per molecule. This is the first time such forces have been measured for micellar systems. Comparisons can be made to the estimates of van der Waals forces in Gecko feet which have been calculated using atomic force microscopy (AFM) techniques and found to be in the same range. Micelle scission happens through a mechanism in which shear-induced stretching causes the surfactant head groups and adsorbed counterions to be farther apart, resulting in reduced electrostatic screening and an increase in the overall micelle energy. The energy barrier for micelle scission was found to be independent of Wi . Thus, consistent with experiments, for $Wi \sim O(1)$ flow-alignment of micelles would promote SIS formation leading to shear thickening while for $Wi \gg 1$ flow-induced micelle scission would result in shear thinning. The CGMD methodology used here can be extended to solutions that contain multiple micelles and/or nanoparticles to study emerging morphologies, flow-structure interactions and rheological properties to benefit applications ranging from enhanced oil recovery and hydrofracking⁸³ to design of active nanofluids for energy harvesting and sensing²⁷.

Chapter 3

Self-assembly of nanoparticles with surfactant micelles

[Adapted (in part) from *Langmuir* **32**, 5 (2016)]

3.1. Introduction

Nanoparticles (NPs) are often functionalized to suit a wide range of applications such as targeted drug delivery⁸⁴, biosensing⁸⁵, imaging⁸⁶, catalysis⁸⁷, and enhanced light trapping in photovoltaics⁸⁸. NPs can be functionalized by using polymers^{89, 90, 91}, DNA^{92, 93}, surfactants⁹⁴, biomolecules⁹⁵ and other natural and synthetic ligands. These functional groups can prevent particle aggregation, enhance NP suspension stability and help create diverse NP morphologies and ordered networks^{46, 96}. Selection of the type of functional group is based on the NP size, shape and surface properties such as electric charge and hydrophobicity⁹⁷. Functionalization can also alter the toxicity of the NPs and/or ligands⁹⁸. For instance, cetyltrimethylammonium bromide (CTAB)-functionalized gold NPs are extremely stable and do not exhibit cytotoxicity whereas unbound CTAB molecules show significant levels of toxicity⁹⁹.

As discussed in Chapter 1, the primary mechanism of these interactions is through surfactant adsorption at the solution-solid interface. The adsorption of CTAB, has been studied extensively on planar surfaces of both hydrophilic and hydrophobic character. For hydrophobic surfaces, CTAB surfactants typically adsorb in a tail-on configuration, resulting in hemi-admicelles with morphology that depends on the specific surface chemistry. For example, the adsorption of CTAB onto graphite results in well-ordered hemi-cylindrical admicelles, whereas the adsorption of CTAB on mica results in a wide range of ad micellar structures, including

hemispheres¹⁰⁰, hemi-cylinders¹⁰¹, and surface network structures. In contrast, CTAB molecules have been shown to form much different structures on hydrophilic surfaces. For example, CTAB admicelles typically adopt a spherical morphology on quartz surfaces, whereas they primarily exhibit a bilayer morphology on amorphous silica as well as a number of other hydrophilic surfaces including other mineral oxides and metals. The morphology of CTABs on hydrophilic surfaces can vary widely with surface preparation¹⁰². Experiments have shown that CTAB surfactants tend to form a bilayer structure around a metallic NP with the head groups of the surfactants bound to the surface of the NP¹⁰³. The nanoparticle surface geometry may also play a role in determining the nature of the self-assembly. Further, in the case of spherical nanoparticles, the role of nanoscale surface curvature on the self-assembly phenomena is also not well understood.

Surfactant-covered NPs are also known to self-assemble with wormlike micelles (WLMs) to produce stable nanofluids. Such fluids tend to be viscoelastic and, depending on the properties of the NPs, they can be tuned to respond to external stimulus such as an optical or magnetic field. For instance, Nettekoven et al.¹⁰⁴ observed that the introduction of NPs into a cationic WLM solution increased the zero shear viscosity, longest relaxation time and storage modulus of the solution. Small angle x-ray and neutron scattering studies suggest that such changes in fluid rheology can be attributed to the bridging of the micelle end-caps with NPs to form stable “junctions”^{27, 104}. Self-assembly of noble metal NPs with WLMs has been shown to offer a robust route for producing stable multicomponent nanogels that respond to localized or broadband electromagnetic excitation²⁴. The optical properties of such plasmonic gels can be easily tuned by varying the type, shape and/or concentration of the NPs. Further, they exhibit rich rheological behavior depending on the NP concentration and the salt to surfactant molar concentration ratio,

R. Specifically, non-monotonic dependence of zero shear viscosity on NP concentration, rheopexy, shear thickening, shear banding and shear thinning have been observed²⁴.

In this Chapter, we use coarse grained (CG) molecular dynamics (MD) simulations to explore the mechanisms underlying the self-assembly of NPs with CTAC surfactants as well as CTAC-functionalized NPs, referred to as nanoparticle surfactant complexes (NPSCs), with rodlike micelles of CTAC in presence of sodium salicylate (NaSal) salt. Both uncharged hydrophobic NPs and charged ones with negative zeta potentials that mimic noble metal particles are considered. Previous MD simulations of similar systems, although limited to time scales on the order of a few hundred picoseconds and performed on pre-assembled NPSCs, have shown that a bilayer assembly of cationic surfactants around semiconductor (ZnS) and metal (Ag) NPs is energetically favorable^{45, 105, 106}. In the present study, we perform CG MD simulations spanning time scales on the order of microseconds to investigate the self-assembly process. Our CG force fields for CTAC and NaSal are based on the MARTINI framework⁷² and have been shown to reproduce experimentally observed phenomena in surfactant solutions such as salt-induced sphere-to-rod shape transition as well as binary interactions and merger of spherical micelles. Further, similar CGMD simulations have been employed to unravel a rich variety of micelle structures as well as their topological, energetic and rheological features. Specifically, Dhakal et al.¹⁷ have performed CG MD simulations of CTAC/NaSal micelle solutions containing ~ 100 micelles and shown that such simulations are capable of accurately predicting micelle length distributions, persistence length, end-cap energies, shape transitions and branching. Further, the CG model employed in this work is capable of capturing experimentally observed anomalous viscosity variations with respect to salt concentration in CTAC/NaSal micelle solutions, and correlating such viscosity variations to changes in the underlying microstructure.

3.2. Simulation Methods

All simulations were implemented in the GROMACS molecular dynamics package¹⁰⁷ using a Coarse Grained (CG) representation described by the MARTINI force field.

Nanoparticle: All composite NPs are spherical and were obtained by cutting a sphere of desired size from the center of an icosahedral hexagonal close-packed (HCP) crystal structure, as done in previous studies of NP translocation across phospholipid bilayers^{108, 109}. The particle diameter (3.5 nm) is comparable to the length of a CTAC molecule. This particle was made up of 297 CG beads out of which 162 beads were on the surface. For hydrophobic NPs, all core and surface beads were kept nonpolar and neutral by assigning a C1 particle type (Fig. 3.1a). For metal NPs, the core beads were assigned a C1 particle type whereas the surface beads were assigned a Q0 particle type with a fractional negative charge on each bead (Fig. 3.1b). The interaction potentials between the bead types that describe the NPs and constituent particles can be found in Chapter 2 (Table 2.1).

Surfactant and Salt: The CG model for CTA⁺ surfactant and Sal⁻ salt were obtained from previous work done by Sangwai et al. A short rodlike micelle consisting of 162 surfactants, of aspect ratio ~ 3 , was obtained from the self-assembly of two spherical micelles in the presence of Sal⁻.

Water and Counterions: Standard single-site CG water was used as explicit solvent and Na⁺ and Cl⁻ counterions were added to maintain the electroneutrality of the system.

Two different sets of equilibrium MD simulations were performed for each NP type. The first set of simulations was performed to study the self-assembly of a single NP with free

surfactants in an aqueous solution resulting in the formation of an NP-surfactant complex (NPSC). The effects of surface charge and hydrophobicity of the NP on the structure of the NPSC was investigated. Subsequently, a second set of simulations was performed to study the self-assembly of NPSCs with rodlike micelles in presence of NaSal salt. Systems in the first set consist of a cubic box of dimensions $15 \times 15 \times 15 \text{ nm}^3$ containing 28,125 CG water molecules. One NP, 324 CTA⁺ as well as Na⁺ and Cl⁻ counterions, required to maintain electroneutrality, were added to the system by replacing overlapping water molecules. A table describing the composition of all of the systems studied is given in Table 3.1.

Table 3.1: Number of NPs, CTA⁺, Cl⁻, Na⁺ and Water (W) for different values of surface charge density (σ).

Surface Charge Density (σ)	Number of NPs	Number of CTA ⁺	Number of Cl ⁻	Number of Na ⁺	Number of W
0.0	1	324	324	0	19507
-0.33	1	324	324	55	19452
-0.66	1	324	324	107	19400
-1.0	1	324	324	162	19345
-1.5	1	324	324	243	19264
-2.0	1	324	324	324	19183

Hydrophobic NPs are uncharged whereas metal NPs are known to have a negative surface charge due to the presence of the free electron plasma. The negative charge on each surface bead, also referred to as the surface charge density (σ), of the NP was varied from 0 to $-2 e$ per bead where e denotes the elementary charge or charge carried by a proton. This range of σ corresponds to zeta potential values which are in good agreement with those reported experimentally for gold NPs^{110, 111}. The system was then energy minimized using the steepest descent algorithm followed by an MD simulation in an isothermal-isobaric ensemble for 5 ns with a time step of 10 fs at 300 K and 1 atm. The total simulation time for a system with uncharged, hydrophobic NPs was 250ns whereas a longer simulation time of 1 μ s was required for charged metal NP systems because the formation of a double layer occurs over a relatively longer time.

The second set of simulations was performed by adding the self-assembled NPSC and a rodlike micelle of 162 CTA⁺ in a 29 x 16 x16 nm³ box containing ~ 50,000 CG water molecules. Further, NaSal salt was added to the above system to facilitate coalescence of the two structures. It has been shown that for organic salts such as NaSal, there is sufficient screening of electrostatic repulsion between the head groups of surfactants for $R \geq 127$. Hence, we chose $R = 1$, i.e., equimolar concentrations of the surfactant and salt. Finally, electroneutrality was achieved by the addition of Na⁺ and Cl⁻ counterions and overlapping water molecules were removed. In all of the above simulations, roughly 10-12% of all water molecules were modeled with the antifreeze CG water provided in the MARTINI force field. This is essential because the standard MARTINI CG water model has a freezing point between 280 and 300 K. The system was then energy minimized by using the steepest descent method followed by an MD simulation in an NPT ensemble for 20 ns with a time-step of 10 fs at 300 K and 1 atm. Furthermore, a production run was performed for several hundred nanoseconds with trajectories saved after every 10 ps. Temperature and pressure

of the system were maintained constant using the velocity rescale method and the Parrinello-Rahman pressure coupling scheme, respectively. Periodic boundary conditions were applied in all three orthogonal directions. As recommended for the MARTINI force field, cut-off for non-bonded interactions was set to 1.2 nm. Specifically, Lennard-Jones interactions and electrostatic interactions were shifted smoothly to zero within the inter-particle distance range of 0.9-1.2 nm and 0.0-1.2 nm respectively. Long-range electrostatic interactions were evaluated using the Particle Mesh Ewald (PME) method. The implementation time for these simulations is extremely machine dependent, especially while including PME calculations. Majority of these simulations were performed on an in house cluster in which we could achieve around 18 ns/day with 16 2.40 GHz Intel Xeon E5620 processors for a system containing ~ 64000 CG beads with PME. However, some of these simulations were performed on the Blacklight supercomputer where we could achieve around 250 ns/day with 96 2.27 GHz Intel Xeon X7560 processors for the same system described above.

3.3. Results and Discussion

3.3.1. Self-Assembly of CTAC surfactants with NPs

Simulations of NPs with different surface properties yielded different NPSCs. NPs with a neutral, hydrophobic surface formed a corona-like monolayer structure made up of 156 CTA⁺ tail groups of the surfactants physically adsorbed onto the surface of the particle (Fig. 3.1c). In contrast, NPs with negative surface charge formed a double layered vesicle-like structure made up of 324 CTA⁺ surfactants with the cationic surfactant head groups electrostatically bound to the surface of the particle (Fig. 3.1d)¹¹². Figure 3.2 shows a closer look at the bilayer structure.

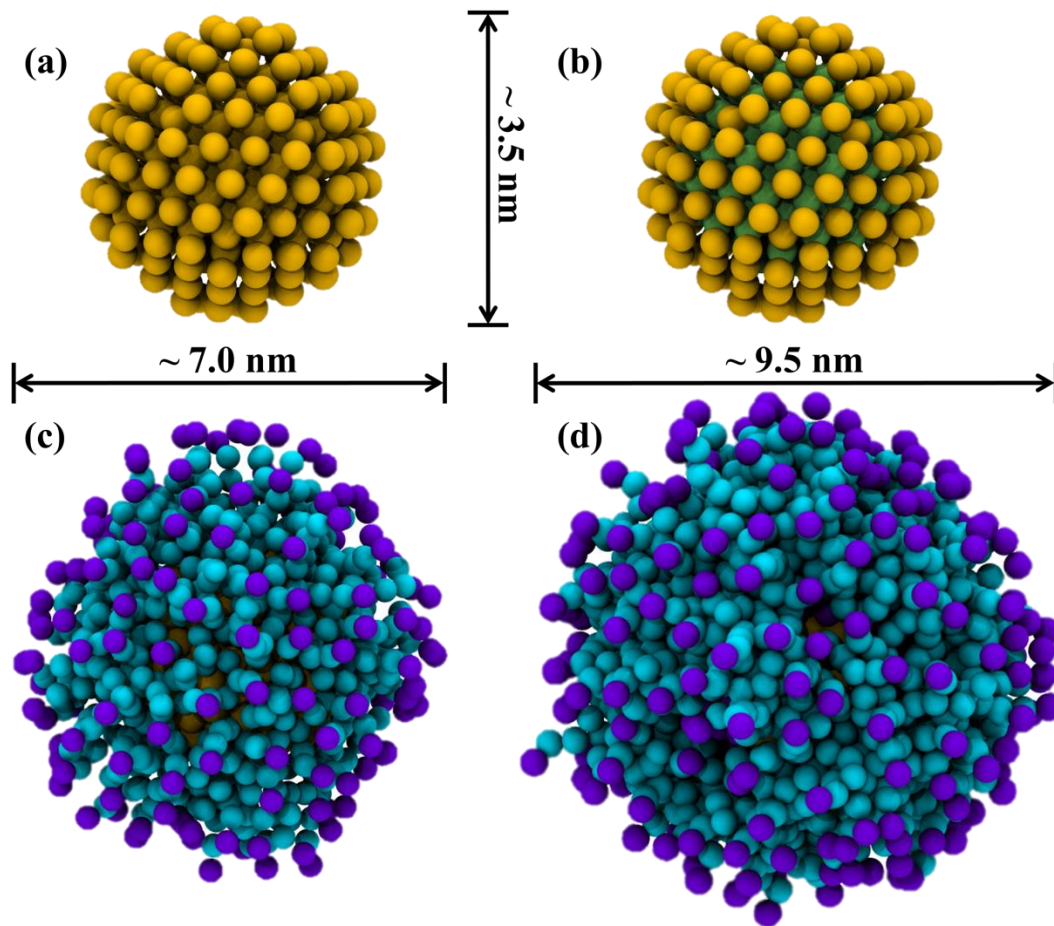


Figure 3.1: (a) Hydrophobic NP with an uncharged surface and core (C1 particle type) (yellow). (b) Metal NP with a charged CG surface (Q0 particle type) (yellow) and an uncharged core (C1 particle type) (green). (c, d) Snapshots of the self-assembled NPSCs. CG water, ions and excess surfactants are not shown for the sake of clarity. Color scheme: NPs (yellow), CTA⁺ head group (violet) and CTA⁺ tail groups (cyan). (c) Corona-like monolayer with the tail groups of CTA⁺ physically adsorbed on to the NP surface. (d) Vesicle-like bilayer with the head groups of the inner layer electrostatically attracted to the NP surface and the tail groups of the outer layer interlinked with the tail groups of the inner layer.

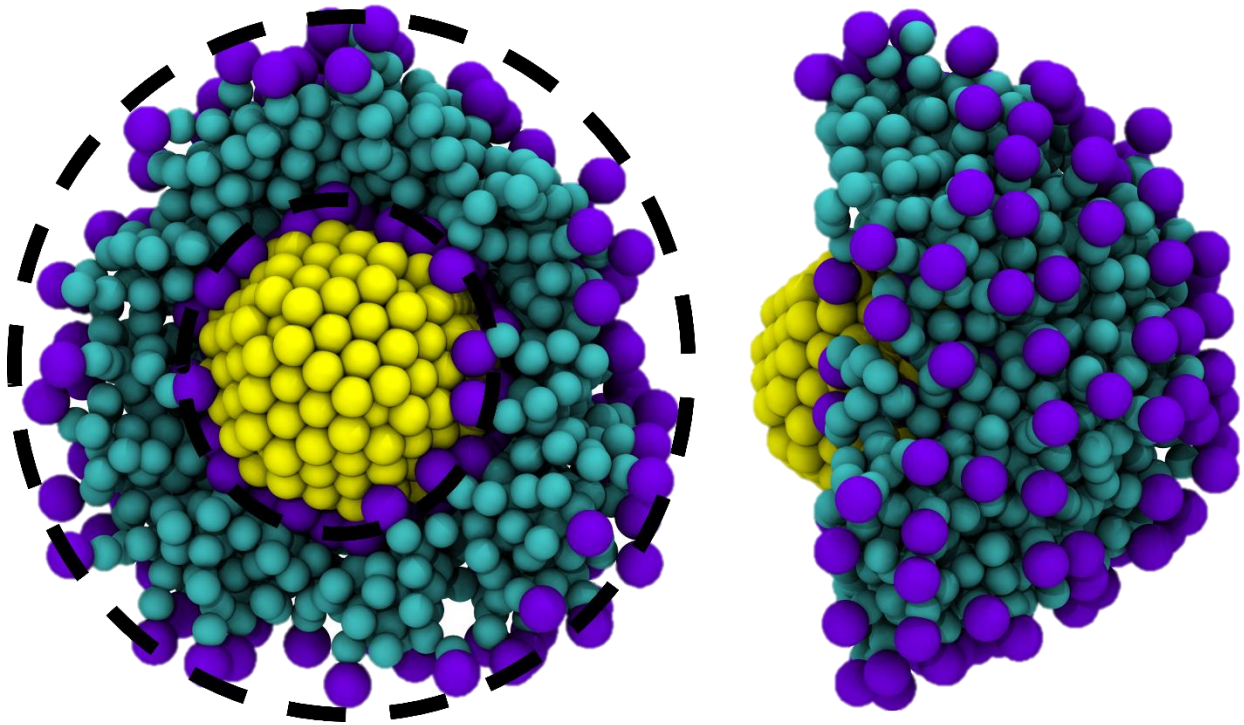


Figure 3.2: (Left) Snapshot showing a closer look at the vesicular structure. Surfactants that obstruct a direct visualization of the inner layer were removed for clarity. Concentric circles are used to depict the two different layers of the NPSC. (Right) Side view of same snapshot.

The effect of surface charge on the self-assembly process was studied by varying the surface charge density (σ) while keeping all other simulation parameters constant. Six different CG MD simulations were performed for σ values of 0, -0.33, -0.66, -1.0, -1.5 and -2.0 e . Corresponding values of Debye length, $1/\kappa$, and the zeta potential, ζ , were estimated by using DLVO theory^{12, 113} and reported in Table 3.2. The Debye length is a function of the ionic strength of the solution and is defined in Chapter 1 (Eq. 1.2). The dimensionless electric potential (scaled by $k_B T/e$) of the particle, ψ_p , is defined as

$$\frac{e\sigma_p}{\kappa\epsilon\epsilon_0k_B T} = \psi_p + \frac{\psi_p}{\kappa a} - \frac{\tau_1^2 \kappa a}{\tau_2 - \tau_1 \kappa a} \quad (3-1)$$

where e is the elementary charge carried by an electron (1.6×10^{-19} C), σ_p is the particle charge density in units of charge per unit area, κ is the inverse of Debye length, ϵ is the relative permittivity of the solvent, ϵ_0 is the relative permittivity of free space, k_B is the Boltzmann constant (1.38×10^{-23} m² kg s⁻² K⁻¹), T is the absolute temperature and a is the particle radius and τ_1 and τ_2 are defined as follows:

$$\tau_1 = 2 \sinh\left(\frac{\psi_p}{2}\right) - \psi_p \quad (3-2)$$

$$\tau_2 = 4 \tanh\left(\frac{\psi_p}{4}\right) - \psi_p \quad (3-3)$$

Table 3.2. Debye length ($1/\kappa$) and Zeta potential (ζ) for different values of NP surface charge density (σ).

Surface charge density (σ)	Debye length ($1/\kappa$) nm	Zeta potential (ζ) mV
0.00	0.47	0.00
-0.33	0.45	-28.98
-0.66	0.43	-39.90
-1.00	0.42	-46.75
-1.50	0.40	-53.25
-2.00	0.38	-57.89

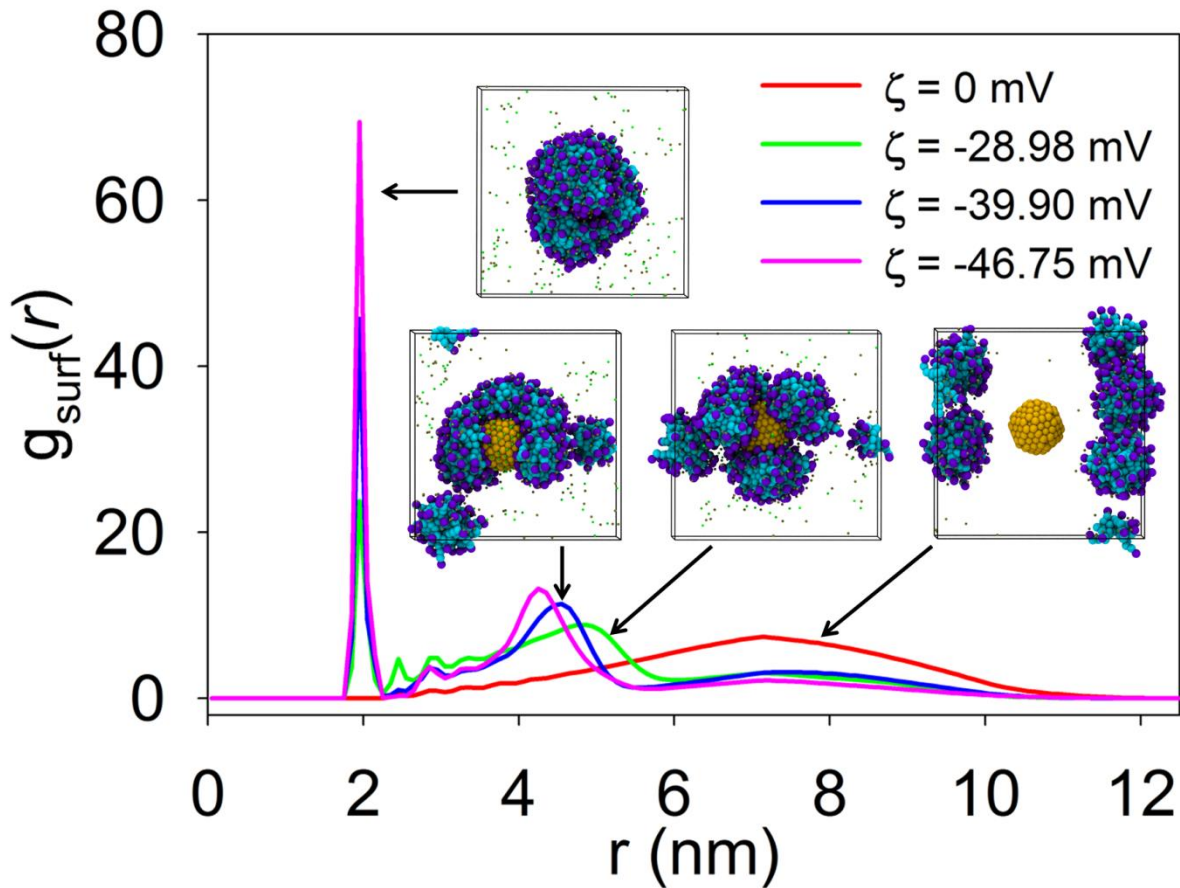


Figure 3.3: Effect of zeta potential (ζ) on metal NP-surfactant bilayer formation. The radial distribution function g_{surf} of the surfactant head groups as a function of distance r from the center of mass of the NP for four different values of $|\zeta|$, namely 0 mV (red), 28.98 mV (green), 39.90 mV (blue) and 46.75 mV (pink). The first peak, at a distance almost equal to the radius of the NP, indicates the inner layer and the second peak indicates the outer layer of the vesicle. Representative snapshots of the system at $t = 1\mu\text{s}$ are shown for each case.

The radial distribution function, $g_{\text{surf}}(r)$, of the surfactant head groups from the center of mass of the NP is plotted in Fig. 3.3 for increasing values of $|\zeta|$. For $\zeta = 0$ mV, the particle is

uncharged. Resultantly, there is no electrostatic interaction between the surfactant head groups and the particle as indicated by a single peak at a distance of 7 nm from the particle surface. As $|\zeta|$ is increased, two distinct peaks appear in $g_{\text{surf}}(r)$. The first peak is sharp and represents the first layer of the surfactant head groups that are bound to the NP surface while the second peak is shorter and broader and represents the head groups that constitute the second layer of the vesicle. Upon further increasing ζ , both peaks become taller and sharper, and for $\zeta = -57.89$ mV, a well-defined double layer assembly of surfactants is formed around the NP. In this range of ζ values, colloidal suspensions are stable and particles remain well-separated in solution¹². Hence, in a suspension consisting of multiple particles, such self-assembly can be expected to result in the formation of a stable dispersion of NPSCs. It is also important to note that NPSC formation does not occur in the case of positively charged NPs due to electrostatic repulsion between cationic surfactants and the NP surface. However, experiment-based hypothesis for NP-micelle interactions indicate that surfactants can self-assemble with cationic NPs through a tail-on approach which is driven by depletion forces. This is however not the case in our simulations and more detailed investigations of such systems might be needed to observe predicted behavior. As mentioned earlier, for the scope of this thesis, we will only consider negatively charged NP surfaces.

3.3.1.1. Kinetics of NPSC Formation

The kinetics of NPSC formation can be visualized from the MD trajectories. Here we discuss the kinetics of surfactant adsorption on the NP surface for zeta potential $\zeta = -46.75$ mV (Fig. 3.4). It is clearly observed that the inner layer (brown) is formed very rapidly (see inset) because of the strong electrostatic attraction between the surfactant head groups and the oppositely

charged NP surface. After the first 10-20 ns, a plateau is observed, suggesting that the surface coverage on the NP is sufficiently large to prevent further surfactant adsorption.

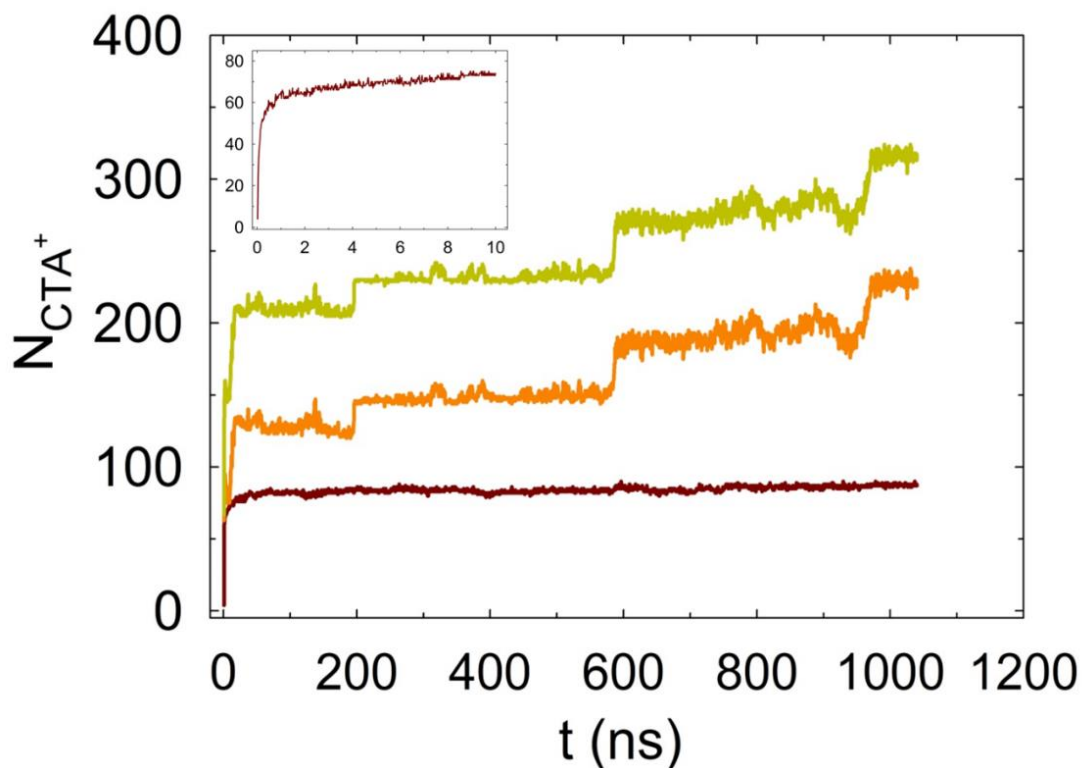


Figure 3.4: Plot of the number of surfactants adsorbed onto the NP surface vs. time during the formation of the bilayer. The growth of the inner layer (brown), outer layer (orange) and the entire bilayer (green) are all shown separately. The inset shows the growth kinetics of the inner layer during the first 10ns of simulation.

However, the outer layer of surfactants (orange) continues to grow because of the presence of free surfactant molecules and small micellar aggregates until the bilayer is saturated. The sudden step increase in the number of surfactants seen is a manifestation of surfactant aggregates

associating with the growing bilayer. As shown in Fig. 3.4, the adsorption of surfactants on the NP surface is characterized by two distinct regimes: a rapid adsorption regime in the first ~ 1 ns followed by a slower regime of ~ 10 ns before the number of adsorbed surfactants eventually reaches a plateau. This is consistent with experimental observations that suggest that the kinetics of adsorption of CTAB molecules typically follows a two-step mechanism, where fast monomer adsorption is followed by slower surface rearrangement¹¹⁴.

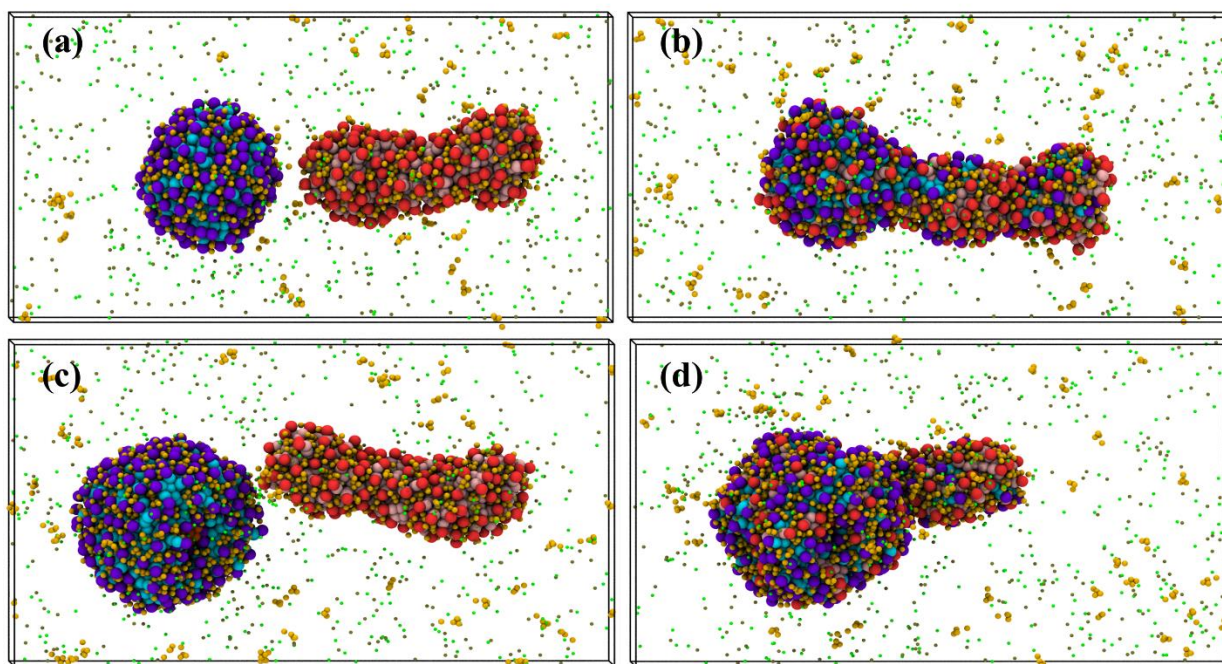


Figure 3.5: Junction formation between a NPSC and rodlike micelle. Snapshots of the CGMD simulation system before and after junction formation for the (a, b) corona-like NPSC and (c, d) vesicle-like NPSC. In order to differentiate between the CTA⁺ surfactants of each species they have been colored differently. CTA⁺ in the micelle is represented by red head groups and pink tail groups whereas CTA⁺ in the NPSC is represented by violet head groups and cyan tail groups. NP (yellow), Sal⁻ (orange), Na⁺ (green) and Cl⁻ (tan) counter ions are also shown.

3.3.2. Self-Assembly of NPSCs with Rodlike Micelles

In all simulations, we observed that the interaction of rodlike micelles with either a corona-like structure or a vesicular structure, in the presence of NaSal salt, resulted in the formation of stable junctions primarily through the opening up of the endcap of the micelle. Figure 3.5 shows representative snapshots of this process before and after junction formation for both the corona-like and vesicle-like particles. The formation of such junctions is a consequence of the higher free energy of the micellar endcaps and salt-induced screening of the electrostatic repulsion between the surfactant head groups of the NPSC and the micelle. This mechanism of junction formation is consistent with the inference from isothermal titration calorimetry and scattering experiments by Helgeson et al.²⁸ that CTAB surfactants can adsorb onto the NP surface and further interact with WLMs in the bulk to form stable junctions in the presence of sodium nitrate salt. Jodar-Reyes and Leermakers^{29, 30} have developed a self-consistent field theoretic framework to model the interactions between linear rodlike micelles and surfactant covered surfaces. Their predictions suggest that for moderately hydrophilic surfaces with a bilayer of surfactants on the surface, the formation of micellar stalks at the solid-solution interface can favor junction formation. These stalks are thermodynamically stable when the micellar endcap energy exceeds the energy required for adsorption of the stalks on the surface. Helgeson and Wagner¹¹⁵ have also derived a statistical mechanical model that takes into account the end-adsorption of WLMs, and is capable of predicting, a priori, the suspension microstructure and colloidal phase behavior for a wide range of WLM-NP solutions. The CGMD simulations discussed above clearly demonstrate the formation of electrostatically stabilized junction formation in such systems.

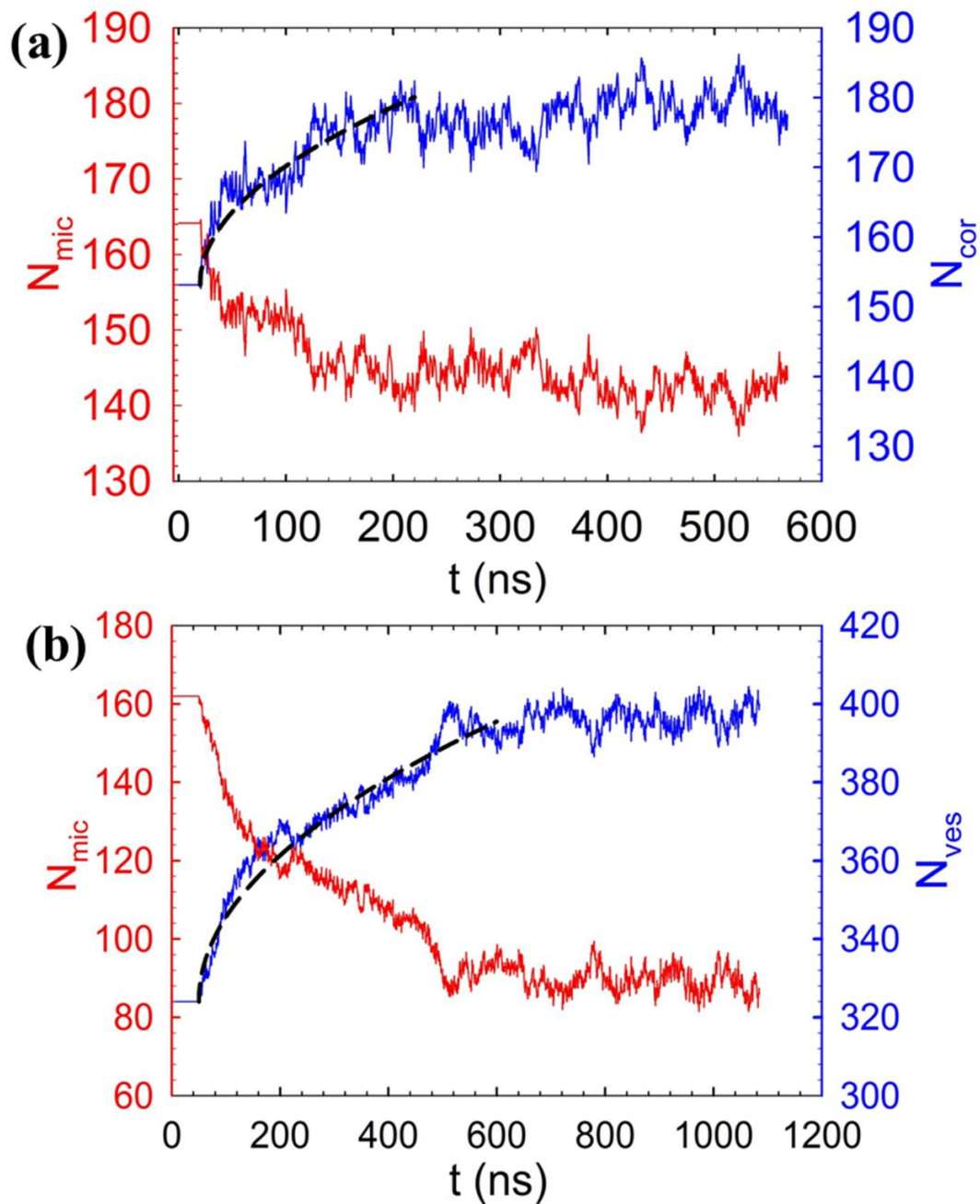


Figure 3.6: Surfactant exchange rates during junction formation. A plot of the total number of surfactants present in the (a) vesicle-like (blue) and (b) corona-like (blue) (right hand side Y-axis) and the micelle (red) (left hand side Y-axis) as a function of time clearly indicating the net transfer of surfactants from the micelle to the NPSC. Dotted black line in both cases indicates a \sqrt{t} dependence which suggests a diffusion-limited exchange process.

3.3.2.1. Surfactant Exchange Dynamics

We quantified the surfactant exchange between the micelle and NPSC during the bridging process. The criterion to determine whether a surfactant is part of the micelle or the NPSC was obtained from the appropriate peak locations in the radial distribution function of the surfactant head groups with respect to the center of mass of the NP, i.e., the second peak for a vesicle (5.2 nm) and the only peak for a corona (4 nm). All surfactants with centers of mass that fell within the above cut-offs were considered to be parts of the NPSC. For both the corona and vesicular structures, there was a net transfer of surfactants from the micelle to the NPSC as shown in Fig. 3.6 where the total number of surfactants present in the micelle, corona or vesicle is plotted as a function of time.

Surfactant exchange is a direct consequence of the endcap opening and bridging process whereby surfactants are free to move between the two structures. The net transfer of surfactants from the micelle to the NPSC is dictated by the number of surfactants that can be accommodated within the monolayer or bilayer. The exchange process has a pronounced diffusive regime, signified by a square root dependence on time of the number of surfactants exchanged. The diffusive regime is ≈ 200 ns for the corona and is significantly longer (≈ 600 ns) for the vesicle. The plateau following the diffusive regime indicates saturation of the NP-surfactant complexes. The temporal fluctuations in the number of surfactants in the plateau regime imply that surfactants continue to be exchanged between the NPSC and the micelle, suggesting a state of dynamic equilibrium. Note that the relatively long time scales of the NPSC-micelle complexation process underscore the importance of performing MD simulations over microsecond time scales.

3.3.2.2. Energetics of Junction Formation

The summation of the pairwise potential energies of the NP, CTA⁺ and Sal⁻, denoted here by Φ , was calculated as a function of time during the junction formation process. As shown in Fig. 3.7, a clear transition from a higher energy state (before junction formation) to a lower energy state (after junction formation) can be observed. The initial system consists of a spherical NPSC and a rod-like micelle with two end caps. Merger of these two structures results in the disruption of the spherical symmetry of the surfactant assembly on the NPSC as well as in the loss of one of the end caps of the micelle, both of which result in a rearrangement of surfactants in the NPSC-micelle composite. This indirectly influences the total energy of the system, as reflected in the observed decrease in the total pair-potential energy, Φ .

For the bilayer-micelle bridging process, the difference in pair-potential energy $\Delta\Phi$ between the initial and final states, averaged over three simulation runs, is ≈ 1050 kJ/mol (≈ 420 k_BT). Corresponding value of $\Delta\Phi$ for the corona-micelle junction formation is ≈ 565 kJ/mol (≈ 227 k_BT), which is almost one half of the energy change in the bilayer case. Further, micelle end cap energy, E_{cap} , has been estimated to be on the order of ~ 10 k_BT¹⁷. Therefore, it is clear that the energy required for the formation of end caps is greater than the energy required for junction formation which means that the junctions are thermodynamically stable. In both cases, $\Delta\Phi/k_{B}T \gg 1$, suggesting that the electrostatically stabilized NPSC-micelle complexes are immune to breakage by thermal fluctuations. MD simulations were performed to verify that these structures remained intact over a period of 1 μ s. The remarkably long shelf life and maintenance of optical properties over the period of weeks of plasmonic nanogels formed by the self-assembly of WLMs and noble metal NPs could be attributed to the stability of the NP-micelle junctions.

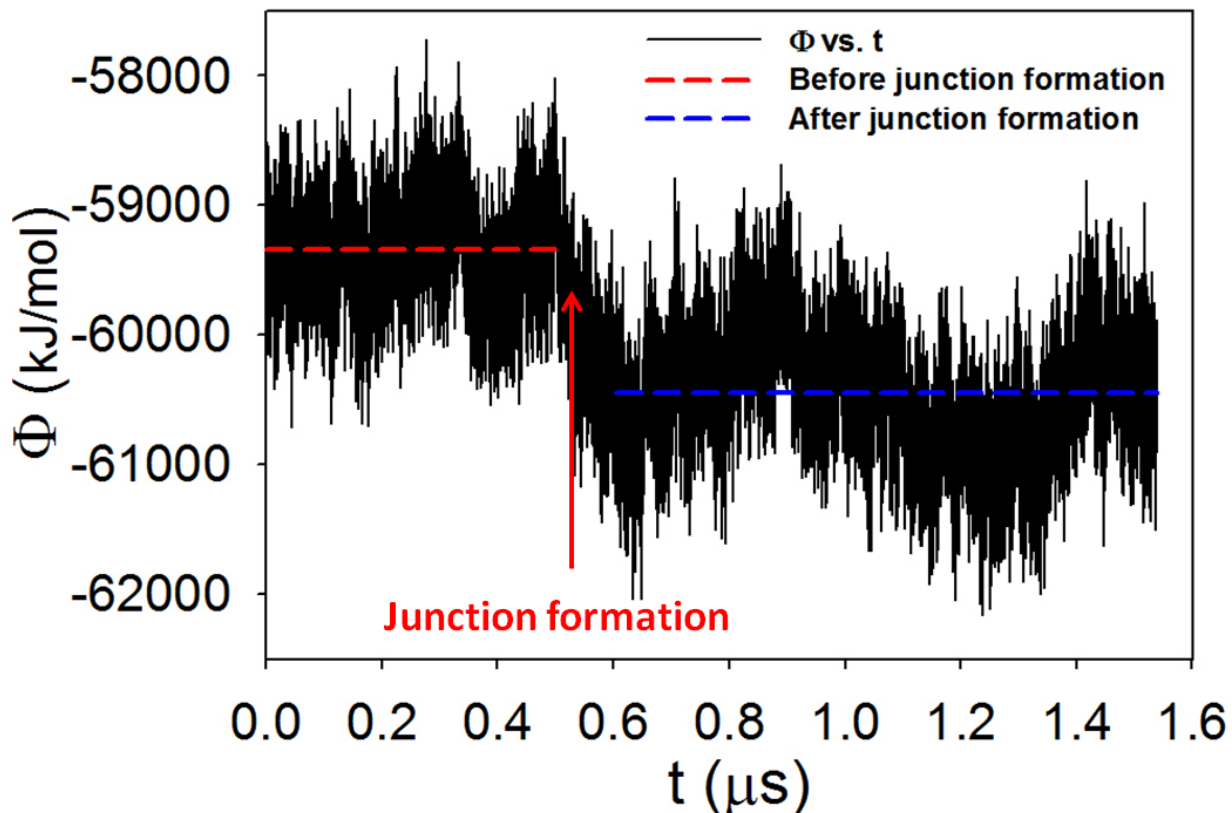


Figure 3.7: Energetics of junction formation. A plot of the summation of pair potential energies Φ of the NP, CTA⁺ and Sal⁻ complex as a function of time indicating a decrease in Φ of ~ 1050 kJ/mol associated with junction formation in the case of a vesicle-like NPSC bridging with a rodlike micelle.

3.4. Conclusions

Coarse-grained molecular dynamics (CG MD) simulations have been developed to study the self-assembly of metallic as well as hydrophobic NPs with CTAC surfactant micelles. We find that negatively charged metal NPs form a vesicular structure with a bilayer of surfactants on their surface. The surfactant head groups are electrostatically attracted to the NP surface leaving the tail

groups exposed to the solvent. This results in a large free energy penalty which results in a second layer of surfactants that self-assemble such that the tail groups of the two layers are interdigitated. Alternatively, uncharged, hydrophobic NPs form a corona-like monolayer with the tail groups of surfactants adsorbed onto the surface of the NP. The effect of surface charge, which is characterized by the zeta potential, on the stability of the bilayer was investigated and it was found that the bilayer is stable for $\zeta < -45$ mV. Radial distribution functions along with representative snapshots of the system show the formation of patchy admicelles at relatively lower surface charges and complete bilayers at $|\zeta| > 45$ mV.

Further, it was found that NPSCs, upon interacting with rodlike micelles in the presence of NaSal salt, form stable junctions primarily through the opening up of the end cap of the micelle. This mechanism of self-assembly is consistent with, and confirms, hypothesis from self-consistent field theories and titration calorimetry measurements. Surfactant exchange between the micelle and NPSC was found to be a diffusion-limited process before it reaches a state of dynamic equilibrium. Stabilization energy of the NPSC-micelle complex was calculated to be $\sim O(100 k_B T)$ which is much less than the micelle end cap energy and consistent with the experimentally observed long shelf life of plasmonic nanogels formed by the self-assembly of WLMs and noble metal NPs²⁴. In Chapter 4, the methodology developed here is extended to solutions containing multiple NPs and micelles which will allow us to systematically probe the flow-microstructure coupling and rheology of such systems through MD simulations.

Chapter 4

Microstructure and Rheology of Nanoparticle-Wormlike Micelle Mixtures

4.1. Introduction

Self-assembly in surfactant solutions is known to result in diverse micelle morphologies that include spheres, cylinders, bilayers and highly ordered liquid crystal structures. Among these, wormlike micelles (WLMs) have generated great fundamental and practical interest because of their easily tunable microstructure and rich rheological behavior. Due to their structural similarity to polymers, the constitutive behavior of WLMs is governed by reptation dynamics along with the equilibrium dissociation and recombination process^{1, 116}. The size, morphology and entanglement density of WLMs greatly depends upon the surfactant concentration, chemical environment, temperature, and flow shear. Such solutions could exhibit Newtonian, shear thinning, or shear thickening behavior, which is accompanied by shear-induced structure (SIS) formation or shear banding. WLMs are ubiquitous and find applications in various consumer products, such as soaps, cosmetics and detergents², hydrofracking fluids³, and active nanomaterials that can be used for energy harvesting and nanoparticle templating.

The effect of added salt on the growth of charged micelles is well understood^{15, 16, 117}. Several experiments, molecular simulations and theories have shown that the presence of salt at sufficient concentrations can promote sphere-to-rod transition and aid the formation of longer micelles. Further, it has been shown that organic, hydrotropic salts such as sodium salicylate (NaSal) tend to screen the electrostatic repulsion between the surfactant head groups more

effectively because of their bulky ring structure and therefore can promote fusion of micelles, SIS formation and shear thickening at much lower salt/surfactant ratios^{18, 19, 21}.

Recent studies have shown that the addition of nanoparticles (NPs) to WLM solutions can not only add functionality to the resulting material but also result in changes in microstructure, phase behavior, and rheology. Further, it has been shown that these NPs can associate themselves with the micellar end caps to form a compact double network of entanglements that produces a significant buildup in viscosity and viscoelasticity. Previous studies have presented contradictory ways in which colloidal particles self-assemble with WLMs. Bandopadhyay and Sood¹¹⁸ claim that the association comes from electrostatic interactions between the particle surface and the surfactant head group and that the viscosity varies non-monotonically with NP concentration. Nettekshiem et al.¹⁰⁴ suggest that the NPs materially participate in the WLM network and that the viscosity increase is monotonic. The primary difference in the above studies was in the surface chemistry of the NPs.

Although myriads of experiments have been performed on micellar systems and micelle-NP mixtures^{24, 28, 112, 119}, molecular explorations of the microstructure-rheology coupling in such systems are still lacking. Briels et al.⁷⁰ have studied the structure, dynamics and rheology of WLM solutions through stochastic simulations for which parameters were obtained from fully atomistic simulations. Sangwai et al.^{19, 44} have shown the sphere-to-rod transition and binary interactions of cationic cetyltrimethylammonium chloride (CTAC) micelles using coarse-grained molecular dynamics (CG MD) simulations and Dhakal et al.¹⁷ have performed large-scale equilibrium simulations that demonstrated the anomalous viscosity variations in CTAC/NaSal micellar solutions. Further, in chapter 2, we have also shown that such CG models can effectively capture

the non-equilibrium configurational dynamics and scission of cylindrical and semiflexible wormlike micelles under shear and uniaxial extensional flow.

In chapter 3, we have studied the self-assembly of NP-surfactant complexes with rodlike CTAC micelles through faithful CGMD simulations¹²⁰. Our results suggested that it was favorable to form stable NP-micelle junctions through a mechanism by which the micelle end cap bridges to the surfactant-covered NP surface. The effect of NP surface chemistry and charge on the dynamics, energetics and nature of self-assembly was also discussed. In this chapter, we present a more systematic study of the structure and rheology of mixtures of CTAC/NaSal micelles and negatively charged NPs in the presence of explicit hydrodynamics and long-range electrostatic interactions. The effect of particle volume fraction (ϕ_p) and salt/surfactant ratio, R , on the equilibrium structure and zero-shear viscosity is discussed. Further, a non-linear shear thinning regime is identified accompanied by a shear-induced isotropic to nematic transition beyond $Wi \sim 1$. Finally, the evolution of the first normal stress difference, N_1 , as a function of time and Wi is also discussed.

4.2. Simulation Methods

4.2.1. The CG MD Model

In this study, we perform all our simulations using the LAMMPS MD package¹²¹ and the Martini force field developed by Marrink et al.⁷² The CG models for CTA⁺ and Sal⁻ have been described in great detail in previous chapters. However, the NP model described in Chapter 3 is slightly modified in this study. In Chapter 3, we used a nanoparticle that consisted of several CG beads that made up the inner core of the NP. These CG beads do not contribute to the self-assembly and unnecessarily increase computational time, thereby reducing simulation efficiency. This

reduction in efficiency is not significant when we have only one particle in the system, which was the case in Chapter 3. Now, we are trying to simulate several NPs in solution and therefore, getting rid of all the inner CG beads would reduce the number of beads in the simulation by thousands. Further, the NPs used previously were faceted rather than being perfect spheres. While there are arguments to suggest that NPs are never perfect spheres in solution, in order to explore the effects of nanoscale curvature we would like to model a perfectly spherical NP. Therefore, the NP was modeled in such a way that it had a non-interacting core which was made up of a single bead that was slightly smaller than the diameter of the NP and a negatively charged surface which consisted of many small beads with fractional charges on them. The core bead only had Lennard-Jones (LJ) type interactions with all constituent species and no coulombic interactions were assigned to it. All the other CG beads in the system had both LJ and coulombic interactions with a global cut-off of 1.4 nm for both types. The interaction between the surface beads and the core bead was defined by means of a Morse potential, which is of the form,

$$V(r) = D_0[e^{-2\alpha(r-r_0)} - 2e^{-\alpha(r-r_0)}] \quad (4-1)$$

where $D_0 = 119.5$ KCal/mol is the depth of the potential well, $\alpha = 0.7$ angstroms controls the width of the well, $r_0 = 2.22$ nm is the equilibrium distance between the two beads and $r_c = 2.55$ nm is the cut-off beyond which no interactions are calculated. These values were estimated on a trial and error basis and were chosen to make sure that the charged surface beads did not escape from the potential well at any point during the simulation. The size of the NP, d , was kept constant in all our simulations and $d = 4.5$ nm. The choice of NP size was based on the fact that 4-5 nm is the

smallest possible size that can be synthesized experimentally in a monodispersed fashion¹²². Further, 4.5 nm is also roughly equal to the average diameter of a CTAC micelle in aqueous solution. Due to the presence of several charged species in our system, we calculate long-range electrostatic interactions using the particle-particle particle-mesh (PPPM) solver¹²³ which is very similar to the particle-mesh Ewald (PME) technique (used in Chapter 1 & 2) but has the advantage of being faster for system sizes on the order of 10000 beads¹²⁴.

4.2.2. Viscosity Calculation from MD Simulations

The shear viscosity of a fluid can be determined very easily using experimental techniques such as rheometry. Knowledge of the viscosity of a fluid under a given set of conditions is important not only from a processing and handling perspective, but also from the point of view of computational modeling and force field development. Most parameters that are used for parametrizing force fields for MD simulations are thermodynamic in nature. Viscosity is a kinetic property of a fluid and it influences the diffusion and conformational changes of molecules that are solvated in the fluid. This makes it a very useful quantity in terms of model development. There are several methods that can be used to determine the shear viscosity of a fluid using MD simulations. Equilibrium methods utilize pressure or momentum fluctuations in the system¹²⁵ whereas non-equilibrium methods make use of steady-state shear flow to estimate shear viscosity¹²⁶. A quick overview of the equilibrium and non-equilibrium methods is given below.

4.2.2.1. Equilibrium MD: Pressure Fluctuations

The shear viscosity of a liquid is related to the fluctuations of the off-diagonal elements of the pressure or stress tensor. The viscosity can be calculated from an equilibrium simulation by integrating the Green–Kubo formula¹²⁷:

$$\eta = \frac{V}{k_B T} \int_0^\infty \langle \tau_{xz}(t_0) \tau_{xz}(t_0 + t) \rangle dt \quad (4-2)$$

where V is the volume of the simulation box, k_B is the Boltzmann constant and T is the absolute temperature. This can be reformulated in the form of an Einstein relation:

$$\eta = \lim_{t \rightarrow \infty} \frac{1}{2} \frac{V}{k_B T} \frac{d}{dt} \langle (\int_{t_0}^{t_0+t} \tau_{xz}(t') dt')^2 \rangle \quad (4-3)$$

Equilibrium methods converge very slowly because the pressure fluctuations are extremely large in MD simulations due to the small size of the system. The temporal autocorrelation of the pressure scales as $t^{-3/2}$, and therefore accurate estimations of viscosity would require long time scale simulations.

4.2.2.2. Non-equilibrium MD (NEMD): SLLOD Algorithm

The most widely used non-equilibrium approach for viscosity calculations is the SLLOD algorithm¹²⁸. The system is subjected to a shear velocity and the momentum flux or shear stress is measured as a response to the imposed shear strain. The viscosity at a given shear rate is given by:

$$\eta(\dot{\gamma}) = -\frac{\tau_{ij}}{\dot{\gamma}} \quad (4-4)$$

where τ_{ij} is an off diagonal component of the stress tensor such that i is the flow direction and j is the gradient direction. For this method, a modified form of the Lees-Edwards sliding brick boundary condition is utilized and for charged systems, a modification of the Ewald summation is also necessary. The disadvantage of this method is that it imposes a linear velocity profile at the atomistic level which is not necessarily the case in experiments. Further, in order to achieve a Couette flow behavior, the equations of motion are modified in a non-Hamiltonian way. This can result in an overall rotation in the system.

4.2.2.3. Reverse NEMD (RNEMD)

The RNEMD approach uses the Muller-Plathe algorithm¹²⁹ in which an unphysical momentum exchange is done between two particles in different regions of the simulation box. The system responds to the unphysical imposed momentum flux by establishing a real momentum flow in the opposite direction. This sets up velocity profiles in the upper and lower halves of the simulation box. The slope of the resulting velocity profiles is used to estimate the shear rate. The number of particles that swap momentum and the frequency of momentum swapping are the two

parameters that control the resulting velocity profile. This is exactly opposite to the traditional NEMD technique in which the momentum flux is a response to the imposed shear velocity.

One disadvantage of using this method is that it works only for a small range of shear rates¹³⁰. For very high momentum flux, we observe a non-linear, parabolic velocity profile and at low momentum flux the resulting profile is again non-linear with very large fluctuations. However, the range of shear rates that are accessible using this method is sufficient for the scope of this study. Another reason for choosing this method over the traditional NEMD method was due to a limitation in LAMMPS. In order to be able to compute long-range electrostatic interactions using the PPPM solver in LAMMPS the simulation box needs to remain orthogonal at all times. Using conventional NEMD simulations would deform the box due to the imposed velocity and therefore make it non-orthogonal.

4.2.3. MD Simulations of WLM-NP Solutions

In this work, we fixed the surfactant concentration $C_D = 0.25$ M. The size of our simulation box was roughly 27 nm on each dimension which resulted in a total of 3000 CG surfactant molecules. We perform simulations at four different values of R namely 0.1, 0.33, 0.67 and 1.0. Further, for each value of R , we perform 14 different simulations by gradually increasing ϕ_p from 0 to 6%. Apart from the CTA⁺, Sal⁻ and NPs the system also consisted of ~130000 CG water beads out of which ~15% were replaced with the antifreeze water molecule to prevent freezing at room temperature. Appropriate number of Na⁺ and Cl⁻ counterions were added to maintain electrical neutrality in the system. The total number of CG beads in the system varied between ~155000 and 165000 depending upon the salt concentration and NP volume fraction. Figure 4.1 shows a

schematic of the nanoparticle, the flow field and the simulation box. The time step used for all our simulations was 10 fs. Periodic boundary conditions were assigned in all three directions. A total of 56 equilibrium simulations were run in an NVT ensemble at 300 K for roughly 300-400 ns each. Once the equilibrium simulations were completed, we performed 20 different RNEMD simulations on each case, which resulted in a total of 1120 simulations. Each RNEMD simulation was performed for ~ 30 -40 ns which was sufficient to obtain quantities such as shear viscosity, η and N_1 . The flow was along the x-direction and the gradient was along the z-direction.

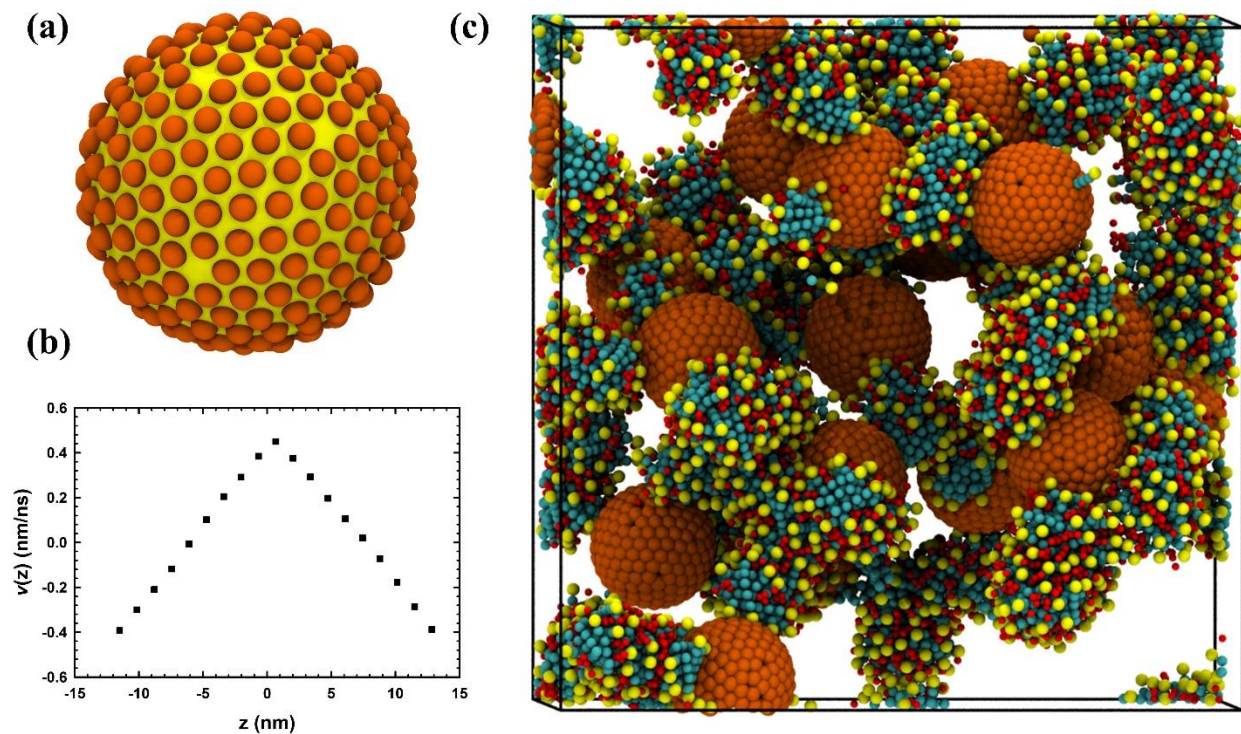


Figure 4.4: (a) Schematic of nanoparticles (yellow core and orange surface) used in simulations. (b) Schematic of the velocity profile in the shear gradient plane in a RNEMD simulation. (c) Schematic of the micelle-NP complex used to study the rheology. CTA⁺ (cyan tails and yellow heads), Na⁺ (red) and NP surface (orange) are shown. Water and other ions removed for clarity.

4.3. Results and Discussion

4.3.1. Equilibrium Rheology

We observe that at a fixed surfactant concentration the zero-shear viscosity increases monotonically with increasing NP concentration for all values of R (Fig. 4.2). Further, at the simulated surfactant concentration, this viscosity increase is independent of the salt concentration and increases linearly with ϕ_p . This is consistent with experimental observations of Helgeson et al.²⁸ in which 30nm silica NPs were added to CTAB/NaNO₃ mixtures in the semi-dilute and entangled regimes.

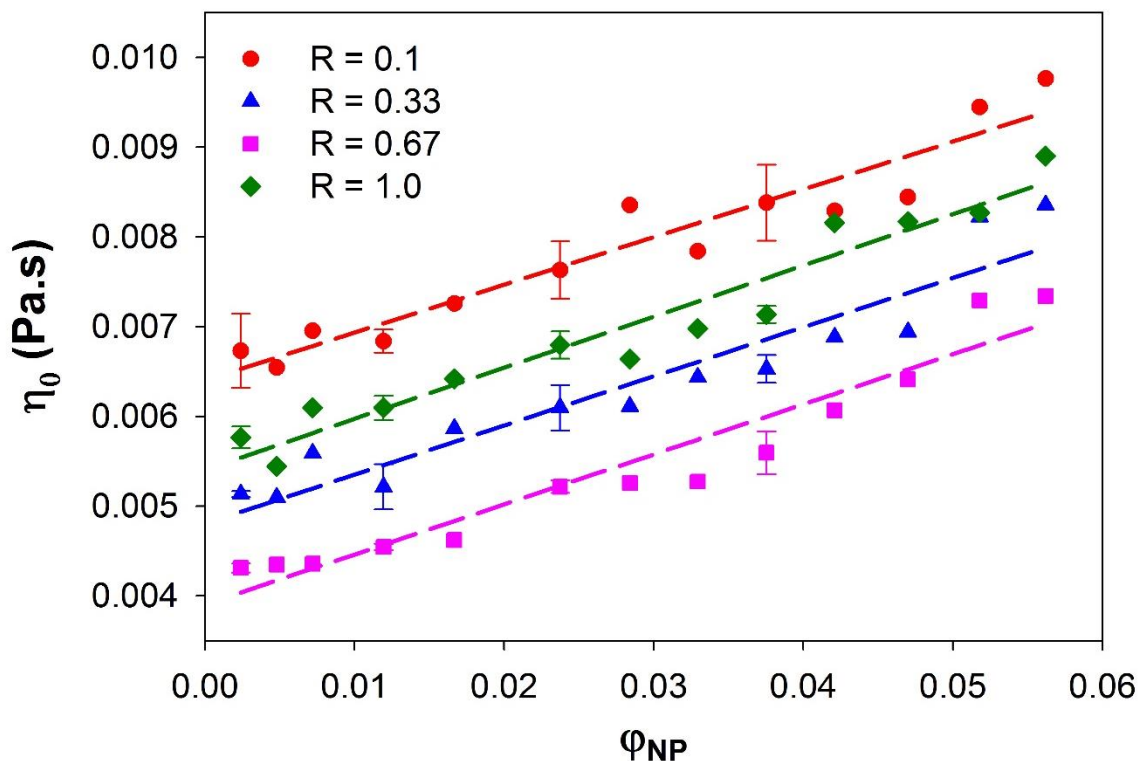


Figure 5: Zero-shear viscosity η_0 as a function of ϕ_p for different values of R and for a fixed $C_D = 0.25$ M. η_0 increases linearly with ϕ_p and non-monotonically with increase in R .

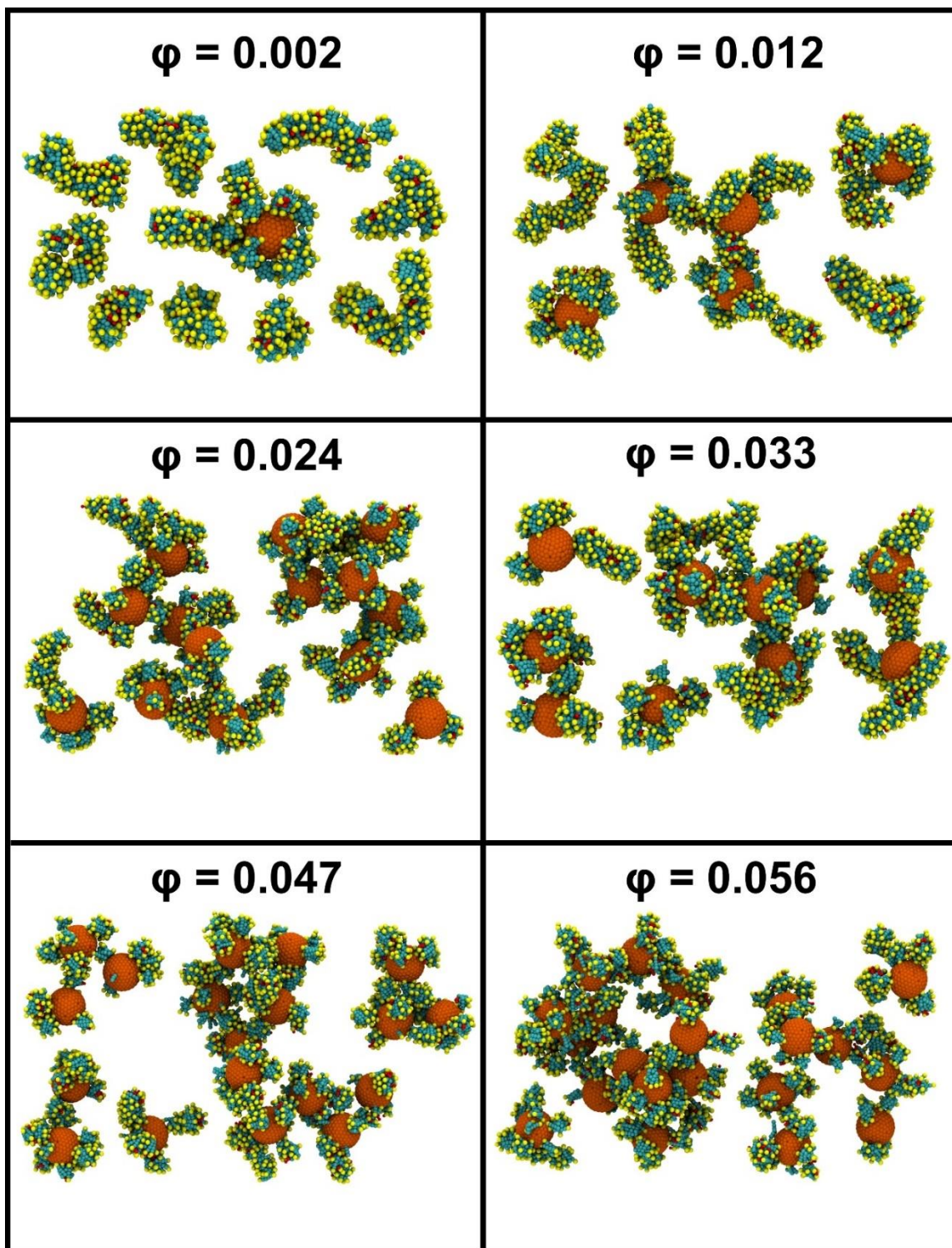


Figure 4.6: Microstructures observed in simulations at various nanoparticle concentrations for $R = 0.1$. Number of micelle-NP junction increases with the NP concentration.

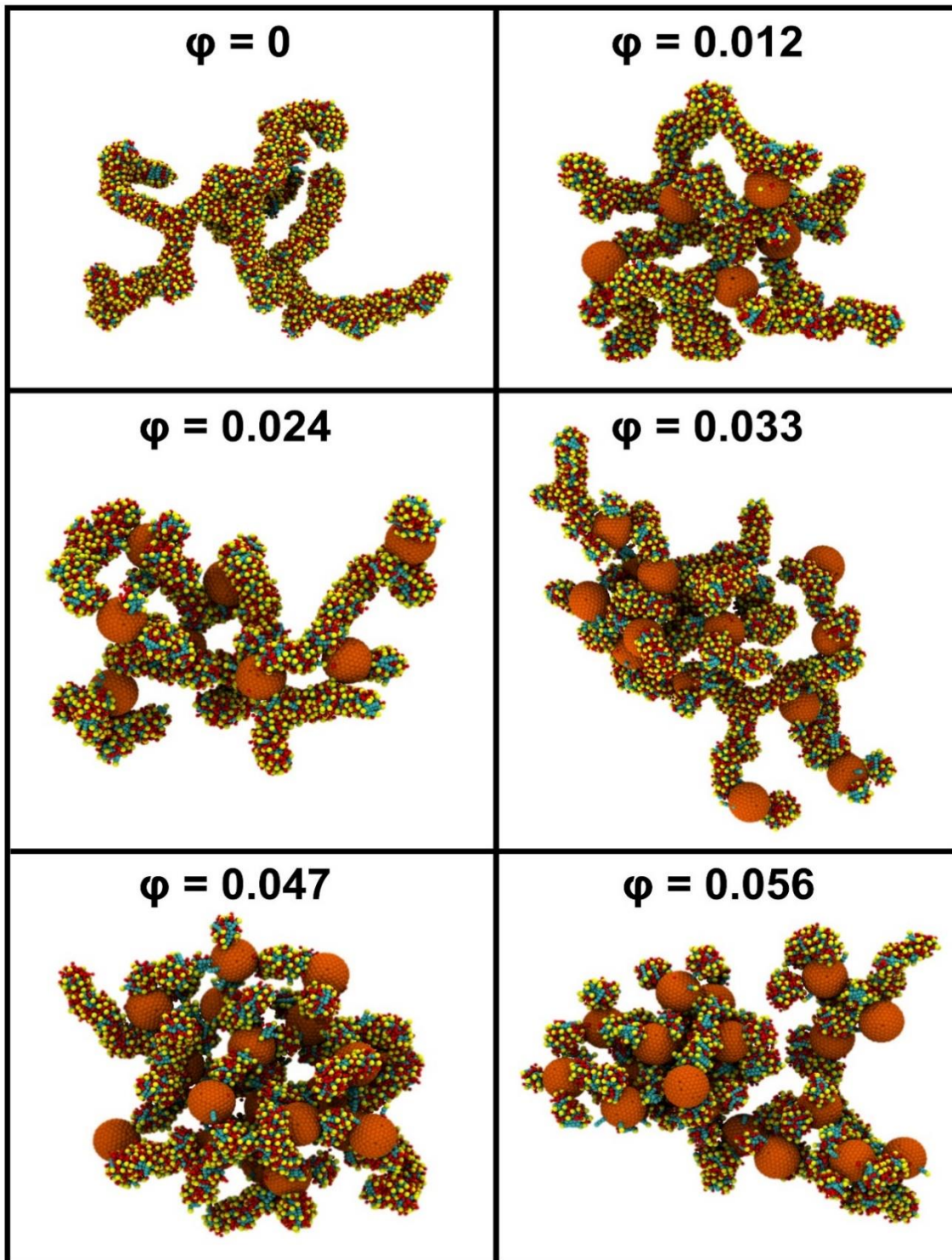


Figure 4.7: Microstructures observed in simulations at various nanoparticle concentrations for $R = 1.0$. Number of micelle-NP junction increases and micelle branches vanish with φ_p .

At low salt concentrations, the solution is composed of rod-like and worm-like micellar aggregates. In such solutions, addition of NPs results in the formation of micelle-NP junctions which results in the effective lengthening of micellar aggregates. As more particles are added to the system, several of these micelle-NP junctions connect with each other thereby creating entanglements in dilute solutions which are otherwise non-entangled. This in turn manifests as an increase in viscosity and viscoelasticity. Fig. 4.3 shows an array of micellar structures for $C_D = 0.25$ M, $R = 0.1$ and φ_p in the range of 0.002-0.056. Note that in Fig. 4.3 only a few of the largest aggregates are shown and that the actual system has a lot of smaller aggregates, free surfactants, salt, counterions and water that have been removed for the sake of clarity. Another point to note is that the particle sizes in all our simulations were constant and that the images in each panel are scaled differently. This means that structures at lower NP concentrations might seem comparable in size to structures at higher NP volume fractions when in reality they are actually much smaller. Similarly, for $R = 1$, we can see that when $\varphi_p = 0$ the system consists of long, branched micellar fragments (Fig. 4.4). However, as φ_p is gradually increased to 0.056 the micellar branches disappear and the system is essentially composed of multi-connected, entangled micelle-NP junctions. However, micelle-NP branches observed here are structurally different from the branches observed in micelles at higher concentrations in the absence of NPs. Branching in micellar solutions has been shown to result in a decrease in viscosity due to a faster stress relaxation mechanism that arises due to the presence of sliding junctions¹³¹. On the other hand, micelle-NP branches are more rigid and the sliding mechanism does not apply to these branch points. This results in an increase in the viscosity and is much greater than the Einstein viscosity predicted for a dilute suspension of spheres¹³ which is given by:

$$\hat{\eta} \approx \eta(1 + \frac{5}{2}\varphi) \quad (4-5)$$

where $\hat{\eta}$ is the effective viscosity of a colloidal suspension, η is the viscosity of the ambient fluid and φ is the volume fraction of spheres in the suspension.

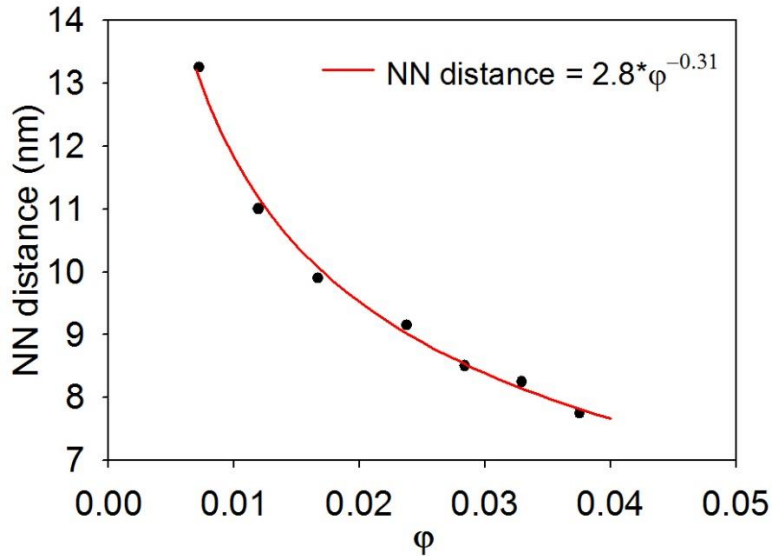


Figure 4.8: Nearest neighbor (NN) distance as a function of φ_p for $R = 1$ shows that NN distance $\sim \varphi_p^{-1/3}$. The red line indicates the fit.

This further confirms that the NPs effectively participate in the WLM network and occupy an effective volume much greater than the actual volume fraction of NPs in solution, thus contributing to a significant buildup in the viscosity. Unlike in experiments, MD simulations can

provide us with a direct estimate of the particle functionality and it is observed that each NP can have 3-4 micelles physically adsorbed on its surface. This is again consistent with the results reported in literature²⁸. We also plot the nearest neighbor distance for the NPs and observe that the NPs are well dispersed and the nearest-neighbor distance scales as $\sim \varphi_p^{-1/3}$ (Fig. 4.5). In other words, the distance (units of length) follows a power law relation with φ_p (units of volume) with an exponent of -1/3, which is intuitive.

We also observe that η_0 varies non-monotonically with the salt concentration (R) for the given surfactant concentration. At R = 0.1 the system is composed primarily of WLMs and a few rod-like micellar aggregates. At R = 0.33 onset of branching results in a slight decrease in solution viscosity. At the microstructural level, this is the point at which the effective charge of the micelle reverses due to the amount of counterions adsorbed on its surface. These observations have been reported for several surfactant systems. At R = 0.67, more branched structures are formed which further decreases the viscosity. However, at R = 1, sufficient salt is present in the system to facilitate the merger of several branched micelles and a multi-connected elastic network is formed as a result of which the viscosity goes up again. The increase in viscosity from the branched state to the network stage is attributed to the increased rigidity of the network. This behavior has been observed for CTAB/NaSal systems both via experiments and molecular simulations^{17, 18}.

4.3.2. Shear Rheology

In order to estimate the shear viscosity, we perform RNEMD simulations that span 3-4 decades of shear rates for solutions at $C_D = 0.25$ M and R = 0.1, 0.33, 0.67 and 1.0 for all φ_p values

ranging from 0 to 6%. We calculated the stress across the shear-gradient plane, τ_{xz} , velocity profile in the shearing direction and normal stress differences which are defined as follows¹³².

$$N_1 = \tau_{xx} - \tau_{zz} = \Psi_1 \dot{\gamma}^2 \quad (4-6)$$

$$N_2 = \tau_{zz} - \tau_{yy} = \Psi_2 \dot{\gamma}^2 \quad (4-7)$$

where N_1 and N_2 are the first and second normal stress difference respectively. τ_{ij} are components of the stress tensor with $i, j = x, y, z$, and Ψ_1, Ψ_2 are first and second normal stress difference coefficients, respectively. For simple viscoelastic fluids with fading memory, at low shear rates, the normal stress differences depend quadratically on shear rate and the shear stress is linear in shear rate. This behavior can be observed for the CTAB/NaSal/NP systems as well (Fig. 4.6). Therefore, by definition, Ψ_1 and Ψ_2 will be a constant for low shear rates and then decrease rapidly.

In a typical simulation, approximate values can be assumed for the shear rate, $\dot{\gamma} \approx 10^9 \text{ s}^{-1}$, density, $\rho \approx 10^3 \text{ kgm}^{-3}$, shear viscosity, $\eta \approx 0.02 \text{ Pa} \cdot \text{s}$ and the box size $L \approx 27 \text{ nm}$. The Reynolds number (Re) is given by:

$$Re = \frac{\dot{\gamma} \rho L^2}{\eta} \quad (4-8)$$

For the values listed above, $Re \approx 0.04$. At such a low Reynolds number, one would expect the inertial forces being negligible as compared to the viscous forces and one would expect laminar

flows with a smooth constant fluid motion. In such a laminar flow regime, the relevant dimensionless quantity is the Weissenberg number defined as $Wi = \dot{\gamma}\tau_R$, where τ_R is the longest relaxation time of the microstructure. For the rest of the discussion, we used Wi to define the deformation rate.

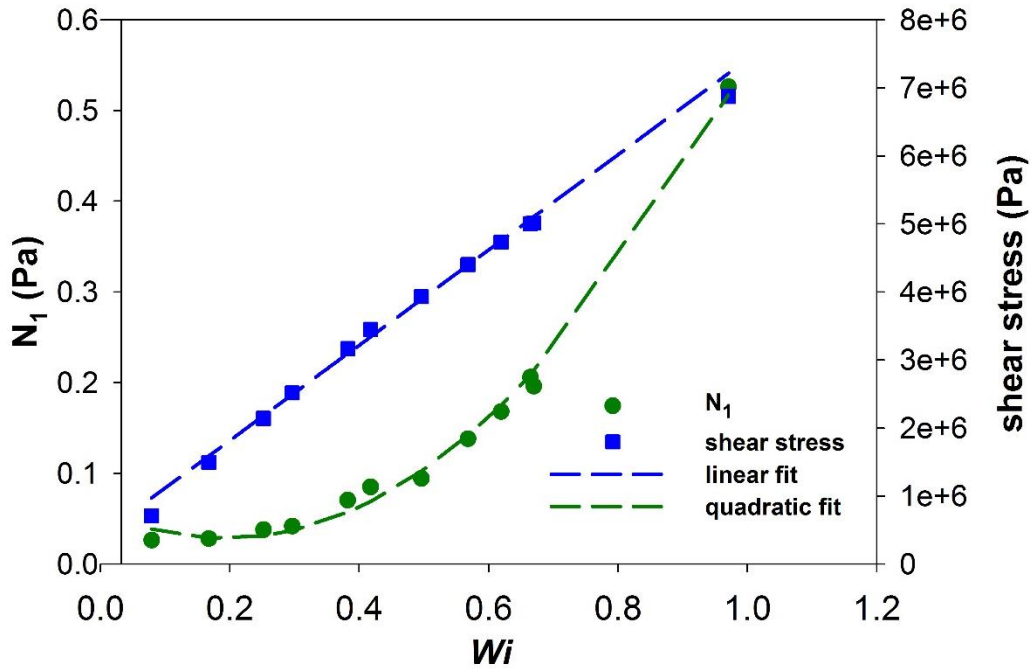


Figure 4.9: Shear stress and Normal stress as a function of Wi for $Wi < 1$. Shear stress scales linearly and N_1 scales quadratically. The dotted lines are the corresponding curve fit.

Plots of shear stress as a function of apparent shear rates from a simulation of $R = 0.1$ and $\varphi_p = 0.002$ are shown in Fig. 4.7. Over the range of shear rates studied, the shear stress is a single valued function of the shear strain, which is further justified by a uniform velocity profile at different shear rates (Fig. 4.8). This clearly illustrates that shear banding instabilities are absent in

our simulations. Shear banding is a commonly observed flow-instability which has been observed in several systems including WLMs^{66, 67, 133, 134}, highly entangled polymers^{135, 136}, associative polymer networks^{137, 138}, and both hard¹³⁹ and soft¹⁴⁰ colloidal suspensions.

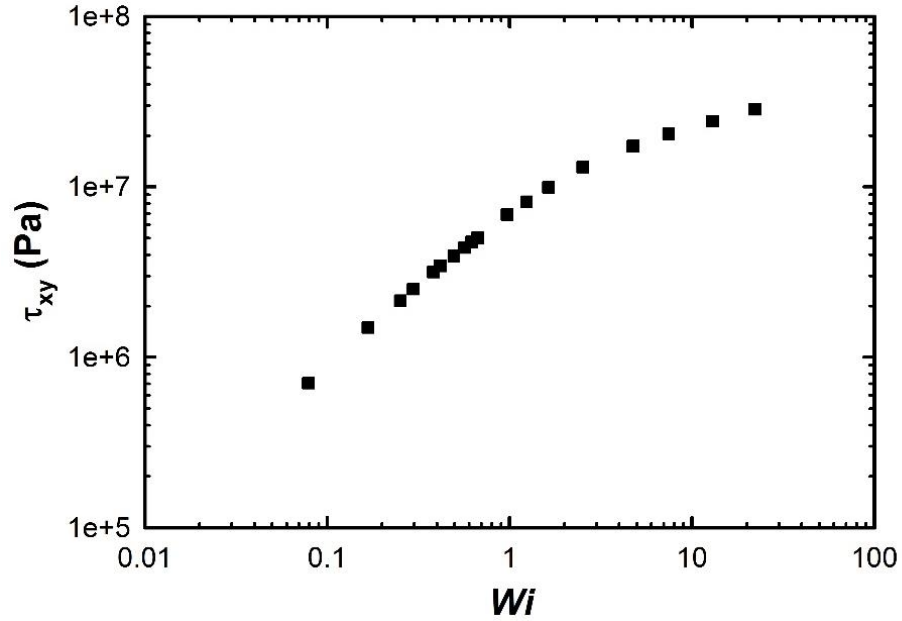


Figure 4.10: Shear stress vs. Wi for $R = 0.1$ and $\varphi_p = 0.002$.

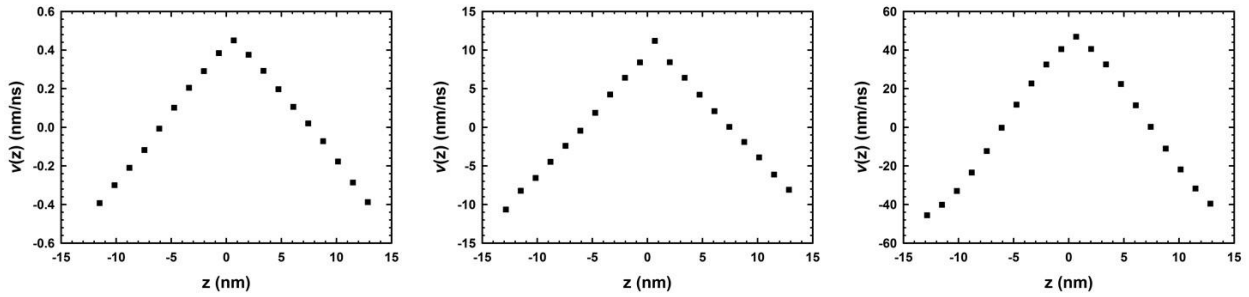


Figure 4.11: Velocity profile at three different shear rates (**Left to right**) $Wi = 0.25$, $Wi = 4.76$, and $Wi = 22.1$.

Shear banding can be considered as an inhomogeneity of the local shear rate of a material in shear flow. In other words, it is the separation of the flow field into two fluid layers, one having a high local shear rate and the other with a low local shear rate. It is also associated with other rheological phenomena of complex fluids such as shear-induced phase separation, wall slip etc. In our simulations, we do not observe shear banding behavior for micelle-NP solutions. Therefore, we can estimate the shear viscosity (η) over the entire range of shear rates simply as:

$$\eta = \frac{\tau_{xz}}{\dot{\gamma}} \quad (4-9)$$

where σ is the shear stress and $\dot{\gamma}$ is the shear rate.

Fig. 4.6 shows that the shear stress in the fluid increases linearly with the shear rate for small deformation and increases non-linearly above a critical shear rates, $\dot{\gamma}_c$. The former linear regime is a signature of Newtonian behavior while the latter is a direct evidence of the non-Newtonian behavior. This transition occurs approximately at $Wi \approx 1$ and is a characteristic of systems consisting of NPs suspended in viscoelastic media^{141, 142}. Such a shear thinning behavior has been attributed in the literature to the alignment of micelles in the flow direction which we will discuss in detail in the following sections¹⁴³.

For less than 1 vol. % nanoparticles, the addition of NPs does not substantially affect the shear viscosity of the solution (Fig. 4.8). This is because, at these volume fractions, the system consists of only 1-3 NPs which is not enough to cause apparent changes in the average length or entanglement density of the micellar solution. However, beyond 1-2 vol. % sufficient number of

NPs are present in the system to cause effective lengthening of micelles and increase in network density. It is also clear that the increase in φ_p shifts the critical shear rate for the onset of non-Newtonian behavior to lower shear rates. This is consistent with experimental observations and as pointed out by Giessle and coworkers¹⁴⁴, this could be because of the presence of solid particles in solution as a result of which the average shear rate of the micelle phase has to be greater than the bulk shear rate of the micelle-NP solution.

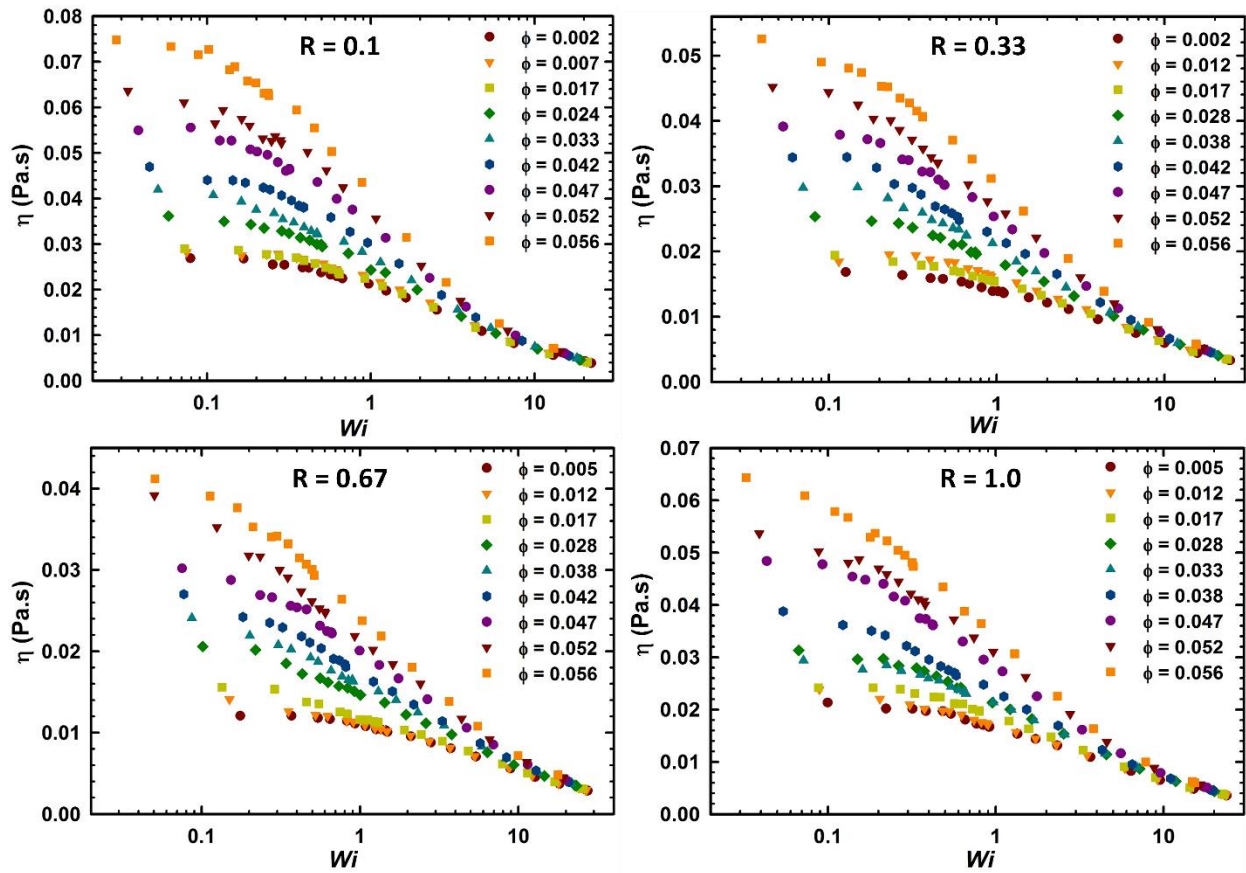


Figure 4.12: Shear viscosity as a function of shear rate for various salt and NP concentrations (a) $R = 0.1$, (b) $R = 0.33$, (c) $R = 0.67$, and (d) $R = 1.0$.

In the range of shear rates accessible through RNEMD simulations, it is possible to observe a small Newtonian regime at lower volume fraction of NPs whereas for systems where $\varphi_p > 4\%$ it is not possible to access critical shear rates that indicate the onset of shear thinning. At moderate shear rates, shear thinning in WLM-NP solutions is initiated by the shear-induced flow-alignment and tumbling dynamics of WLMs and micelle-NP junctions in solution. At higher shear rates, the micelle-NP junctions are ripped apart by the flow and the viscosity converges to the solvent viscosity for all solutions. We characterize the flow-alignment in our simulations using a nematic order parameter. The orientational order is described by a second rank ordering tensor which is defined as,

$$S_{\alpha\beta} = \frac{1}{N_m} \sum_{i=1}^{N_m} \frac{3}{2} \hat{u}_{i\alpha} \hat{u}_{i\beta} - \frac{1}{2} \delta_{\alpha\beta} \quad (4-10)$$

where \hat{u} is a unit vector associated with each micelle and N_m is the total number of micelles in the system. The NPs are not considered in the calculation of nematic order because they are spherical. Typically, in isotropic systems, we would expect the nematic order $\langle S \rangle = 0$. However, this is not possible in MD simulations due to finite size effects. Our simulations consist of $\sim O(10)$ micelles and at these length scales it is reasonable to assume that the system is isotropic for $\langle S \rangle < 0.2$.

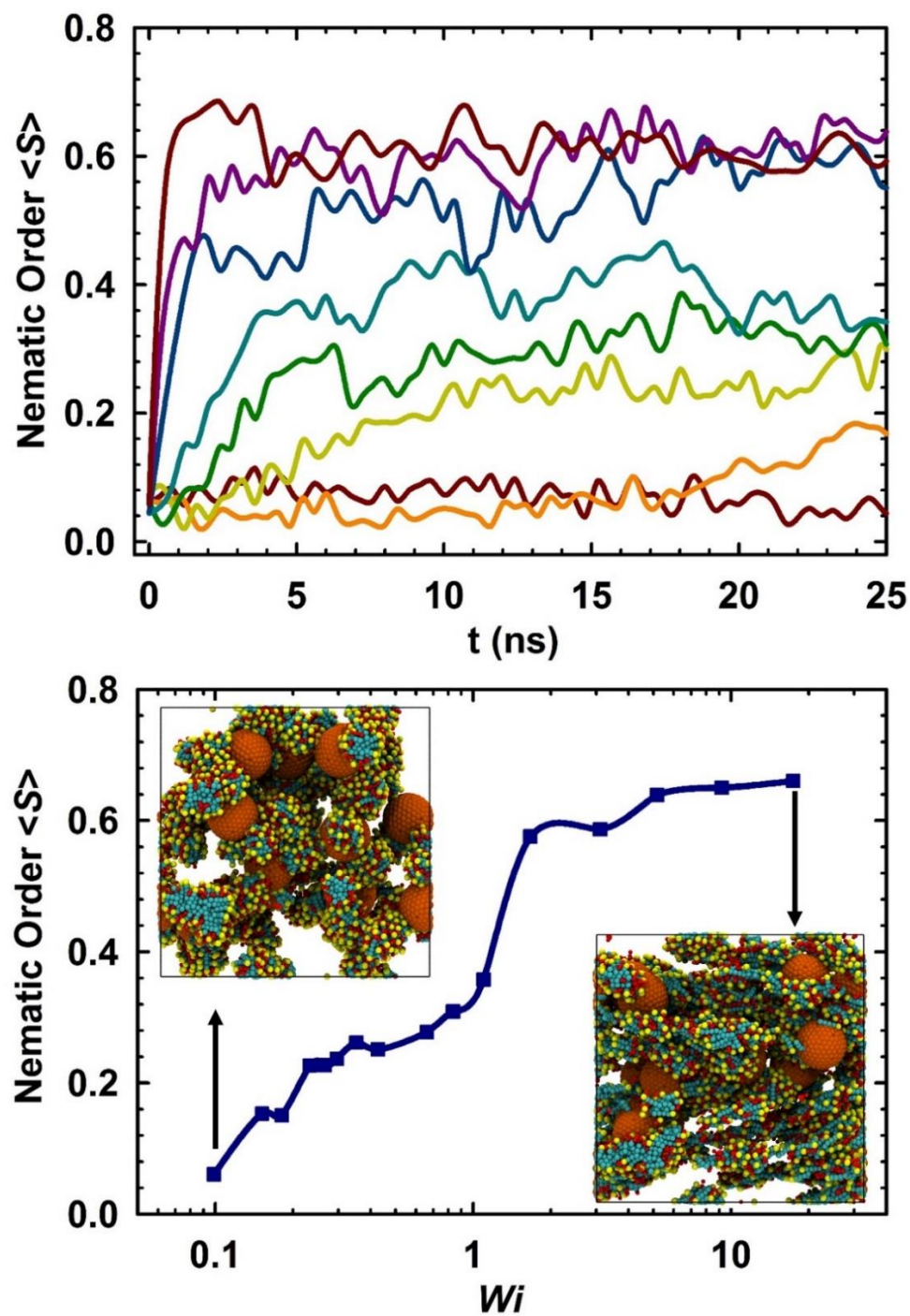


Figure 4.13: (a) Nematic order as a function of time at different shear rates at $C_D = 0.25$ M and $R = 0.33$. (b) Nematic order as a function of Wi . Insets show representative snapshots of the isotropic and nematic state.

Fig. 4.9 shows a plot of the nematic order as a function of time and Wi for the case of $R = 0.33$ and $\varphi_p = 0.03$. The trends observed here are qualitatively similar for all systems that were investigated in this study. Beyond a critical shear rate, we observe that flow induces micellar alignment which is characterized by a gradual increase in the nematic order. This effect becomes significant at $Wi > 1$. Beyond $Wi = 1$, the micelle-NP network is disrupted by the shear flow leading to breakage of micelle-NP junctions and therefore an increase in the number of micelles in solution. Therefore, more micelles undergo flow-alignment and resultantly there is a significant increase in the nematic order. This behavior occurs at all values of R and φ_p .

We further characterized the rheological properties the solution by calculating normal stress differences N_1 and N_2 which are the primary elastic properties of a viscoelastic solution. Fig. 4.10 shows a plot of N_1 as a function of (a) time and (b) Wi for $R = 0.1$ and $\varphi_p = 0.002$. The non-linear behavior appearing in the stress vs. strain relation or the viscosity is also manifested in the normal differences plots. At low shear rates, in the diffusive limit, the system remains fairly isotropic and N_1 tends to zero i.e., the system is Newtonian. However, beyond the critical shear rate, flow-induced ordering results in a sharp increase in N_1 . We observe that N_1 increases linearly with Wi on a semi logarithmic scale. This is again consistent with experimental observations for a canonical surfactant solution (CPyCl-NaSal) which differs only in the length of the hydrocarbon chain of surfactant as compared to the one used in this paper¹⁴⁴. Similarly, the second normal stress difference N_2 is zero in the regime I, and it increases linearly on the semi logarithmic scale in the non-Newtonian regime. It is interesting to note that N_2 has the same sign as N_1 and is smaller by a factor of 2.

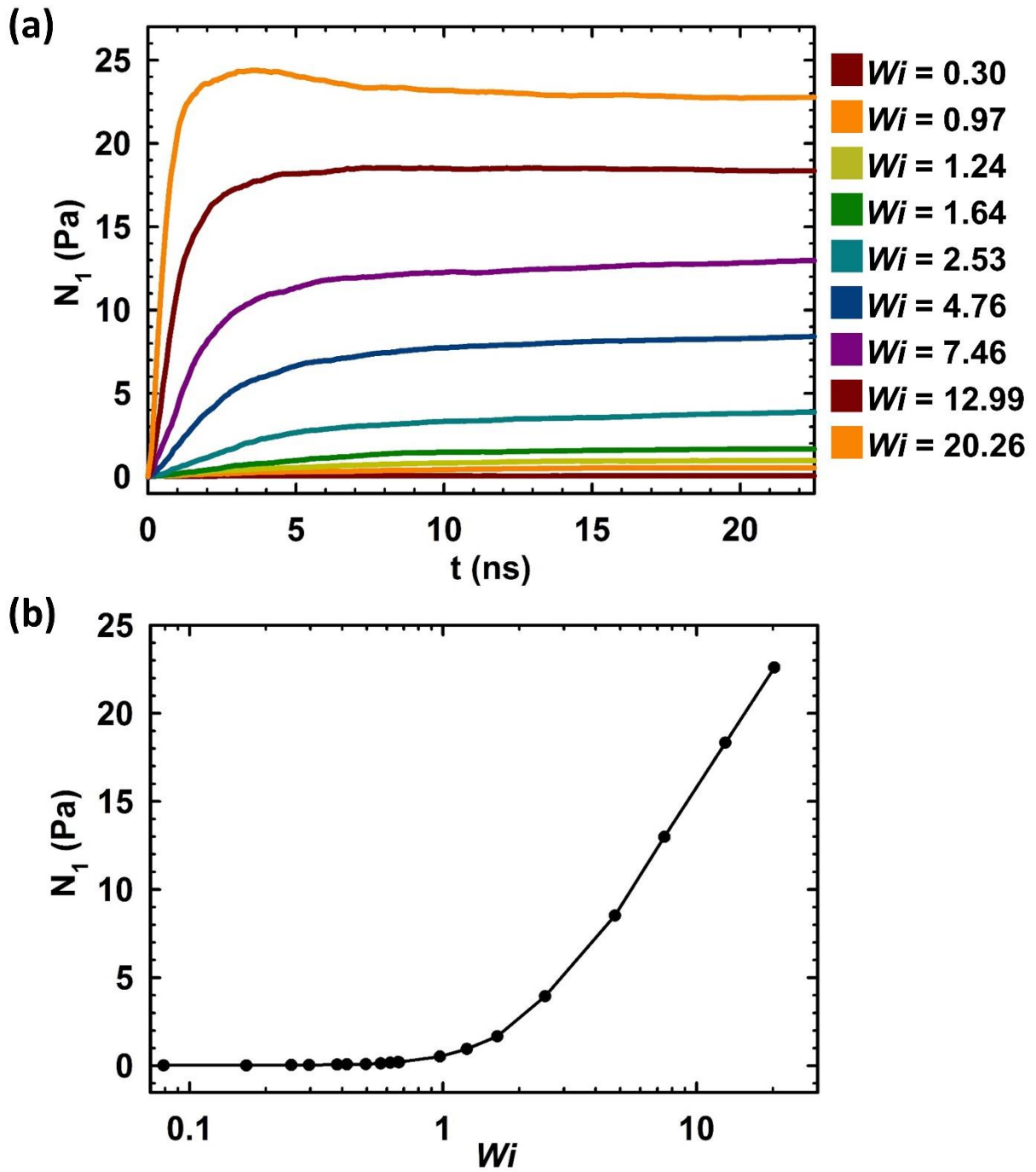


Figure 4.14: First normal stress difference N_1 vs (a) time at different shear rates and (b) Wi .

4.4. Conclusions

We have investigated the microstructure and rheology of solutions containing cationic surfactant micelles and negatively charged spherical nanoparticles in the presence of hydrotropic sodium salicylate salt using coarse-grained MD simulations. Our simulations were performed under conditions of explicit hydrodynamic interactions and long-ranged electrostatic interactions. Addition of NPs to WLM solutions resulted in the formation of electrostatically stabilized NP-micelle junctions. The formation of such junctions produced a linear increase in the solution viscosity due to effective lengthening of micellar structures. At $R = 0.1$, the system consists of nonentangled wormlike aggregates. At low φ_p , the addition of NPs to this solution resulted in effective lengthening of structures due to the formation of physically cross-linked micelle-NP clusters. At higher φ_p the presence of several micelle-NP junctions resulted in the formation of entanglements in an otherwise nonentangled system. At $R = 1$, the equilibrium structure of the micellar solution already consists of several branches and the increase in viscosity with increase in φ_p can be rationalized based on two simultaneous effects: (i) effective lengthening of micelles and (ii) decrease in number of micellar branch points. In NP-micelle solutions, micellar branches were replaced by more rigid NP-mediated branch points which are physically different from micellar branches and do not undergo the sliding mechanism. These observations are in excellent agreement with experimental predictions by Helgeson et al. We also observed a non-monotonic dependence of solution viscosity on R . This can be rationalized using the above-mentioned branching arguments and is discussed in detail in our previous work on micelle solutions in the absence of NPs.

Non-equilibrium MD simulations spanning several decades were performed, using the Muller-Plathe algorithm, to explore the non-Newtonian rheological behavior of micelle-NP solutions. At low φ_p , we observed a small Newtonian regime followed by the onset of shear thinning. We observed shear thinning for all systems across the entire range of salt concentrations and NP volume fractions that were investigated in this study. The critical shear rate for the onset of shear thinning was found to decrease with increasing volume fraction. This is again consistent with experimental observations. Shear thinning was also accompanied by flow-alignment and collective advection of micelle-NP networks. Flow-induced anisotropy was quantitatively captured by calculating a nematic order parameter which clearly shows a transition from isotropic (diffusive) to nematic (flow-aligned) state. The first normal stress difference, N_1 , was calculated from MD simulations and was found to be positive and increases with increase in Wi .

It would be interesting to look at the effects of NP size, shape and surface charge on the microstructure and rheology of such solutions. Another interesting study could be the effect of changing the NP surface chemistry, for e.g., making it completely uncharged and hydrophobic. We have previously shown that both surface charge and surface chemistry have a significant effect on the nature of the self-assembly in micelle-NP solutions. The impact and consequences of these parameters on the rheology of micelle-NP solutions could potentially be of great interest and importance and is the subject of ongoing investigation. A thorough understanding of the structure, dynamics and rheology of such systems can prove to be extremely useful especially in applications where NPs are added to viscoelastic media to provide specific functionality such as in hydrofracking fluids, consumer products and plasmonic nanogels.

Chapter 5

Influence of salt type and concentration on the morphology of surfactant micelles

5.1. Introduction

It is well established that, above the critical micelle concentration (CMC), amphiphilic surfactant molecules tend to self-assemble into supramolecular nanostructures which are referred to as micelles. The driving force for micelle formation is the noncovalent interactions between the tail groups and the head groups of the surfactants and the solvent. These supramolecular structures can include various morphologies ranging from simple spheres and cylinders to wormlike structures and bilayers. Self-assembly in ionic surfactants, such as the one studied in this thesis, are extremely sensitive to the presence of counterions in solution. Several studies have shown that the mixing of ionic surfactants with inorganic or organic salts such as sodium chloride (NaCl), sodium nitrate (NaNO₃), potassium bromide (KBr), sodium salicylate (NaSal) and 3-hydroxy-naphthalene-2-carboxylate (SHNC) results in the screening of electrostatic repulsion between the surfactant head groups due to the presence of oppositely charged counterions. This can consequently change the micelle packing parameter (defined in chapter 1) by reducing the effective surface area of the head group and promote the formation of longer rodlike micelles.

Organic salts such as NaSal and SHNC are amphiphilic in nature due to the presence of a hydrophobic ring structure (tail group) and a negatively charged hydrophilic head group. While they are incapable of forming micelles in solution they can help to solubilize organic molecules in water and hence are referred to as hydrotropic salts. Several studies of mixtures of cationic

surfactants and anionic hydrotropic salts have shown that such salts can promote the growth of wormlike micelles at much lower salt/surfactant ratios than other inorganic salts. In particular, experiments on solutions of cetyltrimethylammonium chloride (CTAC) and cetyltrimethylammonium bromide (CTAB) indicate that aromatic anions like salicylate (Sal^-) are much more effective in inducing wormlike micelle formation than are simple inorganic anions, such as chloride (Cl^-) and bromide (Br^-). The threshold salt concentration for the appearance of rodlike or threadlike micelles was found to be about 1.18 M for NaCl and 0.06 M for NaBr, but as low as 0.15 mM for NaSal. Different ion binding mechanisms have been suggested to elucidate these phenomena. The halide ions, such as Cl^- or Br^- , are believed to be adsorbed on the surface of the micelles due to weak or moderately weak interactions with the surfactant cations. On the other hand, nuclear magnetic resonance (NMR) experiments and atomistic and coarse-grained (CG) molecular dynamics (MD) simulations suggest that aromatic counterions like Sal⁻ penetrate into the micelle and bind strongly with the surfactant head groups, promoting the micelle shape transition at much lower salt concentrations.

More recently, studies have shown that mixtures of cationic surfactants and SHNC salt are extremely sensitive to conditions such as temperature, ionic strength and flow. Kalur et al.¹⁴⁵ have observed an increase in the zero-shear viscosity with increasing temperatures for systems containing erucyl bis-(hydroxyethyl)methylammonium chloride (EHAC) and SHNC salt. They explained this anomaly from the perspective of a temperature dependent counterion binding efficiency. These solutions have also shown pronounced birefringence phenomena¹⁴⁶. Mishra et al.¹⁴⁷ have outlined the phase behavior of CTAB/SHNC solutions for a fixed CTAB concentration (60 mM) and varying the salt/surfactant ratio. They were able to observe transitions from spherical and rodlike aggregates, followed by a liquid crystalline lamellar phase which then formed a

multilamellar vesicular structure. Further addition of salt resulted in inhibition of micelle growth and reduction in entanglement density. Interestingly, it has been noted that the CTAB/SHNC system behaves very similarly to the CTAB/Sodium dodecyl sulfate (SDS) system¹⁴⁸. SDS is an anionic surfactant and SHNC is also structurally similar, albeit with a shorter tail.

Since cationic surfactant micelles display anomalous viscosity behavior with respect to the concentration of hydrotropic salts in solution¹⁴⁹, it is important to understand the fundamental coupling between the underlying microstructure and the observed rheology. Interestingly, the phase behavior of CTAB/NaSal systems is very different from that of the CTAB/SHNC system although the chemical structure of both salts are very similar. The only difference in their structures is that the SHNC molecule has an additional fused benzene ring or a naphthalene ring. Hydrogen Nuclear Magnetic Resonance (HNMR) measurements suggest that due to the closer proximity between the carboxyl and hydroxyl groups in SHNC molecules, they form stronger cation- π and π - π interaction bonds which adversely affect micelle size and shape¹⁵⁰. Therefore, it is safe to hypothesize that the unique phase behavior of SHNC-cationic surfactant solutions is a result of the naphthalene structure as well as the strong hydrophobicity of the HNC⁻ ion. However, till date, there are no molecular explorations of the phase behavior of such systems. The next couple of paragraphs details several attempts to model the effect of salt/counterions on the self-assembly and rheology of micelle solutions.

Maillet et al.¹⁵¹ performed short (~3 ns) atomistic MD simulations of preassembled spherical and cylindrical micelles of n-nonyltrimethylammonium chloride (C₉TAC) and erucyl bis[2-hydroxyethyl]methylammonium chloride (EMAC). The cylindrical micelles were shown to be stabilized with sodium salicylate (NaSal), while at high concentrations of sodium chloride (NaCl) the cylindrical micelle broke into smaller cylindrical fragments. In a notable work by

Marrink et al.¹⁵², atomistic MD simulations of spontaneous formation of micelles of dodecylphosphocholine (DPC) surfactant molecules in the absence of salt were carried out. Formation of a long threadlike micelle was preferred through the periodic boundaries when the size of the surfactant aggregate was comparable to the size of the simulation box. It was pointed out that a small simulation box induces artifacts in the dynamics of micellar aggregate formation due to spatial correlations or long hydrophobic interactions at the periodic boundaries. Piotrovskaya et al.¹⁵³ analyzed the penetration of different additives such as acetone, 2-propanol, and sodium benzoate into the threadlike micelles of CTAC to estimate their effects on the stability of structures. Wang and Larson²⁰ used atomistic MD simulations to study the stability of an infinitely long threadlike micelle of CTAC in the presence of sodium salicylate and sodium chloride salts. The effect of different salts on the kinetics of shape fluctuations and transitions was estimated using relatively long (~10 ns) simulations. In a recent work, the structural properties of both spontaneously formed and preassembled micelles of nonionic dimethyldodecylamine-N-oxide (DDAO) upon addition of ethyl butyrate-like oil molecules were studied¹⁵⁴. The oil molecules induced a near-spherical shape in DDAO micelles which were otherwise somewhat elongated.

Lattice models with Monte Carlo simulations have been developed to study the phase behavior of surfactants and determine their critical micelle concentrations^{155, 156, 157}. Further, CG models of dimer surfactants represented by two types of particles (head and tail) with Lennard-Jones interactions have been utilized to predict the structural phase behavior and dynamical equilibrium of micelles¹⁵⁸. Implicit solvation has been widely used in both atomistic and CG systems to improve the sampling of micellar structures for longer time and length scales^{159, 160}. Finitely extensible nonlinear elastic (FENE) potentials used with dissipative particle dynamics or even molecular dynamics have been explored for large-scale simulations of micellar self-

assemblies to study rheological properties of wormlike micelles^{161, 162}. While these studies are capable of making qualitative predictions of the phase behavior and rheological properties of micelles, they do not account for the effect of the chemical specificity of the intermolecular interactions among the surfactant, salt, and water molecules. Recently, Sangwai et al.^{19, 44} used a MARTINI based CG model to show that the sphere-to-rod transition and the coalescence of two spherical micelles to form a single rod-like micelle was better facilitated by the presence of hydrotropic salts such as NaSal as compared to NaCl salt.

In this chapter, we present results from equilibrium CGMD simulations of CTAC surfactants with three different salt types, namely, NaCl, NaSal and SHNC, at a fixed surfactant concentration and over a wide range of salt concentrations. The dynamics of micelle formation, range of observed micellar structures and the zero-shear viscosity of these solutions are presented. Finally, outlines for future work in this topic are discussed.

5.2. Simulation Methods

5.2.1. Effect of Salt Concentration on Micelle Growth Kinetics

All simulations were performed using the GROMACS MD simulation package (Version 4.6.5). In order to study the effect of salt concentration on the micelle growth kinetics, the model system that we chose is the CTAC/NaSal system. The CG models used in this study are described in detail in Chapter 2. We fixed the surfactant concentration at $C_D = 0.14$ M and varied the salt concentration such that the salt/surfactant ratio, R , ranged between 0 and 2. The size of the simulation box was ~ 27 nm on each side. Therefore, the system consisted of 1500 CTAC surfactants, ~ 130000 water molecules out of which 10% were replaced by the antifreeze CG water

molecule in order to prevent freezing at room temperature. We performed equilibrium MD simulations for $R = 0.1$, $R = 0.3$, $R = 0.6$, $R = 0.9$, $R = 1.2$, $R = 1.6$ and $R = 1.9$. For each value of R , we performed 10 simulations, each with a different random initial configuration. This was done in order to obtain sufficient statistics and error bars because micelle growth kinetics can depend heavily on the initial configuration of molecules in the system. Finally, an equivalent amount of Na^+ and Cl^- ions were added to the system to maintain electrical charge neutrality. The system was then energy minimized using the steepest descent method followed by an NPT simulation for 50 ns with a time step of 20 fs at a temperature of 300 K and a pressure of 1 atm. Temperature coupling was done using the velocity rescaling method and pressure coupling was done using the Berendsen barostat. The neighbor list cut off was set at 1.4 nm and short range Lennard-Jones and Coulombic interactions were cut off at 1.2 nm using the potential-shift-verlet scheme in GROMACS. Long ranged electrostatic interactions were evaluated using the particle mesh Ewald (PME) method. Periodic boundary conditions were applied in all three orthogonal directions. Finally, a production run of 300 ns was performed for each of the simulations. Therefore, the sum total of all the simulations performed for this study adds up to 21 μs .

5.2.2. Effect of Salt Type on Micelle Growth

We performed a second set of simulations to study the effect of salt type on the growth kinetics and zero shear viscosity of CTAC surfactants. Three different salts, namely, NaCl, NaSal and SHNC, were used in this study. The data for the CTAC/NaSal system was obtained from a recently published work by Dhakal and Sureshkumar¹⁷ and we performed CG MD simulations of CTAC/NaCl and CTAC/SHNC systems at the same conditions as described in their work. This

will enable us to make a comparison of the microstructures and equilibrium rheology of such systems under varying salt concentrations and types. For all three salt types, the surfactant concentration was fixed at ~ 0.34 M and the salt/surfactant ratio, R , was varied between 0 and 3. Simulations consisted of 4000 CTAC surfactants in a cubic box of side ~ 27 nm. Equilibration of the system was performed for ~ 50 ns and production runs sampled $t > 400$ ns. The number of micelles as well as the average size of the clusters were tracked as a function of time.

The zero shear viscosity for each of the systems was calculated using a time decomposition method proposed by Zhang et al.¹⁶³ The method uses the traditional Green-Kubo formalism but makes use of several short independent trajectories as compared to the single long trajectory that is used more commonly for such calculations. For each short trajectory, the shear viscosity is calculated based on the Green-Kubo relation (defined in eq. 4.1). The averaged running integral, $\langle \eta(t) \rangle$, and the standard deviation is calculated as a function of time and fitted to a double exponential function of the form

$$\eta(t) = A\alpha\tau_1(1 - e^{-t/\tau_1}) + A(1 - \alpha)\tau_2(1 - e^{-t/\tau_2}) \quad (5-1)$$

where A , α , τ_1 , τ_2 are fitting parameters. The advantage of using this method is that while typical Green-Kubo integrals require integration over infinite time, here we can use a finite cutoff time, t_{cut} , which is determined by using the relative values of the running integral and the standard deviation. Zhang et al.¹⁶³ suggest that a good choice for t_{cut} is when the standard deviation, $\sigma(t)$ is about 40% of the running integral, $\langle \eta(t) \rangle$.

5.3. Results and Discussion

5.3.1. Micelle Growth Kinetics: Effect of Salt Concentration

The kinetics of micelle formation and growth depends factors such as the surfactant concentration, salt concentration, temperature, pressure, and pH and has been studied by several researchers from an experimental as well as theoretical point of view. Understanding the effect of factors such as temperature and salt concentration on the rate of micelle formation might be useful in terms of developing standard protocols for molecular simulations of such systems. For example, knowledge of the timescales associated with micelle formation, growth, scission and recombination can provide valuable information not only from a scientific understanding perspective, but also regarding the timescales necessary for sufficient sampling of thermodynamic states in such systems using molecular dynamics simulations. Micelle kinetics is typically governed by a fast process which is related to the average time for surfactant exchange between micelles (\sim ns), and a slower process related to micelle breakage and end cap formation (\sim ms)¹⁶⁴. The longer the timescale of such processes, the more stable is the micelle structure. Commercial surfactants such as sodium dodecyl sulfate (SDS) have surfactant exchange times on the order of microseconds which is an indication of their remarkable stability¹⁶⁵. Experimental techniques such as temperature jump, ultrasonic absorption, EPR, or shock tube method have been used to detect the surfactant exchange time in micelle solutions^{166, 167}.

In our simulations of CTAC/NaSal systems, we track the number of micelles, N_m , in solution as a function of time for $R = 0.1$, $R = 0.3$, $R = 0.6$, $R = 0.9$, $R = 1.2$, $R = 1.6$ and $R = 1.9$. For all simulations, we observe that N_m follows a power law scaling with time given by:

$$N_m \sim N_m^0 t^{-\alpha(R)} \quad (5-2)$$

where N_m^0 is the number of micelles at $t = 0$ and α is the power law exponent which is a function of R . Figure 5.1 shows the number of micelles as a function of time for $R = 0.1$ and $R = 0.9$ which clearly show a power law dependence with time and Fig. 5.2 shows a plot of the power law exponent $\alpha(R)$ as a function of R .

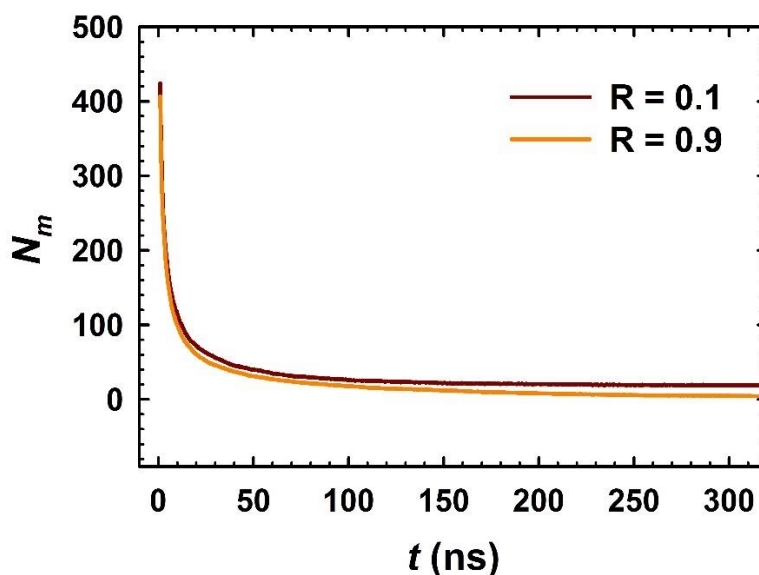


Figure 5.15: Number of micelles N_m as a function of time for $R = 0.1$ and $R = 0.9$. Plots of N_m at other values of (R) are not shown for clarity.

The observed power law in the growth kinetics of surfactant micelles has been reported previously and suggests that there are at least two stages in the kinetics of micelle formation. The initial stage is rapid and is characterized by nucleation and coalescence of surfactant molecules and smaller

micellar aggregates. As micelles become longer and fewer in number, there is a dramatic reduction in the growth rate due to the longer timescales associated with micelle fusion and/or scission.

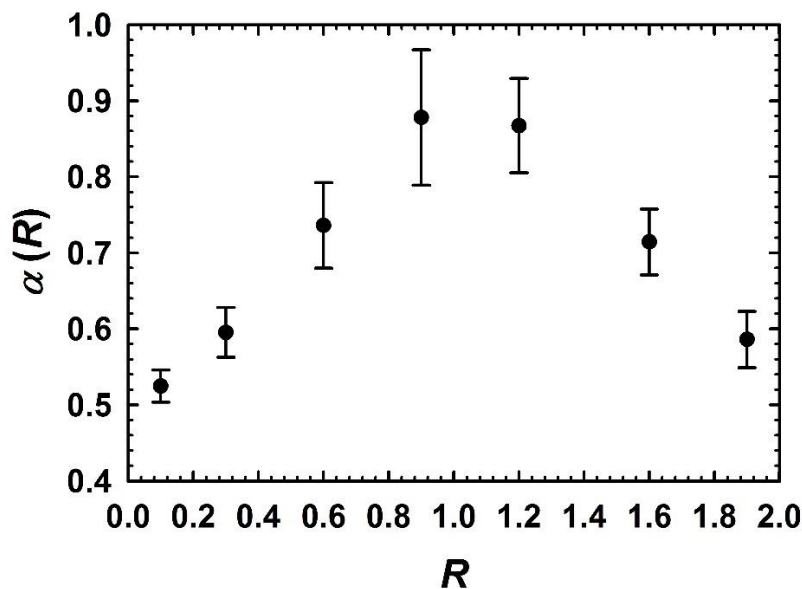


Figure 5.16: Dependence of the power law exponent $\alpha(R)$ on the salt/surfactant ratio, R . Error bars indicate data averaged over 10 different simulations for each data point.

Figure 5.2 suggests that the power law exponent $\alpha(R)$ increases with increase in R until $R = 1$, after which it decreases again. A higher value of α means that the rate of micelle formation is faster and a lower value suggests that the growth rate is slower. The observed behavior can be rationalized by the fact that initially, at $R = 0.1$, due to the lack of sufficient electrostatic screening, cationic head groups repel each other and reduce the growth rate of micelles in solution. As R is increased, the growth kinetics in these micelle solutions gradually increases until $R=1$. At this point, equimolar amounts of salt and surfactant are present in the system leading to efficient

screening of the electrostatic repulsion which in turn enhances the growth kinetics. Beyond this point, the excess salt in the system probably results in an inversion of the micellar charge which in turn reduces the growth kinetics¹⁷.

5.3.2. Zero-Shear Viscosity

The zero-shear viscosity of CTAC/NaSal systems and CTAC/NaCl systems has been investigated extensively using rheological characterizations, cryo-TEM imaging¹⁶⁸, mesoscopic theories¹⁶⁹ and more recently, using CG MD simulations. CG MD simulations clearly show that the anomalous double peak in the zero-shear viscosity of CTAC/NaSal systems is closely related to the molecular structure of the fluid and that the interplay between the various non-bonded interactions in the system results in a wide variety of micelle morphologies¹⁷. At low R, the micelles are typically spheres or short rodlike aggregates. As R increases, there is a rapid increase in the size of these rodlike aggregates which results in the formation of wormlike micelles. The rapid increase in micelle length directly corresponds to the sharp increase in the solution viscosity. However, beyond a certain salt concentration ($R=0.8$), the onset of branching in micellar systems gives rise to a faster stress relaxation mechanism by which micelle branches can slide along the contour of the micelle. This results in a rapid decrease in the viscosity. On further addition of salt, a second peak appears due to the formation of a rigid elastic network which is a consequence of coalescence of branched micelles. Finally, the excess counterions in solution tend to disintegrate the network due to electrostatic attraction of cationic surfactant molecules.

Here we study the zero-shear viscosity of CTAC/SHNC system and attempt to compare it with the observations for CTAC/NaSal system. Figure. 5.3 shows a plot of the zero-shear viscosity

of CTAC/SHNC system as a function of R . Over the range of R studied in this work, we do not observe a double peak in the zero-shear viscosity for CTAC/SHNC systems.

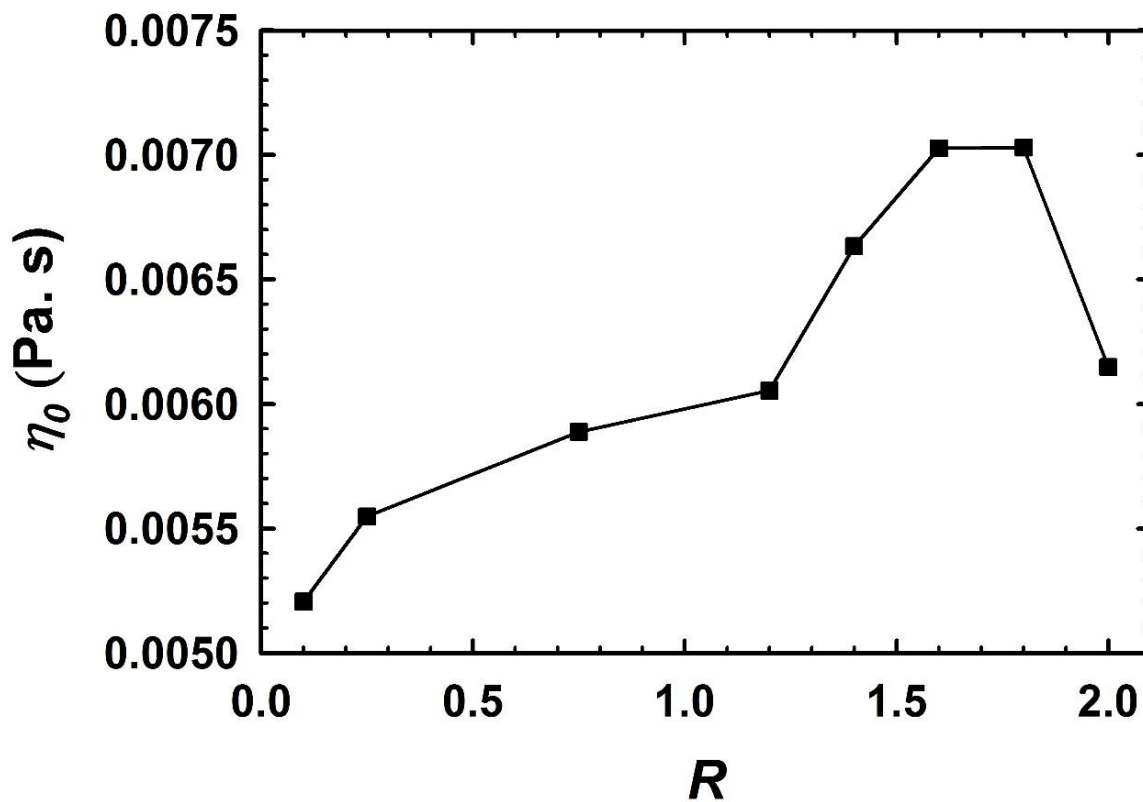


Figure 5.17: Zero-shear viscosity (η_0) for CTAC/SHNC system as a function of R showing a 35% increase in η_0 with the addition of salt. Line is just a guide to the eye.

At $R = 0.1$, the system consisted of linear, rodlike and semiflexible micelles. At $R = 0.25$, although we observe one instance of micellar branching, the system predominantly consists of

longer wormlike micelles which results in a slight increase in the viscosity. For $R > 0.5$, the viscosity increases more sharply until $R > 1.5$ beyond which there is a decrease in η_0 . We find that the CTAC/SHNC system exhibits a very different phase behavior as compared to the CTAC/NaSal system. For $0.5 > R > 1.5$ surfactants tend to self-assemble into semi-lamellar structures which may or may not be connected by wormlike micelles. In some cases, even small vesicular structures were observed. This is primarily due to the naphthalene ring of SHNC which strongly binds to the micellar surface and changes the effective head group area of the surfactants thereby increasing the geometric packing parameter to values close to 1. Such semi-lamellar structures have not been observed before and it may be interesting to explore such structures in more detail in the future. Representative snapshots of the largest aggregate in the system are shown in Fig. 5.4 to illustrate the above argument.

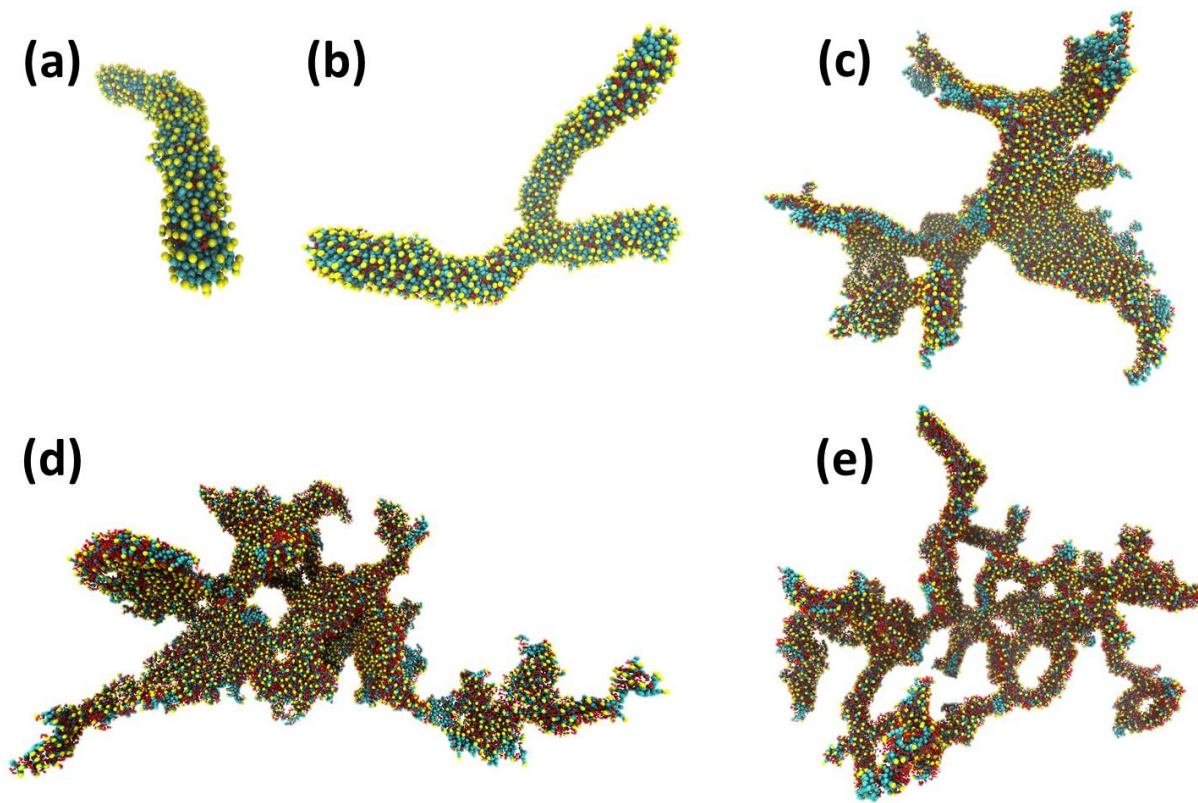


Figure 5.18: Snapshots of the largest self-assembled structure for $C_D = 0.34$ M and (a) $R = 0.1$, (b) $R = 0.25$, (c) $R = 1.2$, (d) $R = 1.6$ and (e) $R = 2.0$. Coloring scheme is as follows: CTA+ tail group (cyan), head group (yellow) and SHNC salt (red).

5.4. Conclusions

In this chapter, we studied the effect of salt concentration and type on the kinetics of micelle formation. The number of micelles in solution was found to have a power law relationship with time suggesting that micelle formation is a two-step process. The first step is rapid and is characterized by nucleation and coalescence of surfactant monomers as well as smaller micellar

aggregates (less than aggregation number of CTAC). The second step is much slower and is associated with micelle breakage and recombination which occurs over longer timescales. The power law exponent α was found to be strongly dependent on the salt/surfactant ratio, R . It was found that the growth rate of micelles in solution reaches a peak at equimolar concentrations of surfactant and salt. This is consistent with current literature¹⁹ which suggests that at $R=1$, sufficient salt is present in the system to efficiently screen the electrostatic repulsion between the head groups which results in coalescence as well as faster dynamics. Equilibrium viscosity of CTAC/SHNC system was calculated using a time decomposition method which is based on the traditional Green-Kubo formalism. Unlike CTAC/NaSal systems, CTAC/SHNC systems do not display a double peak in the zero-shear viscosity, η_0 . Initially, η_0 increases with increase in R but for $R > 1.8$, sufficient salt is present in the system to force a transition from sheet-like structures to entangled micelle networks which leads to a reduction in the solution viscosity. We also report new observations of semi-lamellar sheet-like micelle structures in CTAC/SHNC systems for $0.5 < R < 1.5$. The origin of such structures and their effect on the macroscopic properties of the fluid are potentially interesting topics of study. A thorough understanding of the CTAC/SHNC system over a wide range of physicochemical conditions will require synergistic efforts from experiments, theory and molecular simulations. We hope that the results presented here will motivate further investigations of such systems using experimental techniques such as high-resolution atomic force microscopy, cryo-TEM measurements and so on.

Chapter 6

Summary and Future Work

6.1. Introduction

Surfactant micelles are commonly used in several industrial and consumer products². Despite decades of research, experiments have not been able to provide sufficient spatial and temporal resolution to study the structure, dynamics, self-assembly and rheology of surfactant micelles at the molecular level. Understanding the coupling between the microstructure and the macroscopic properties in such systems is a key towards manufacturing precisely architected micellar fluids for tailored applications. Such applications include targeted drug delivery, detergency¹⁷⁰, enhanced oil-recovery³, turbulent drag reduction⁵ and creating soft templates for nanoparticle synthesis⁹⁶. Micellar fluids are intrinsically multiscale in nature and investigations of equilibrium and non-equilibrium properties of such solutions would require techniques that are equally multi-scaled. Further, the microstructure and phase behavior of micellar fluids is strongly dependent on the surfactant concentration, chemical environment, i.e., salt concentration and type, pH, temperature, type of solvent, flow conditions and other external stimuli such as electrical and optical fields. Efforts have been made to study the effect of each of the above mentioned properties through several material characterization techniques including rheology, small-angle X-ray scattering, small-angle neutron scattering, titration calorimetry, and nuclear magnetic resonance (NMR). Theoretical investigations of such systems have focused on kinetics of micelle formation, identifying timescales associated with surfactant dissociation and recombination, length distributions, a priori predictions of micelle morphology and phase behavior, and several equilibrium and non-equilibrium phenomena.

More recently, rapid advancements in the area of distributed computing and the development of efficient algorithms that can utilize the parallel computing environment have made it possible for us to investigate polymeric and micellar systems using multiscale modeling methods. Many molecular dynamics (MD) simulation studies have attempted to investigate the effects of different salts on the sphere to rod transition of micelles. Maillet et al.¹⁵¹ performed short (~3 ns) atomistic MD simulations of preassembled spherical and cylindrical micelles of n-nonyltrimethylammonium chloride (C₉TAC) and erucyl bis[2-hydroxyethyl]methylammonium chloride (EMAC). Marrink et al.¹⁵² performed atomistic MD simulations of spontaneous formation of micelles of dodecylphosphocholine (DPC) surfactant molecules in the absence of salt and reported that the formation of a long threadlike micelle was preferred through the periodic boundaries when the size of the surfactant aggregate was comparable to the size of the simulation box. Piotrovskaya et al.¹⁵³ analyzed the penetration of different additives such as acetone, 2-propanol, and sodium benzoate into the threadlike micelles of CTAC to estimate their effects on the stability of structures. Wang and Larson²⁰ used atomistic MD simulations to study the stability of an infinitely long threadlike micelle of CTAC in the presence of sodium salicylate and sodium chloride salts. The effect of different salts on the kinetics of shape fluctuations and transitions was estimated using relatively long (~10 ns) simulations. In a recent work, the structural properties of both spontaneously formed and preassembled micelles of nonionic dimethyldodecylamine-N-oxide (DDAO) upon addition of oil-like molecules were studied. The oil molecules induced a near-spherical shape in DDAO micelles which were otherwise somewhat elongated.

To overcome the limitations of time and length scales in atomistic MD, different coarse-grained schemes have been used to model surfactant self-assemblies. Continuum-level models can access long timescales and make qualitative and semi-quantitative predictions of steady-state

behavior as well as flow instabilities, such as shear banding, in worm-like micelle solutions. These models attempt to capture macroscopic fields such as shear stress, velocity, viscosity and pressure and neglect molecular details such as structure, self-assembly and configurational dynamics of surfactant micelles in solutions. Stochastic simulations such as Brownian dynamics and dissipative particle dynamics simulations have also been performed on such systems where parameters for the stochastic simulation, such as the persistence length of the micelle, were obtained from short time scale fully atomistic simulations⁷⁰.

Lattice models with Monte Carlo simulations have been developed to study the phase behavior of surfactants and determine their critical micelle concentrations¹⁶². Further, CG models of dimer surfactants represented by two types of particles (head and tail) with Lennard-Jones interactions have been utilized to predict the structural phase behavior and dynamical equilibrium of micelles. Implicit solvation has been widely used in both atomistic and CG systems to improve the sampling of micellar structures for longer time and length scales¹⁶¹. Finitely extensible nonlinear elastic (FENE) potentials used with dissipative particle dynamics or even molecular dynamics have been explored for large-scale simulations of micellar self-assemblies to study rheological properties of wormlike micelles. While these studies are capable of making qualitative predictions of the phase behavior and rheological properties of micelles, they do not account for the effect of the chemical specificity of the intermolecular interactions among the surfactant, salt, and water molecules.

The goals of this thesis were to present a rigorous coarse-grained molecular model for a typical surfactant such as cetyltrimethylammonium chloride (CTAC) and hydrotropic salts such as sodium salicylate (NaSal) and 3-hydroxy naphthalene-2-carboxylate (SHNC), which could account for chemical detail as well as access long timescales. Further, the ability of the CGMD

framework to investigate the structure, dynamics, rheology and self-assembly of surfactant micelles and micelle-nanoparticle solutions at the molecular level has been elucidated. The important results and conclusions have been described in detail in each of the next four sections below. In the final section, we motivate new approaches to study the rheology of these fluids, for e.g. linear viscoelastic behavior, using molecular simulations and provide recommendations for future work in the area.

6.2. Configurational Dynamics and Scission of a Rodlike Micelle

In Chapter 2, the configuration dynamics of a single rodlike cationic surfactant micelle was studied using coarse-grained molecular dynamics (CGMD) simulations. Our simulations included long ranged electrostatic interactions through particle mesh Ewald summations, and solvent polarizability and hydrodynamic interactions through an explicit polarizable water model. Equilibrium properties such as the timescale of rotational diffusion, τ_D , and the orientational relaxation time, τ_R , of the micelle were estimated. While the diffusion timescale was found to be on the order of microseconds, the orientational relaxation was found to be approximately 28.7 ns, which is two orders of magnitude lesser. An appropriate criterion to distinguish between the Brownian (diffusive) regime and the flow-aligned regime was identified as the Weissenberg number which is defined as, $Wi \equiv \dot{\gamma}\tau_R$. CGMD simulations are capable of accurately predicting the stretching and tumbling dynamics of a single rodlike micelle in shear flow. The probability distribution function (PDF) of the in-plane orientational angle, θ , was found to be slightly biased to positive θ values and could be fitted to a shifted Gaussian for $Wi > 1$. The full width at half maximum of the Gaussian follows a power law relation with Wi with an exponent of -0.31. For

$Wi \gg 1$, the tail of the PDF of the out-of-plane angle, φ , was found to scale as φ^{-2} . The tumbling frequency also follows a power law relation with Wi for $Wi > 1$. The power law exponent has been found to approach 0.67 and this is in excellent agreement with predictions for rodlike and semiflexible polymers in shear flow.

A relationship between micelle pair potential energy, Φ , and length, l , was estimated through structure relaxation simulations on flow-aligned, stretched micelles. A linear dependence of Φ on l was found which yielded a micelle stretching force of ≈ 650 kJ/mol/nm. This corresponded to a force of ~ 1 nN per molecule which is similar to van der Waals forces estimated through atomic force microscopy experiments in Gecko feet. Finally, for $Wi \gg 1$, we show that micelle scission occurs due to a mechanism by which flow-induced micelle stretching results in reduced electrostatic screening of micellar head groups which results in micelle breakage. The energy barrier for micelle scission was found to be ~ 2500 - 2700 kJmol⁻¹. Thus, consistent with experimental observations, we conclude that for $Wi \sim O(1)$, flow-alignment can result in shear-induced structure formation and for $Wi \gg 1$, flow-induced micelle scission would result in shear thinning.

6.3. Self-Assembly at the Nanoparticle-Surfactant Interface

The addition of noble metal nanoparticles to wormlike micelle solutions has been shown to provide a robust route to manufacture multicomponent plasmonic nanogels with tunable optical properties and rich rheological behavior. The nanoparticle shape, size and material are all important factors in controlling the wavelength at which light is absorbed or emitted. The light trapping ability of metal nanoparticles is a consequence of localized surface plasmon resonance, a phenomenon by which the free conduction electrons in the particle surface collectively oscillate with the same frequency as that of the incident radiation. While rheological characterizations, cryogenic transmission electron microscopy (cryo-TEM) experiments and small-angle X-ray scattering measurements provide insight into the microstructure of such solutions, the underlying mechanisms of self-assembly between the nanoparticles and micellar aggregates is poorly understood.

In Chapter 3, we have performed CGMD simulations of nanoparticles and surfactants in aqueous solution to uncover the equilibrium structure and self-assembly mechanisms in micelle-nanoparticle solutions. Our simulations indicated that surfactants tend to self-assemble with both hydrophobic and charged, hydrophilic nanoparticle surfaces. In the case of a hydrophobic surface, self-assembly occurred in a tail-on fashion with the surfactants forming a corona-like monolayer around the nanoparticle. Conversely, for a negatively charged particle surface, the cationic head groups of the particle are electrostatically attracted to the nanoparticle surface leaving the tail groups exposed to the water. Since this is energetically unfavorable, a second layer of surfactants was formed with the tail groups of the two layers interdigitated with each other. The kinetics of self-assembly was also discussed. The self-assembly process consisted of two regimes: a rapid adsorption regime followed by a slower regime of surface rearrangement.

These nanoparticle-surfactant complexes further interacted with rodlike micelles in the presence of NaSal salt to form electrostatically stabilized micelle-nanoparticle junctions. Consistent with existing hypothesis, junction formation was shown to occur via an end cap attachment mechanism which results in the micelle losing one end cap and the nanoparticle losing its spherical symmetry. Both these events would result in the rearrangement of surfactants within the nanoparticle-surfactant-micelle composite structure. The dynamics of surfactant exchange was found to have two regimes: a diffusive regime which had a net transfer of surfactants from the micelle to the nanoparticle-surfactant complex followed by a plateau indicating saturation of the particle surface and the existence of a dynamic equilibrium where the average number of surfactants in each structure was constant. The energetics of junction formation was also investigated. Junction formation resulted in a decrease in the pair potential energy of the composite structure by $\sim O(100 k_B T)$. This is much greater than the end cap energy of the micelle which is estimated to be $\sim O(10 k_B T)$. Further, these estimates of the pair potential energy suggest that these fluids are immune to breakage by thermal fluctuations which is consistent with the experimentally observed long shelf life of plasmonic nanogels.

6.4. Rheology of Micelle-Nanoparticle Solutions

Wormlike micelles are widely used in a number of different industrial and consumer products and processes where they come in contact with colloidal species. Still, relatively little is understood regarding the interactions between WLMs and colloids both at equilibrium and, especially, under flow. Limited previous studies have reported a number of often contradictory ways in which colloids affect the rheology of micellar fluids. Some colloids lead to a monotonic

increase in viscosity, whereas for others it is non-monotonic. Some fluids exhibit a transition from Maxwellian to non-Maxwellian linear viscoelasticity with particle addition. Some show the opposite trend, and some maintain Maxwellian behavior throughout. Conversely, the presence of WLMs significantly affects the interactions between, and stability of, colloidal particles. This potentially new class of WLM-mediated colloidal interactions has been relatively unexplored, and the nature of the resulting colloidal phase behavior is poorly understood. In Chapter 3, we uncovered the self-assembly mechanisms in micelle-nanoparticle solutions. In Chapter 4, we performed large-scale equilibrium and non-equilibrium MD simulations to explore the structure and rheology of these solutions.

We first utilized equilibrium simulations to study the influence of salt concentration and surfactant concentration on the zero shear viscosity of wormlike micelle solutions. The surfactant concentration and the nanoparticle diameter were fixed at 0.25 M and 4.5 nm for all our simulations. In the range of salt-to-surfactant ratios, R , and nanoparticle volume fractions, φ_p , studied, we observed the following behavior. Zero shear viscosity, η_o , was found to vary non-monotonically with the salt concentration. Specifically, η_o was found to decrease for $R = 0.33$ and further decrease for $R = 0.67$. On further addition of salt, η_o was found to increase slightly. The decrease in viscosity is attributed to the onset of micelle branching which is known to reduce the solution viscosity. Further addition of salt results in the merger of several branched micelles resulting in the formation of an elastic network which resulted in an increase in the viscosity. Next, we observed that η_o increased linearly with increase in φ_p for all salt concentrations, which is in good agreement with experimental observations. The viscosity increase was closely related to the changes in the microstructure of the fluid due to the presence of the nanoparticles. It was noted that, for $R = 0.1$, the system consisted of rodlike and wormlike micellar aggregates and there were

no instances of branching or entanglements in these systems. However, with increase in φ_p , these micellar aggregates self-assembled with the nanoparticles to form patchy micelle-nanoparticle junctions which resulted in the effective lengthening of the micellar structures. On further increase in φ_p , several nanoparticle-micelle junctions are formed which resulted in the formation of entangled micelle-nanoparticle networks. Thus the addition of nanoparticles to micellar fluids can result in effective lengthening of micelles and also create entanglements in an otherwise non-entangled fluid. Both these phenomena resulted in an increase in η_o . In branched micellar systems, for e.g., $R = 1.0$, apart from the effective lengthening of micelles, the replacement of micellar branch points with nanoparticle-mediated branches was found to result in an increase in η_o .

Next, we performed thousands of non-equilibrium MD (NEMD) simulations to study the rheological behavior of micelle-nanoparticle solutions. We utilized the Muller-Plathe algorithm to perform reverse NEMD simulations and calculated quantities such as the shear rate, shear stress, shear viscosity, orientational order and normal stress differences. Wormlike micelle solutions have been shown to exhibit Newtonian, shear thinning, shear thickening, rheopexy and shear banding behavior. In our simulations we observed a Newtonian regime and a shear thinning regime for all salt concentrations and volume fractions. The onset of shear thinning behavior was shifted to lower shear rates with increasing φ_p , which is due to the presence of solid particles in a fluid medium which results in the apparent shear rate being lesser than the shear rate of the micelle phase. Shear thinning was accompanied by flow-induced isotropic-to-nematic transition in micelle-nanoparticle solutions. We did not observe shear banding instabilities in our simulations as evidenced by the shear stress which remained a single-valued function of the shear rate for all systems. This is possibly due to the presence of the nanoparticles which tend to suppress the orientational order in such solutions. We also calculated the first and second normal stress differences from our

simulations. It was observed that at low shear rates, i.e., $Wi < 1$, the shear stress scales linearly with Wi and the first normal stress difference scales quadratically with Wi . This indicated that wormlike micelle-nanoparticle solutions modeled in this study display behavior that is typical of a simple viscoelastic fluid. For $Wi > 1$, there is a sharp transition to a non-linear regime which suggested that flow is sufficiently strong to align micelles in the direction of the flow and increase orientational order. The increase in orientational order was directly captured by the nematic order parameter. Further, a sharp increase in the normal stress and a sharp decrease in the shear viscosity clearly suggested that flow-induced alignment and micelle scission results in shear thinning behavior. This is again consistent with the results presented for rodlike micelles in Chapter 2.

6.5. Effect of Salt Type and Concentration on Micelle Formation

In chapter 5, we studied the effect of salt concentration and type on the growth kinetics and zero-shear viscosity of CTAC surfactants using CD MD simulations. We demonstrate a two-step micelle formation process: a fast step which is characterized by nucleation and aggregation of monomers and small aggregates, and a slow step which corresponds to micelle recombination and scission timescales. Further, a power law scaling was obtained for the number of micelles as a function of time and the exponent was plotted as a function of the salt concentration. We find that the growth rate of micelles reaches a peak value at $R=1$. This suggests that at equimolar concentrations of surfactant and salt, efficient screening of the electrostatic repulsion results in faster aggregation. We also studied CTAC/SHNC systems and estimated the zero-shear viscosity as a function of R . Our simulations suggest that the behavior of CTAC/SHNC systems are distinctly different from CTAC/NaSal systems although the two salts have very similar chemical

structures. CTAC/SHNC systems do not produce a double peak in the zero-shear viscosity with gradual increase in salt concentration. We observed a 35% increase in the zero-shear viscosity over the range of concentrations studied. A closer look at the molecular origins of the viscosity increase revealed an interesting morphology which has not been previously identified in literature. For $C_D = 0.34$ M and $0.5 < R < 1.5$, CTAC/SHNC systems tend to form semi-lamellar sheet-like structures which tend to break down into entangled micellar networks at even higher salt concentrations. Further, anomalous rheological behavior such as an increase in viscosity with increasing temperature has been observed for CTAB/SHNC system via experiments¹⁴⁵. The molecular origins of this behavior is not well understood and could be the focus of future work.

6.6. Recommendations for Future Work

6.6.1. Effect of nanoparticle charge, surface chemistry and size on the self-assembly and rheology of wormlike micelle-nanoparticle solutions

In chapter 3, we have studied the effect of nanoparticle surface charge and surface chemistry on the self-assembly and structure of nanoparticles in surfactant solutions. However, the effect of these parameters on the rheology of micelle-nanoparticle solutions has not been investigated. We have demonstrated that the CGMD framework described in this work is capable of capturing typically observed equilibrium and non-equilibrium behavior for wormlike micellar fluids and systems in which nanoparticles are dispersed in such fluids. A more thorough investigation of the nanoparticle charge, surface chemistry and size on the microstructure and rheology of such fluids is required to explain the following questions. How would nanoparticle size affect their self-assembly behavior? Would junction formation occur for extremely small

particles (~ 1 nm)? Or would these particles diffuse freely in solution like ions? Would large particles behave as macro-ions and promote the formation of multiple junctions? In other words, how would the size of the particle affect the particle functionality? Experiments have suggested that micron-sized particles do not show the same changes in rheological behavior. Does that mean that there is a limited size range over which rheological modifications are observed? Is there a reliable multi-scaled approach to study such systems? These questions definitely need to be addressed using multiscale computational modeling methods as well as novel experimental techniques. Advances in high-resolution cryo-TEM and atomic force microscopy measurements provide a promising route to explore some of these questions.

Moreover, in this work, we only studied a cationic surfactant system and its interactions with various salts, nanoparticles and solvent. Further research could also focus on the interactions between different surfactant architectures and tailored nanoparticle surfaces. From a computational perspective, studying such complex rheological behavior in non-ionic surfactant systems might be more efficient. This is because ionic systems require the inclusion of long-ranged electrostatic calculations which consumes the majority of the computing time. Simulations of non-ionic systems can provide a speedup of up to $\sim 30\%$ for systems that consist of roughly 1 million particles. A more exotic and interesting study could involve simulations of polydispersed nanoparticles as well as particles of different shapes and surface chemistries in the same solution.

6.6.2. Linear Viscoelasticity

Viscoelastic materials are those which combine the properties of elastic solids and viscous fluids. Elastic materials can be considered as having a perfect memory of their non-deformed initial

state. Therefore, any deformation in the material due to an applied stress would completely vanish as soon as the applied stress is removed. However, viscous liquids have no memory of their non-deformed initial configuration. So when the shear stress is released it remains in its last configuration. In viscoelastic materials, the stress would gradually decay in time, a phenomenon which is referred to as stress relaxation. Oscillatory shear flow experiments have become the predominant tool to study the linear viscoelasticity in soft materials¹³². In oscillatory shear flow, we apply a sinusoidal shear strain which is given by:

$$\gamma(t) = \gamma_0 \sin(\omega t) \quad (6-1)$$

The resulting shear rate is therefore given by:

$$\dot{\gamma}(t) = \gamma_0 \omega \cos(\omega t) \quad (6-2)$$

The shear stress is also sinusoidal with the same frequency, but leads the strain by a phase angle, δ .

$$\sigma(t) = \sigma_0 \sin(\omega t + \delta) \quad (6-3)$$

Here, $\gamma(t)$ is the instantaneous shear strain, γ_0 is the amplitude or the peak displacement, ω is the angular frequency of oscillation, $\dot{\gamma}(t)$ is the shear rate at time t , and $\sigma(t)$ is the shear stress at t .

Wormlike micelles as well as colloidal suspensions in wormlike micelles exhibit linear viscoelastic behavior. While current experimental techniques can provide great insight into the linear viscoelastic behavior of known fluids, they cannot provide details regarding the underlying fluid microstructure. The important questions are: Is it possible to perform CGMD simulations of oscillatory shear flow in such solutions? How reliable are these methods for studying viscoelastic behavior? If so, can these simulations be further used to study model surfactant and polymer systems? Do current MD simulations packages possess the capabilities to do such calculations? Initial progress towards this end has been made and a brief description is provided below.

Currently the GROMACS package does not have the capability to run oscillatory shear flow calculations and although the LAMMPS package does have the necessary infrastructure it is limited to nonionic systems. Therefore, in order to perform oscillatory shear flow calculations for ionic systems, we have modified the source code of the GROMACS 4.6.5 MD package and included new parameters that can create sinusoidal strains. While these codes have not been extensively tested on complex fluids, initial results seem promising. Currently, we have identified one serious limitation in using these methods to perform small-amplitude oscillatory shear (SAOS) simulations. In SAOS experiments, the maximum allowable strain is $\sim 5\%$. At such small strain values, it is difficult to get apparent changes in the stress tensor due to the presence of large fluctuations in pressure for small simulation boxes. However, the code does seem to work for large-amplitude oscillatory shear (LAOS) simulations, as evidenced by a phase shifted sinusoidal stress response of a model wormlike micelle fluid (Fig. 6.1). Further refinement of the algorithm and detailed validation of the method is required before we can study complex fluid behavior. However, the approach is novel and promising.

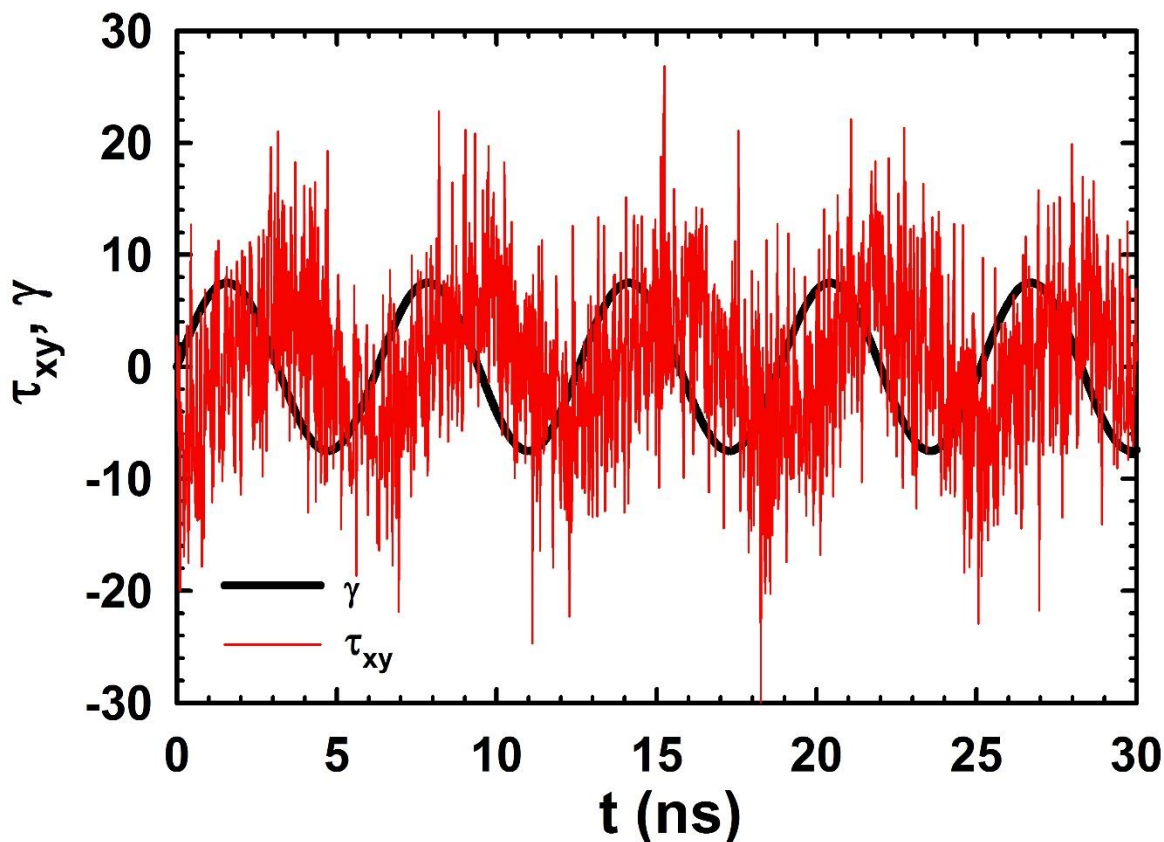


Figure 6.19: Plots of shear stress and shear strain as a function of time for a model surfactant micelle system in large-amplitude oscillatory shear flow using MD simulations. The stress response is sinusoidal and leads the applied strain by a phase angle, δ .

6.6.3. CGMD Simulations Using Implicit Solvent Models

Till date, one of the biggest challenges in the area of multiscale computational modeling and simulation of complex fluids and soft materials, at the molecular level, has been the incorporation of hydrodynamic forces. These solvent mediated interactions are crucial in determining the microstructure, self-assembly, dynamics, rheology and phase behavior of complex

fluids. However, they also consume a large majority of the computational time and resources needed to simulate such systems. So, in some ways, the presence of an explicit solvent in MD simulations is a necessary evil. Recently, a lot of work has been done in trying to create implicit solvent models for various biomolecules as well as commercial surfactants. These models can facilitate tremendous acceleration in computing time and would allow us to access much longer timescales on systems that consists of particles on the order of a few millions.

Currently, these implicit models are capable of predicting the structure of micellar fluids, lipid bilayers and proteins in water. However, it has been shown that the implicit solvent model for MARTINI CG force fields requires unphysical values for the dielectric constant of the solvent which makes it a little difficult to use it to make accurate, reliable predictions^{171, 172}. Further, the other problem with this approach is that it is not able to accurately capture the dynamics of molecules that are not part of an aggregate. For example, in micellar solutions, the dynamics of a surfactant present within a micellar aggregate is captured fairly accurately whereas a free surfactant in solution has been observed to move too fast due to the absence of hydrodynamic viscous forces on it. Future research should focus on overcoming such limitations by using more sophisticated algorithms and developing better, more accurate force fields for implicit solvent models. Advancements in this area would allow us to implement truly multiscale models on several systems of interest in the area of biology, physics, chemistry and materials science.

6.6.4. Extensional Rheology of Micelle-Nanoparticle Solutions

The extensional response of viscoelastic fluids can differ substantially from that in shear flow. In particular, the viscosity can grow more strongly at larger stretching rates than at smaller

ones due to a phenomenon referred to as strain hardening. Wormlike micelles have been shown to exhibit strain hardening behavior under several conditions. Experiments have also shown that the addition of spherical particles to polymer melts causes a reduction in strain hardening in such solutions¹⁷³. Recently, Dhakal et al.¹⁷⁴ have performed CGMD simulations of a single rodlike and wormlike micelle subjected to uniaxial extensional flow. New mechanisms such as counterion induced chain stiffening and flow-induced migration of counterions leading to micelle scission were identified which were previously not known. This clearly shows that MD simulations of micellar and micelle-nanoparticle systems can provide detailed insight into the interactions that govern the structure and dynamics of these materials.

Several important questions are raised here. How does the addition of nanoparticles change the dynamics and stability of wormlike micelles in extensional flow? Can CGMD simulations of uniaxial extensional flow of micelle-NP junctions reveal microstructural details regarding scission and redistribution of counterions in such systems? What is the mechanism of breakage of micelle-NP junctions in shear and extensional flow fields? What other physicochemical conditions can affect the stability of these junctions? Can we explore the dynamics of more biologically relevant morphologies such as vesicles and branched micelles under extensional flow? All these questions remain and could prove to be exceptionally promising research directions. One would imagine that with advancements in distributed computing platforms and efficient algorithms, these investigations will surely be made possible in the near future.

REFERENCES

1. Cates, M. E. REPTATION OF LIVING POLYMERS - DYNAMICS OF ENTANGLED POLYMERS IN THE PRESENCE OF REVERSIBLE CHAIN-SCISSION REACTIONS. *Macromolecules* **1987**, *20* (9), 2289-2296.
2. Ezrahi, S.; Tuval, E.; Aserin, A.; Garti, N. Daily Applications of Systems with Wormlike Micelles. In *Giant Micelles: Properties and Applications*, Zana, R.; Kaler, E. W., Eds., 2007; Vol. 140, pp 515-544.
3. Sullivan, P.; Nelson, E. B.; Anderson, V.; Hughes, T. Oilfield Applications of Giant Micelles. In *Giant Micelles: Properties and Applications*, Zana, R.; Kaler, E. W., Eds., 2007; Vol. 140, pp 453-472.
4. B. Chase, W. C., R. Marcinew, C. Mitchell, Y. Dang, K. Krauss, E.; Nelson, T. L., C. Parham, and J. Plummer. Clear fracturing fluids for increased well productivity. *Oilfield Review* **1997**, *9* (20).
5. Zakin, J. L.; Zhang, Y.; Ge, W. Drag Reduction by Surfactant Giant Micelles. In *Giant Micelles: Properties and Applications*, Zana, R.; Kaler, E. W., Eds., 2007; Vol. 140, pp 473-492.
6. Armstrong, K.; Card, R.; Navarrete, R.; Nelson, E.; Nimerick, K.; Samuelson, M.; Collins, J.; Dumont, G.; Priaro, M.; Wasylcia, N.; Slusher, G. ADVANCED FRACTURING FLUIDS IMPROVE WELL ECONOMICS. *Oilfield Review* **1995**, *7* (3), 34-51.
7. C. Bivins, C. B., C. Fredd, J. Lassek, P. Sullivan, J. Engels, E. O. Fielder, T. Gorham, T. Judd, A. E. Sanchez-Mogollon, L. Tabor, A. V. Munoz, and D. Willberg. *Oilfield Review* **2005**, *17* (34).

8. S. Kefi, J. L., T. L. Pope, P. Sullivan, E. Nelson, A. N. Hernandez, T. Olsen,; M. Parlar, B. P., A. Roy, A. Wilson, and A. Twynam. Expanding applications for viscoelastic surfactants. *Oilfield Review* **2005**, *16* (10).
9. Park, J.; An, K. J.; Hwang, Y. S.; Park, J. G.; Noh, H. J.; Kim, J. Y.; Park, J. H.; Hwang, N. M.; Hyeon, T. Ultra-large-scale syntheses of monodisperse nanocrystals. *Nat. Mater.* **2004**, *3* (12), 891-895.
10. Park, J.; Lee, E.; Hwang, N. M.; Kang, M. S.; Kim, S. C.; Hwang, Y.; Park, J. G.; Noh, H. J.; Kini, J. Y.; Park, J. H.; Hyeon, T. One-nanometer-scale size-controlled synthesis of monodisperse magnetic iron oxide nanoparticles. *Angewandte Chemie-International Edition* **2005**, *44* (19), 2872-2877.
11. Helgeson, M. E. Structure, rheology, and thermodynamics of wormlike micelle-nanoparticle mixtures. Ph.D., UNIVERSITY OF DELAWARE 2009.
12. Israelachvili, J. *Intermolecular and Surface Forces*; Academic Press 2011.
13. Hiemenz, P. C.; Rajagopalan, R. *Principles of Colloid and Surface Chemistry*; 3rd ed.; Taylor & Francis 1997. p 650.
14. Cates, M. E.; Candau, S. J. STATICS AND DYNAMICS OF WORM-LIKE SURFACTANT MICELLES. *J. Phys.-Condes. Matter* **1990**, *2* (33), 6869-6892.
15. Mackintosh, F. C.; Safran, S. A.; Pincus, P. A. SELF-ASSEMBLY OF LINEAR AGGREGATES - THE EFFECT OF ELECTROSTATICS ON GROWTH. *Europhys. Lett.* **1990**, *12* (8), 697-702.
16. Safran, S. A.; Pincus, P. A.; Cates, M. E.; Mackintosh, F. C. GROWTH OF CHARGED MICELLES. *Journal De Physique* **1990**, *51* (6), 503-510.

17. Dhakal, S.; Sureshkumar, R. Topology, length scales, and energetics of surfactant micelles. *J. Chem. Phys.* **2015**, *143* (2), 024905-1-024905-11.
18. Oelschlaeger, C.; Suwita, P.; Willenbacher, N. Effect of Counterion Binding Efficiency on Structure and Dynamics of Wormlike Micelles. *Langmuir* **2010**, *26* (10), 7045-7053.
19. Sangwai, A. V.; Sureshkumar, R. Coarse-Grained Molecular Dynamics Simulations of the Sphere to Rod Transition in Surfactant Micelles. *Langmuir* **2011**, *27* (11), 6628-6638.
20. Wang, Z. W.; Larson, R. G. Molecular Dynamics Simulations of Threadlike Cetyltrimethylammonium Chloride Micelles: Effects of Sodium Chloride and Sodium Salicylate Salts. *J. Phys. Chem. B* **2009**, *113* (42), 13697-13710.
21. Vasudevan, M.; Shen, A.; Khomami, B.; Sureshkumar, R. Self-similar shear thickening behavior in CTAB/NaSal surfactant solutions. *J. Rheol.* **2008**, *52* (2), 527-550.
22. Vasudevan, M.; Buse, E.; Lu, D. L.; Krishna, H.; Kalyanaraman, R.; Shen, A. Q.; Khomami, B.; Sureshkumar, R. Irreversible nanogel formation in surfactant solutions by microporous flow. *Nat. Mater.* **2010**, *9* (5), 436-441.
23. Frounfelker, B. D.; Kalur, G. C.; Cipriano, B. H.; Danino, D.; Raghavan, S. R. Persistence of Birefringence in Sheared Solutions of Wormlike Micelles. *Langmuir* **2009**, *25* (1), 167-172.
24. Cong, T. Structure, Rheology and Optical Properties of Plasmonic Fluids. Dissertation, Syracuse University 2013.
25. Faraday, M. The Bakerian lecture: experimental relations of gold (and other metals) to light. *Philosophical Transactions of the Royal Society of London* **1857**, 147.
26. Parfitt, G. D.; Rochester, C. H. *Adsorption from solution at the solid/liquid interface*; Academic Press: New York; London, 1983.

27. Cong, T.; Wani, S. N.; Paynter, P. A.; Sureshkumar, R. Structure and optical properties of self-assembled multicomponent plasmonic nanogels. *Appl. Phys. Lett.* **2011**, *99* (4), 043112-1-043112-3.
28. Helgeson, M. E.; Hodgdon, T. K.; Kaler, E. W.; Wagner, N. J.; Vethamuthu, M.; Ananthapadmanabhan, K. P. Formation and Rheology of Viscoelastic "Double Networks" in Wormlike Micelle-Nanoparticle Mixtures. *Langmuir* **2010**, *26* (11), 8049-8060.
29. Jodar-Reyes, A. B.; Leermakers, F. A. M. Can linear micelles bridge between two surfaces? *J. Phys. Chem. B* **2006**, *110* (37), 18415-18423.
30. Jodar-Reyes, A. B.; Leermakers, F. A. M. Self-consistent field modeling of linear nonionic micelles. *J. Phys. Chem. B* **2006**, *110* (12), 6300-6311.
31. Karatrantos, A.; Clarke, N.; Kroeger, M. Modeling of Polymer Structure and Conformations in Polymer Nanocomposites from Atomistic to Mesoscale: A Review. *Polymer Reviews* **2016**, *56* (3), 385-428.
32. Uneyama, T.; Doi, M. Calculation of the micellar structure of polymer surfactant on the basis of the density functional theory. *Macromolecules* **2005**, *38* (13), 5817-5825.
33. Palmer, B. J.; Liu, J. Simulations of micelle self-assembly in surfactant solutions. *Langmuir* **1996**, *12* (3), 746-753.
34. Karaborni, S.; Smit, B. Computer simulations of surfactant structures. *Curr. Opin. Colloid Interface Sci.* **1996**, *1* (3), 411-415.
35. Shelley, J. C.; Shelley, M. Y. Computer simulation of surfactant solutions. *Curr. Opin. Colloid Interface Sci.* **2000**, *5* (1-2), 101-110.
36. Mei, D. H.; O'Connell, J. P. Molecular dynamics simulations of model perhydrogenated and perfluorinated alkyl chains, droplets, and micelles. *Langmuir* **2002**, *18* (23), 9067-9079.

37. Dominguez, H.; Rivera, M. Mixtures of sodium dodecyl sulfate/dodecanol at the air/water interface by computer simulations. *Langmuir* **2005**, *21* (16), 7257-7262.
38. Trokhymchuk, A.; Henderson, D.; Nikolov, A.; Wasan, D. T. Computer modeling of ionic micelle structuring in thin films. *J. Phys. Chem. B* **2003**, *107* (16), 3927-3937.
39. Lopez, C. F.; Moore, P. B.; Shelley, J. C.; Shelley, M. Y.; Klein, M. L. Computer simulation studies of biomembranes using a coarse grain model. *Comput. Phys. Commun.* **2002**, *147* (1-2), 1-6.
40. Izvekov, S.; Voth, G. A. A multiscale coarse-graining method for biomolecular systems. *J. Phys. Chem. B* **2005**, *109* (7), 2469-2473.
41. Groot, R. D. Mesoscopic simulation of polymer-surfactant aggregation. *Langmuir* **2000**, *16* (19), 7493-7502.
42. Kim, K. Y.; Byun, K. T.; Kwak, H.-Y.; Asme. *The mesoscopic simulation on the structures of the surfactant solution using dissipative particle dynamics* 2005; Vol. 261. p 139-144.
43. Lu, D. N.; Liu, Z.; Liu, Z. X.; Zhang, M. L.; Ouyang, P. Molecular simulation of surfactant-assisted protein refolding. *J. Chem. Phys.* **2005**, *122* (13).
44. Sangwai, A. V.; Sureshkumar, R. Binary Interactions and Salt-Induced Coalescence of Spherical Micelles of Cationic Surfactants from Molecular Dynamics Simulations. *Langmuir* **2012**, *28* (2), 1127-1135.
45. Praus, P.; Dvorsky, R.; Horinkova, P.; Pospisil, M.; Kovar, P. Precipitation, stabilization and molecular modeling of ZnS nanoparticles in the presence of cetyltrimethylammonium bromide. *J. Colloid Interface Sci.* **2012**, *377*, 58-63.

46. Yue, J.; Jiang, X. C.; Zeng, Q. H.; Yu, A. B. Experimental and numerical study of cetyltrimethylammonium bromide (CTAB)-directed synthesis of goethite nanorods. *Solid State Sci.* **2010**, *12* (7), 1152-1159.
47. Liu, C. H.; Pine, D. J. Shear-induced gelation and fracture in micellar solutions. *Phys. Rev. Lett.* **1996**, *77* (10), 2121-2124.
48. Miller, E.; Rothstein, J. P. Transient evolution of shear-banding wormlike micellar solutions. *J. Non-Newton. Fluid Mech.* **2007**, *143* (1), 22-37.
49. Rehage, H.; Wunderlich, I.; Hoffmann, H. Shear induced phase transitions in dilute aqueous surfactant solutions. In *Polymers as Colloid Systems*, Springer, J., Ed.; Steinkopff, 1986; Vol. 72, pp 51-59.
50. Turner, M. S.; Cates, M. E. Flow-induced phase-transitions in rod-like micelles. *J. Phys.-Condes. Matter* **1992**, *4* (14), 3719-3741.
51. Wunderlich, I.; Hoffmann, H.; Rehage, H. Flow birefringence and rheological measurements on shear induced micellar structures. *Rheol. Acta* **1987**, *26* (6), 532-542.
52. Doi, M.; Edwards, S. F. *The theory of polymer dynamics*; Clarendon Press 1987.
53. Doyle, P. S.; Bibette, J.; Bancaud, A.; Viovy, J. L. Self-assembled magnetic matrices for DNA separation chips. *Science* **2002**, *295* (5563), 2237-2237.
54. Teclerian, N. P.; Beck, V. A.; Shaqfeh, E. S. G.; Muller, S. J. Dynamics of DNA polymers in post arrays: Comparison of single molecule experiments and simulations. *Macromolecules* **2007**, *40* (10), 3848-3859.
55. Kim, J. M.; Doyle, P. S. Design and numerical simulation of a DNA electrophoretic stretching device. *Lab on a Chip* **2007**, *7* (2), 213-225.

56. Huang, C. C.; Sutmman, G.; Gompper, G.; Winkler, R. G. Tumbling of polymers in semidilute solution under shear flow. *Epl* **2011**, *93* (5).
57. Kobayashi, H.; Yamamoto, R. Tumbling motion of a single chain in shear flow: A crossover from Brownian to non-Brownian behavior. *Phys. Rev. E* **2010**, *81* (4).
58. Schroeder, C. M.; Teixeira, R. E.; Shaqfeh, E. S. G.; Chu, S. Characteristic Periodic Motion of Polymers in Shear Flow. *Phys. Rev. Lett.* **2005**, *95* (1), 018301.
59. Smith, D. E.; Babcock, H. P.; Chu, S. Single-polymer dynamics in steady shear flow. *Science* **1999**, *283* (5408), 1724-1727.
60. Smith, D. E.; Chu, S. Response of flexible polymers to a sudden elongational flow. *Science* **1998**, *281* (5381), 1335-1340.
61. Teixeira, R. E.; Babcock, H. P.; Shaqfeh, E. S. G.; Chu, S. Shear thinning and tumbling dynamics of single polymers in the flow-gradient plane. *Macromolecules* **2005**, *38* (2), 581-592.
62. Winkler, R. G. Semiflexible polymers in shear flow. *Phys. Rev. Lett.* **2006**, *97* (12).
63. Lee, J. S.; Kim, J. M. Tumbling Dynamics of Rod-like and Semi-flexible Polymers in Simple Shear and Mixed Flows. *Macromol. Res.* **2009**, *17* (10), 807-812.
64. Yang, Y. Structure, Dynamics and Rheology of Polymer Solutions from Coarse-Grained Molecular Dynamics: Effects of Polymer Concentration, Solvent Quality and Geometric Confinement. Ph. D., Syracuse University 2015.
65. Vasquez, P. A.; McKinley, G. H.; Cook, L. P. A network scission model for wormlike micellar solutions - I. Model formulation and viscometric flow predictions. *J. Non-Newton. Fluid Mech.* **2007**, *144* (2-3), 122-139.
66. Fielding, S. M. Viscoelastic Taylor-Couette Instability of Shear Banded Flow. *Phys. Rev. Lett.* **2010**, *104* (19).

67. Fielding, S. M.; Olmsted, P. D. Spatiotemporal oscillations and rheochaos in a simple model of shear banding. *Phys. Rev. Lett.* **2004**, *92* (8).
68. Macias, E. R.; Bautista, F.; Soltero, J. F. A.; Puig, J. E.; Attane, R.; Manera, O. On the shear thickening flow of dilute CTAT worm-like micellar solutions. *J. Rheol.* **2003**, *47* (3), 643-658.
69. Nicolas, A.; Morozov, A. Nonaxisymmetric Instability of Shear-Banded Taylor-Couette Flow. *Phys. Rev. Lett.* **2012**, *108* (8).
70. Padding, J. T.; Boek, E. S.; Briels, W. J. Rheology of wormlike micellar fluids from Brownian and molecular dynamics simulations. *J. Phys.-Condes. Matter* **2005**, *17* (45), S3347-S3353.
71. Sambasivam, A.; Sangwai, A. V.; Sureshkumar, R. Dynamics and Scission of Rodlike Cationic Surfactant Micelles in Shear Flow. *Phys. Rev. Lett.* **2015**, *114* (15), 158302.
72. Marrink, S. J.; Risselada, H. J.; Yefimov, S.; Tieleman, D. P.; de Vries, A. H. The MARTINI Force Field: Coarse Grained Model for Biomolecular Simulations. *J. Phys. Chem. B* **2007**, *111* (27), 7812-7824.
73. Yesylevskyy, S. O.; Schafer, L. V.; Sengupta, D.; Marrink, S. J. Polarizable Water Model for the Coarse-Grained MARTINI Force Field. *PLoS Comput. Biol.* **2010**, *6* (6).
74. Lees, A. W. E., S. F. The computer study of transport processes under extreme conditions. *Journal of Physics C: Solid State Physics* **1972**, *5* (15), 1921-1929.
75. Celani, A.; Puliafito, A.; Turitsyn, K. Polymers in linear shear flow: A numerical study. *Europhys. Lett.* **2005**, *70* (4), 464-470.
76. Chertkov, M.; Kolokolov, I.; Lebedev, V.; Turitsyn, K. Polymer statistics in a random flow with mean shear. *Journal of Fluid Mechanics* **2005**, *531*, 251-260.

77. Puliafito, A.; Turitsyn, K. Numerical study of polymer tumbling in linear shear flows. *Physica D-Nonlinear Phenomena* **2005**, *211* (1-2), 9-22.
78. Sultan, E.; de Meent, J. W. v.; Somfai, E.; Morozov, A. N.; van Saarloos, W. Polymer rheology simulations at the meso- and macroscopic scale. *Epl* **2010**, *90* (6).
79. Jorgensen, W. L.; Maxwell, D. S.; Tirado-Rives, J. Development and Testing of the OPLS All-Atom Force Field on Conformational Energetics and Properties of Organic Liquids. *Journal of the American Chemical Society* **1996**, *118* (45), 11225-11236.
80. Freindorf, M.; Kraka, E.; Cremer, D. A comprehensive analysis of hydrogen bond interactions based on local vibrational modes. *International Journal of Quantum Chemistry* **2012**, *112* (19), 3174-3187.
81. Huber, G.; Mantz, H.; Spolenak, R.; Mecke, K.; Jacobs, K.; Gorb, S. N.; Arzt, E. Evidence for capillarity contributions to gecko adhesion from single spatula nanomechanical measurements. *Proceedings of the National Academy of Sciences of the United States of America* **2005**, *102* (45), 16293-16296.
82. Hsieh, C. C.; Jain, S.; Larson, R. G. Brownian dynamics simulations with stiff finitely extensible nonlinear elastic-Fraenkel springs as approximations to rods in bead-rod models (vol 124, pg 044911, 2006). *J. Chem. Phys.* **2006**, *124* (17).
83. Suleimanov, B. A.; Ismailov, F. S.; Veliyev, E. F. Nanofluid for enhanced oil recovery. *Journal of Petroleum Science and Engineering* **2011**, *78* (2), 431-437.
84. Davis, M. E.; Chen, Z.; Shin, D. M. Nanoparticle therapeutics: an emerging treatment modality for cancer. *Nat. Rev. Drug Discov.* **2008**, *7* (9), 771-782.
85. Anker, J. N.; Hall, W. P.; Lyandres, O.; Shah, N. C.; Zhao, J.; Van Duyne, R. P. Biosensing with plasmonic nanosensors. *Nat. Mater.* **2008**, *7* (6), 442-453.

86. Gao, X. H.; Cui, Y. Y.; Levenson, R. M.; Chung, L. W. K.; Nie, S. M. In vivo cancer targeting and imaging with semiconductor quantum dots. *Nat. Biotechnol.* **2004**, *22* (8), 969-976.
87. Narayanan, R.; El-Sayed, M. A. Catalysis with transition metal nanoparticles in colloidal solution: Nanoparticle shape dependence and stability. *J. Phys. Chem. B* **2005**, *109* (26), 12663-12676.
88. Israelowitz, M.; Amey, J.; Cong, T.; Sureshkumar, R. Spin Coated Plasmonic Nanoparticle Interfaces for Photocurrent Enhancement in Thin Film Si Solar Cells. *Journal of Nanomaterials* **2014**, *2014*, 1-9.
89. Corbierre, M. K.; Cameron, N. S.; Sutton, M.; Mochrie, S. G. J.; Lurio, L. B.; Ruhm, A.; Lennox, R. B. Polymer-stabilized gold nanoparticles and their incorporation into polymer matrices. *Journal of the American Chemical Society* **2001**, *123* (42), 10411-10412.
90. Estridge, C. E.; Jayaraman, A. Assembly of diblock copolymer functionalized spherical nanoparticles as a function of copolymer composition. *J. Chem. Phys.* **2014**, *140* (14), 144905-1-144905-13.
91. Estridge, C. E.; Jayaraman, A. Diblock Copolymer Grafted Particles as Compatibilizers for Immiscible Binary Homopolymer Blends. *ACS Macro Lett.* **2015**, *4* (2), 155-159.
92. Nykypanchuk, D.; Maye, M. M.; van der Lelie, D.; Gang, O. DNA-guided crystallization of colloidal nanoparticles. *Nature* **2008**, *451* (7178), 549-552.
93. Dhakal, S.; Kohlstedt, K. L.; Schatz, G. C.; Mirkin, C. A.; de la Cruz, M. O. Growth Dynamics for DNA-Guided Nanoparticle Crystallization. *Acs Nano* **2013**, *7* (12), 10948-10959.
94. Gorelikov, I.; Matsuura, N. Single-step coating of mesoporous silica on cetyltrimethyl ammonium bromide-capped nanoparticles. *Nano Letters* **2008**, *8* (1), 369-373.

95. Li, T. H.; Park, H. G.; Lee, H. S.; Choi, S. H. Circular dichroism study of chiral biomolecules conjugated nanoparticles. *Nanotechnology* **2004**, *15* (10), S660-S663.
96. Varade, D.; Haraguchi, K. One-pot synthesis of noble metal nanoparticles and their ordered self-assembly nanostructures. *Soft Matter* **2012**, *8* (14), 3743-3746.
97. Sperling, R. A.; Parak, W. J. Surface modification, functionalization and bioconjugation of colloidal inorganic nanoparticles. *Therapeutic Innovation & Regulatory Science* **2013**, *47* (1), 1333-1383.
98. Goodman, C. M.; McCusker, C. D.; Yilmaz, T.; Rotello, V. M. Toxicity of gold nanoparticles functionalized with cationic and anionic side chains. *Bioconjugate Chemistry* **2004**, *15* (4), 897-900.
99. Connor, E. E.; Mwamuka, J.; Gole, A.; Murphy, C. J.; Wyatt, M. D. Gold nanoparticles are taken up by human cells but do not cause acute cytotoxicity. *Small* **2005**, *1* (3), 325-327.
100. Patrick, H. N.; Warr, G. G. Self-assembly structures of nonionic surfactants at graphite-solution inter-faces. 2. Effect of polydispersity and alkyl chain branching. *Colloid Surf. A-Physicochem. Eng. Asp.* **2000**, *162* (1-3), 149-157.
101. Wanless, E. J.; Ducker, W. A. Weak influence of divalent ions on anionic surfactant surface-aggregation. *Langmuir* **1997**, *13* (6), 1463-1474.
102. Furst, E. M.; Pagac, E. S.; Tilton, R. D. Coadsorption of polylysine and the cationic surfactant cetyltrimethylammonium bromide on silica. *Industrial & Engineering Chemistry Research* **1996**, *35* (5), 1566-1574.
103. Nikoobakht, B.; El-Sayed, M. A. Evidence for bilayer assembly of cationic surfactants on the surface of gold nanorods. *Langmuir* **2001**, *17* (20), 6368-6374.

104. Nettesheim, F.; Liberatore, M. W.; Hodgdon, T. K.; Wagner, N. J.; Kaler, E. W.; Vethamuthu, M. Influence of nanoparticle addition on the properties of wormlike micellar solutions. *Langmuir* **2008**, *24* (15), 7718-7726.
105. Sui, Z. M.; Chen, X.; Wang, L. Y.; Xu, L. M.; Zhuang, W. C.; Chai, Y. C.; Yang, C. J. Capping effect of CTAB on positively charged Ag nanoparticles. *Physica E* **2006**, *33* (2), 308-314.
106. Yang, C. J.; Chen, X.; Sui, Z. M.; Wang, L. Y. Molecular dynamics simulation of a positively charged silver nanoparticle capped by cetyltrimethylammonium cations. *Colloid Surf. A-Physicochem. Eng. Asp.* **2006**, *274* (1-3), 219-222.
107. Berendsen, H. J. C.; Vanderspoel, D.; Vandrunen, R. GROMACS - A MESSAGE-PASSING PARALLEL MOLECULAR-DYNAMICS IMPLEMENTATION. *Comput. Phys. Commun.* **1995**, *91* (1-3), 43-56.
108. Lin, J. Q.; Zhang, H. W.; Chen, Z.; Zheng, Y. G. Penetration of Lipid Membranes by Gold Nanoparticles: Insights into Cellular Uptake, Cytotoxicity, and Their Relationship. *Acs Nano* **2010**, *4* (9), 5421-5429.
109. Nangia, S.; Sureshkumar, R. Effects of Nanoparticle Charge and Shape Anisotropy on Translocation through Cell Membranes. *Langmuir* **2012**, *28* (51), 17666-17671.
110. Kim, T.; Lee, C. H.; Joo, S. W.; Lee, K. Kinetics of gold nanoparticle aggregation: Experiments and modeling. *J. Colloid Interface Sci.* **2008**, *318* (2), 238-243.
111. Kim, T.; Lee, K.; Gong, M. S.; Joo, S. W. Control of gold nanoparticle aggregates by manipulation of interparticle interaction. *Langmuir* **2005**, *21* (21), 9524-9528.
112. Favoriti, P.; Mannebach, M. H.; Treiner, C. Surface interactions on silica particles between a cationic surfactant and sodium salicylate. *Langmuir* **1996**, *12* (20), 4691-4696.

113. Magan, R. V.; Sureshkumar, R. Multiscale-linking simulation of irreversible colloidal deposition in the presence of DLVO interactions. *J. Colloid Interface Sci.* **2006**, *297* (2), 389-406.
114. Paria, S.; Khilar, K. C. A review on experimental studies of surfactant adsorption at the hydrophilic solid-water interface. *Advances in Colloid and Interface Science* **2004**, *110* (3), 75-95.
115. Helgeson, M. E.; Wagner, N. J. Colloidal interactions mediated by end-adsorbing polymer-like micelles. *J. Chem. Phys.* **2011**, *135* (8), 084901-1-084901-11.
116. Cates, M. E. DYNAMICS OF LIVING POLYMERS AND FLEXIBLE SURFACTANT MICELLES - SCALING LAWS FOR DILUTION. *Journal De Physique* **1988**, *49* (9), 1593-1600.
117. Cates, M. E. THEORY OF THE VISCOSITY OF POLYMERIC LIQUID SULFUR. *Europhys. Lett.* **1987**, *4* (4), 497-502.
118. Bandyopadhyay, R.; Sood, A. K. Effect of silica colloids on the rheology of viscoelastic gels formed by the surfactant cetyl trimethylammonium tosylate. *J. Colloid Interface Sci.* **2005**, *283* (2), 585-591.
119. Mendoza, L. D.; Rabelero, M.; Escalante, J. I.; Macias, E. R.; Gonzalez-Alvarez, A.; Bautista, F.; Soltero, J. F. A.; Puig, J. E. Rheological behavior of surfactant-based precursors of silica mesoporous materials. *J. Colloid Interface Sci.* **2008**, *320* (1), 290-297.
120. Sambasivam, A.; Sangwai, A. V.; Sureshkumar, R. Self-Assembly of Nanoparticle-Surfactant Complexes with Rodlike Micelles: A Molecular Dynamics Study. *Langmuir* **2016**, *32* (5), 1214-1219.
121. Plimpton, S. Fast parallel algorithms for short-range molecular dynamics. *J. Comput. Phys.* **1995**, *117* (1), 1-19.

122. Piella, J.; Bastus, N. G.; Puntès, V. Size-Controlled Synthesis of Sub-10-nanometer Citrate-Stabilized Gold Nanoparticles and Related Optical Properties. *Chem. Mat.* **2016**, *28* (4), 1066-1075.
123. Buneman, O. COMPUTER-SIMULATION USING PARTICLES - HOCKNEY,RW, EASTWOOD,JW. *Siam Review* **1983**, *25* (3), 425-426.
124. Pollock, E. L.; Glosli, J. Comments on P(3)M, FMM, and the Ewald method for large periodic coulombic systems. *Comput. Phys. Commun.* **1996**, *95* (2-3), 93-110.
125. Palmer, B. J. TRANSVERSE-CURRENT AUTOCORRELATION-FUNCTION CALCULATIONS OF THE SHEAR VISCOSITY FOR MOLECULAR LIQUIDS. *Phys. Rev. E* **1994**, *49* (1), 359-366.
126. Allen, M. P.; Tildesley, D. J. *Computer simulation of liquids*; Clarendon Press: New York;Oxford [England];, 1987.
127. Zwanzig, R. TIME-CORRELATION FUNCTIONS AND TRANSPORT COEFFICIENTS IN STATISTICAL MECHANICS. *Annual Review of Physical Chemistry* **1965**, *16*, 67-&.
128. Evans, D. J.; Morriss, G. P. *Statistical Mechanics of Nonequilibrium Liquids* 2007. p 1-302.
129. Muller-Plathe, F. Reversing the perturbation in nonequilibrium molecular dynamics: An easy way to calculate the shear viscosity of fluids. *Phys. Rev. E* **1999**, *59* (5), 4894-4898.
130. Kelkar, M. S.; Rafferty, J. L.; Maginn, E. J.; Siepmann, J. I. Prediction of viscosities and vapor-liquid equilibria for five polyhydric alcohols by molecular simulation. *Fluid Phase Equilibria* **2007**, *260* (2), 218-231.

131. Lequeux, F. Reptation of Connected Wormlike Micelles. *Europhys. Lett.* **1992**, *19* (8), 675-681.
132. Larson, R. G.; Books24x, I. *The structure and rheology of complex fluids*; Oxford University Press: New York, 1999.
133. Rehage, H.; Hoffmann, H. VISCOELASTIC SURFACTANT SOLUTIONS - MODEL SYSTEMS FOR RHEOLOGICAL RESEARCH. *Molecular Physics* **1991**, *74* (5), 933-973.
134. Fischer, E.; Callaghan, P. T. Shear banding and the isotropic-to-nematic transition in wormlike micelles. *Phys. Rev. E* **2001**, *64* (1), 15.
135. Boukany, P. E.; Hu, Y. T.; Wang, S.-Q. Observations of wall slip and shear banding in an entangled DNA solution. *Macromolecules* **2008**, *41* (7), 2644-2650.
136. Boukany, P. E.; Wang, S.-Q.; Ravindranath, S.; Lee, L. J. Shear banding in entangled polymers in the micron scale gap: a confocal-rheoscopic study. *Soft Matter* **2015**, *11* (41), 8058-8068.
137. Sprakel, J.; Spruijt, E.; Stuart, M. A. C.; Besseling, N. A. M.; Lettinga, M. P.; van der Gucht, J. Shear banding and rheochaos in associative polymer networks. *Soft Matter* **2008**, *4* (8), 1696-1705.
138. van der Gucht, J.; Lemmers, M.; Knoben, W.; Besseling, N. A. M.; Lettinga, M. P. Multiple shear-banding transitions in a supramolecular polymer solution. *Phys. Rev. Lett.* **2006**, *97* (10).
139. Vermant, J.; Solomon, M. J. Flow-induced structure in colloidal suspensions. *J. Phys.-Condes. Matter* **2005**, *17* (4), R187-R216.
140. Rogers, S. A.; Vlassopoulos, D.; Callaghan, P. T. Aging, yielding, and shear banding in soft colloidal glasses. *Phys. Rev. Lett.* **2008**, *100* (12).

141. Barnes, H. A. A review of the rheology of filled viscoelastic systems. *Rheology Reviews* **2003**, 36.
142. Metzner, A. B. RHEOLOGY OF SUSPENSIONS IN POLYMERIC LIQUIDS. *J. Rheol.* **1985**, 29 (6), 739-775.
143. Lopez-Gonzalez, M. R.; Holmes, W. M.; Callaghan, P. T. Rheo-NMR phenomena of wormlike micelles. *Soft Matter* **2006**, 2 (10), 855-869.
144. Ohl, N.; Gleissle, W. THE CHARACTERIZATION OF THE STEADY-STATE SHEAR AND NORMAL STRESS FUNCTIONS OF HIGHLY CONCENTRATED SUSPENSIONS FORMULATED WITH VISCOELASTIC LIQUIDS. *J. Rheol.* **1993**, 37 (2), 381-406.
145. Kalur, G. C.; Frounfelker, B. D.; Cipriano, B. H.; Norman, A. I.; Raghavan, S. R. Viscosity increase with temperature in cationic surfactant solutions due to the growth of wormlike micelles. *Langmuir* **2005**, 21 (24), 10998-11004.
146. Mishra, B. K.; Samant, S. D.; Pradhan, P.; Mishra, S. B.; Manohar, C. A NEW STRONGLY FLOW BIREFRINGENT SURFACTANT SYSTEM. *Langmuir* **1993**, 9 (4), 894-898.
147. Mishra, S.; Mishra, B. K.; Samant, S. D.; Narayanan, J.; Manohar, C. CHARGE-INDUCED NEMATIC ISOTROPIC TRANSITION IN MIXED SURFACTANT SOLUTIONS. *Langmuir* **1993**, 9 (11), 2804-2807.
148. Kaler, E. W.; Murthy, A. K.; Rodriguez, B. E.; Zasadzinski, J. A. N. SPONTANEOUS VESICLE FORMATION IN AQUEOUS MIXTURES OF SINGLE-TAILED SURFACTANTS. *Science* **1989**, 245 (4924), 1371-1374.

149. Hartmann, V.; Cressely, R. Simple salts effects on the characteristics of the shear thickening exhibited by an aqueous micellar solution of CTAB/NaSal. *Europhys. Lett.* **1997**, *40* (6), 691-696.
150. Gravsholt, S. VISCOELASTICITY IN HIGHLY DILUTE AQUEOUS-SOLUTIONS OF PURE CATIONIC DETERGENTS. *J. Colloid Interface Sci.* **1976**, *57* (3), 575-577.
151. Maillet, J. B.; Lachet, V.; Coveney, P. V. Large scale molecular dynamics simulation of self-assembly processes in short and long chain cationic surfactants. *Physical Chemistry Chemical Physics* **1999**, *1* (23), 5277-5290.
152. Marrink, S. J.; Tieleman, D. P.; Mark, A. E. Molecular dynamics simulation of the kinetics of spontaneous micelle formation. *J. Phys. Chem. B* **2000**, *104* (51), 12165-12173.
153. Piotrovskaya, E. M.; Vanin, A. A.; Smirnova, N. A. Molecular dynamics simulation of micellar aggregates in aqueous solution of hexadecyl trimethylammonium chloride with different additives. *Molecular Physics* **2006**, *104* (22-24), 3645-3651.
154. Lorenz, C. D.; Hsieh, C.-M.; Dreiss, C. A.; Lawrence, M. J. Molecular Dynamics Simulations of the Interfacial and Structural Properties of Dimethyldodecylamine-N-Oxide Micelles. *Langmuir* **2011**, *27* (2), 546-553.
155. Cheong, D. W.; Panagiotopoulos, A. Z. Monte Carlo simulations of micellization in model ionic surfactants: Application to sodium dodecyl sulfate. *Langmuir* **2006**, *22* (9), 4076-4083.
156. Davis, J. R.; Panagiotopoulos, A. Z. Micellization and phase separation in binary amphiphile mixtures. *Molecular Physics* **2009**, *107* (22), 2359-2366.
157. Mackie, A. D.; Onur, K.; Panagiotopoulos, A. Z. Phase equilibria of a lattice model for an oil-water-amphiphile mixture. *J. Chem. Phys.* **1996**, *104* (10), 3718-3725.

158. Smit, B.; Hilbers, P. A. J.; Esselink, K.; Rupert, L. A. M.; Vanos, N. M.; Schlijper, A. G. COMPUTER-SIMULATIONS OF A WATER OIL INTERFACE IN THE PRESENCE OF MICELLES. *Nature* **1990**, *348* (6302), 624-625.
159. Padding, J. T.; Boek, E. S.; Briels, W. J. Dynamics and rheology of wormlike micelles emerging from particulate computer simulations. *J. Chem. Phys.* **2008**, *129* (7).
160. Padding, J. T.; Briels, W. J.; Stukan, M. R.; Boek, E. S. Review of multi-scale particulate simulation of the rheology of wormlike micellar fluids. *Soft Matter* **2009**, *5* (22), 4367-4375.
161. Morisada, S.; Shinto, H.; Higashitani, K. Revised implicit solvent model for the simulation of surfactants in aqueous solutions. *J. Phys. Chem. B* **2005**, *109* (23), 11762-11769.
162. Shinto, H.; Morisada, S.; Miyahara, M.; Higashitani, K. Langevin dynamics simulations of cationic surfactants in aqueous solutions using potentials of mean force. *Langmuir* **2004**, *20* (5), 2017-2025.
163. Zhang, Y.; Otani, A.; Maginn, E. J. Reliable Viscosity Calculation from Equilibrium Molecular Dynamics Simulations: A Time Decomposition Method. *Journal of Chemical Theory and Computation* **2015**, *11* (8), 3537-3546.
164. Patist, A.; Kanicky, J. R.; Shukla, P. K.; Shah, D. O. Importance of micellar kinetics in relation to technological processes. *J. Colloid Interface Sci.* **2002**, *245* (1), 1-15.
165. Yuan, F.; Wang, S.; Larson, R. G. Potentials of Mean Force and Escape Times of Surfactants from Micelles and Hydrophobic Surfaces Using Molecular Dynamics Simulations. *Langmuir* **2015**, *31* (4), 1336-1343.
166. Frindi, M.; Michels, B.; Zana, R. ULTRASONIC-ABSORPTION STUDIES OF SURFACTANT EXCHANGE BETWEEN MICELLES AND BULK PHASE IN AQUEOUS

- MICELLAR SOLUTIONS OF NONIONIC SURFACTANTS WITH A SHORT ALKYL CHAIN
- .3. SURFACTANTS WITH A SUGAR HEAD GROUP. *J. Phys. Chem.* **1992**, *96* (20), 8137-8141.
167. Kato, S.; Harada, S.; Sahara, H. ULTRASONIC RELAXATION AND VOLUMETRIC STUDIES OF THE MICELLE MONOMER EXCHANGE PROCESS IN AQUEOUS-SOLUTIONS OF THE NONIONIC SURFACTANTS C(7)E(4), C(8)E(4), AND C(8)E(5). *J. Phys. Chem.* **1995**, *99* (33), 12570-12575.
168. Talmon, Y. Seeing Giant Micelles by Cryogenic-Temperature Transmission Electron Microscopy (Cryo-TEM). In *Giant Micelles: Properties and Applications*, Zana, R.; Kaler, E. W., Eds., 2007; Vol. 140, pp 163-178.
169. Cates, M.; Fielding, S. Theoretical Rheology of Giant Micelles. In *Giant Micelles: Properties and Applications*, Zana, R.; Kaler, E. W., Eds., 2007; Vol. 140, pp 109-161.
170. Brassard, M. *Cosmetics & Toiletries* **1989**, *104* (53).
171. Arnarez, C.; Uusitalo, J. J.; Masman, M. F.; Ingolfsson, H. I.; de Jong, D. H.; Melo, M. N.; Periole, X.; de Vries, A. H.; Marrink, S. J. Dry Martini, a Coarse-Grained Force Field for Lipid Membrane Simulations with Implicit Solvent. *Journal of Chemical Theory and Computation* **2015**, *11* (1), 260-275.
172. Wang, S.; Larson, R. G. Coarse-Grained Molecular Dynamics Simulation of Self-Assembly and Surface Adsorption of Ionic Surfactants Using an Implicit Water Model. *Langmuir* **2015**, *31* (4), 1262-1271.
173. Mewis, J.; Wagner, N. J. *Colloidal suspension rheology*; Cambridge University Press: Cambridge; New York, 2012.

174. Dhakal, S.; Sureshkumar, R. Uniaxial Extension of Surfactant Micelles: Counterion Mediated Chain Stiffening and a Mechanism of Rupture by Flow-Induced Energy Redistribution. *ACS Macro Lett.* **2016**, *5* (1), 108-111.

ABHINANDEN SAMBASIVAM

120 Remington Avenue, Apt. L, Syracuse, NY 13210
Ph.: (703) 568-3869, Email: abhinanden@gmail.com

Objective

Highly motivated chemical engineer with 5+ years of experience in multiscale computational modeling, numerical methods, materials science, rheology and scientific programming. Analytical problem-solver with exceptional communication and organizational skills seeking a challenging R&D position.

Education

Ph.D. in Chemical Engineering (2016)

College of Engineering and Computer Science, Syracuse University, Syracuse, NY

- GPA: 3.88/4.0
- Research Specialization: Computational chemistry, polymer physics, structure-property relationships, material characterization, rheology and data analysis
- Proficiency with multiscale computational modeling techniques such as molecular dynamics (MD), Monte Carlo simulations, mesoscale and Finite Element Modeling (FEM)

B. Tech. in Chemical Engineering (2010)

St. Joseph's College of Engineering, Anna University, Chennai, India

- Graduated top 2%; Ranked 10th among ~500 students in the University

Technical Skills

Programming: FORTRAN, C/C++, Linux shell scripting, Python, Parallel computing (MPI, OpenMP)

Classical MD: GROMACS, LAMMPS, NAMD packages. **Force-fields:** MARTINI, Gromos, OPLS

Numerical methods: R, MATLAB, COMSOL, Computational Fluid Dynamics (CFD)

Quantum simulations: *Ab-initio* & Monte Carlo methods, Importance sampling

Integration: Finite Element Analysis (FEA), Finite difference methods

Data Analysis: Eureka, Design of Experiments (DOE) and Statistical Process Control (SPC) methods

Other software: VMD, Yasara, PyMol, LaTeX, Polymath, Mathematica, Sigma Plot

Instrumentation: TEM, SEM, AFM, Rheometer (AR-G2), Spectrophotometer, Spin coating, Dip coating

Research Experience

Research Assistant, Sureshkumar Research Group, Syracuse University (2010-2016)

- Provided the first visual observation of the dynamics of “living” polymers under shear flow using large-scale molecular dynamics simulations
- Comprehensively researched the microstructure, self-assembly and rheology of surfactant-based plasmonic nanogels using a combination of experimental and simulation techniques
- Developed a novel algorithm to probe the linear viscoelasticity of complex fluids near equilibrium conditions using molecular simulations that mimic experimental measurements
- Hypothesized and proved mechanisms of nanoparticle-polymer self-assembly
- Developed new software and object-oriented codes to perform electronic structure calculations using the Metropolis Monte Carlo method and estimated the ground-state energies for small molecules.

Publications

- **Sambasivam, A.**, Sangwai, A.V., Sureshkumar, R., ‘Dynamics and Scission of Rodlike Cationic Surfactant Micelles in Shear Flow’, *Physical Review Letters*, **114** (15), 158302, 2015.
- **Sambasivam, A.**, Sangwai, A.V., Sureshkumar, R., ‘Self-assembly in a nanoparticle-cationic surfactant micelle solution: a molecular dynamics study’, *Langmuir*, **32** (5), 1214-1219, 2016. (Featured on the cover of *Langmuir*!)
- **Sambasivam, A.**, Elward, J., Chakraborty, A., ‘A multi-determinant electron-nuclear quantum Monte Carlo method for ground state solution of molecular Hamiltonian’ (manuscript in preparation)
- **Sambasivam, A.**, Dhakal, S., Sureshkumar, R., ‘Structure-rheology relationship in nanoparticle-wormlike micelle mixtures using molecular dynamics simulations’ (manuscript in preparation).

Selected Conference Presentations

- Computational Rheology of Surfactant Micelles and Micelle-nanoparticle Solutions: A Molecular Dynamics Study. **Nunan Research Day**, Syracuse, NY, April 6, 2015.
- Microstructure-rheology relationship in surfactant micelle and micelle-nanoparticle solutions: a molecular dynamics study. **AIChE Annual Meeting**, Atlanta, GA, November 18, 2014.
- Structure and rheology of micelle and micelle-nanoparticle solutions from molecular dynamics simulations, **247th ACS National Meeting and Exposition**, Dallas, TX, March 20, 2014.
- Multi-determinant electron-nuclear quantum Monte Carlo method for ground state solution of molecular Hamiltonian, **APS March Meeting**, Baltimore, MD, March 19, 2013.

Honors & Awards

- **Grand Prize-Best Graduate Research Poster**, Nunan Research Day (April 2016)
- **Best Student Poster Award**, BMCE Department, Nunan Research Day (April 2015)
- **Syracuse University Graduate Fellowship** (Most prestigious graduate student award) (2010-2014)
- **Best Student Poster Award**, 83rd Annual Meeting of The Society of Rheology (October 2011)
- **Summer Fellowship Award** (2011, 2014)
- **Outstanding Undergraduate Student Award**, Department of Chemical Engineering, St. Joseph’s College of Engineering, Anna University (2010)
- **Academic Excellence Scholarship** (Merit based) (2007, 2008, 2010)

Teaching and Mentoring Experience

Undergraduate Research Mentor, Syracuse University (Summer 2013)

- Trained students under the Research Experiences for Undergraduates (REU) program funded by NSF.
- Provided hands-on training with multiscale computational modeling and simulations of polymeric solutions on high-performance computing systems including GPU architectures.

Teaching Assistant/Co-Instructor, Syracuse University

- Multiscale Computational Methods (CEN 600) (Spring 2013,2014)
- Mathematical Methods in Chemical Engineering (CEN 671) (Fall 2013,2015)

Relevant Courses

Multiscale Computational Methods
Object Oriented Programming in C++

Complex Fluids & Flows
Mathematical Methods

Fluid Dynamics
Polymer Physics